BEILSTEIN JOURNAL OF NANOTECHNOLOGY

High-resolution electrical and chemical characterization of nm-scale organic and inorganic devices

Edited by Ernst Meyer and Pierre Eyben

Imprint

Beilstein Journal of Nanotechnology
www.bjnano.org
ISSN 2190-4286
Email: journals-support@beilstein-institut.de

The *Beilstein Journal of Nanotechnology* is published by the Beilstein-Institut zur Förderung der Chemischen Wissenschaften.

Beilstein-Institut zur Förderung der Chemischen Wissenschaften
Trakehner Straße 7–9
60487 Frankfurt am Main
Germany
www.beilstein-institut.de

Beilstein Journal of Nanotechnology

High-resolution electrical and chemical characterization of nm-scale organic and inorganic devices

Pierre Eyben

Editorial

Open Access

Address:
IMEC VZW, Kapeldreef 75, 3001 Leuven, Belgium

Email:
Pierre Eyben - pierre.eyben@imec.be

Beilstein J. Nanotechnol. **2013,** *4,* 318–319.
doi:10.3762/bjnano.4.35

Received: 03 April 2013
Accepted: 06 April 2013
Published: 16 May 2013

This article is part of the Thematic Series "High-resolution electrical and chemical characterization of nm-scale organic and inorganic devices"

Editor-in-Chief: T. Schimmel

Almost ever since the advent of the microelectronics adventure, silicon-based MOSFET (metal–oxide–semiconductor field-effect transistor) technology has been largely dominant. However, for a few years now this technology has exhibited some fundamental limitations in tackling the increasingly challenging issues of miniaturization and improvements in processing speed and power consumption. Hence, new inorganic semiconductor materials (Ge, InGaAs, InP, InSb, GaN, GaSb, SiC, etc.) and new architectures (multiple-gate FETs, nanowire T-FETs, etc.) are being progressively introduced.

These new materials are mainly introduced due to their increased mobility (to boost the processing speed of the devices), and the new architectures are required to reduce the junction leakage (and hence reduce the power consumption). These architectures are typically three-dimensional, and with the continuous decrease of dimensions, they also represent extremely confined volumes in which statistical and quantum effects start to play an increasing role. The entirely successful application of these new materials and architectures towards realizable technologies is facing some challenges. The most significant one is probably the impact of defects linked to growth processes and to the presence of stress. Indeed, the presence of different semiconductor materials with different lattice dimensions leads to crystalline defects, threading dislocations, and microtwins that affect the diffusion of dopants and the material mobility (due to scattering). When growth is performed in narrow trenches, dislocations are trapped within the confined volume (aspect-ratio trapping) and, theoretically, defect-free layers can be obtained. However, even if an apparently defect-free layer is obtained, the polar nature of the complex compound materials implies that antiphase boundaries can still be formed, which potentially represent important charge and recombination centers.

Beyond the standard logic/memory applications there is a very strong increase in “More than Moore” developments targeting energy (photovoltaic, energy storage), imaging (e.g., quantitat-

ive medical imaging), sensor/actuators linked to CMOS-base circuitry, biochips, etc. The utilization of graphene in order to process high mobility (both for holes and electrons) field-effect transistors is also being intensively studied.

In all these cases, metrology is a challenge, and no universal solution is identifiable. Moreover in many cases it becomes also very difficult to establish a complete assessment of accuracy, precision and spatial resolution due to a lack of appropriate 3-D standards and comparative metrology.

The development of high-performance devices (high speed and density, low consumption) is not the only objective of the electronic industry. The need for low-cost devices processed industrially on flexible and light substrates over very large surfaces has led to the emergence of electronic components based on organic semiconductors. The organic materials used nowadays are typically made of single molecules in highly ordered assemblies or of polymeric semiconductors in thin films. In recent years, an extensive set of organic-based prototypes (transistors, sensors, electrochromic devices, biosensors, photodiodes, photovoltaic cells, etc.) have been developed, demonstrating the strong potential of these materials. However, the advent of commercial applications often requires important breakthroughs towards more efficient and stable organic photovoltaic devices. This implies reduced exciton diffusion lengths (and thus more efficient collection) through the fabrication of an entangled mixture of the acceptor–donor layers, the addition of light scattering nanoparticles or metallic nanoparticles (spectrum harvesting through plasmonics) in the active layer or even wavelength convertors based on metal nanoparticles with a dye to shift the wavelengths. Improving the lifetime of organic solar cells requires incorporating optically transparent inorganic barriers in between the polymer films to prevent moisture penetration.

Unfortunately, these organic systems represent an even more challenging metrological problem as compared to their inorganic counterparts, as it no longer suffices to determine the atomic and electrical distributions, but one is also faced with the additional, equally important problem to trace, on the nanometer scale, the chemical configuration and the polymeric information.

It is therefore important to develop and improve two- and three-dimensional characterization techniques that can be utilized on both organic and inorganic semiconductors. These techniques should allow determination of the carrier/dopant distribution with an excellent sensitivity and repeatability (within 3 to 5%) with nanometer spatial resolution (subnanometer in inorganic and below 10 nm in organic) over a broad dynamic range (up to five decades). Ideally, they should also be able to probe the elemental distribution and to provide information on chemical bonding.

In this Thematic Series, we present the work of various leading labs in developing such techniques. Targeting 2-D/3-D resolution, one inevitably needs to look at scanning probe techniques that can be proclaimed to be dominant for electrical characterization and atomic probes that can be viewed as the ultimate in terms of compositional analysis.

At the same time we need to recognize that, notwithstanding the past efforts and achievements, there remains a considerable knowledge and performance gap between the state-of-the-art metrology and the future metrology requirements. Hence also some simulation work is presented in this Thematic Series.

Pierre Eyben

Leuven, April 2013

Beilstein Journal of Nanotechnology

Influence of diffusion on space-charge-limited current measurements in organic semiconductors

Thomas Kirchartz

Full Research Paper

Open Access

Address:
Department of Physics and Centre for Plastic Electronics, Imperial College London, South Kensington Campus SW7 2AZ, United Kingdom

Email:
Thomas Kirchartz - t.kirchartz@imperial.ac.uk

Keywords:
current–voltage curves; electron-only device; drift–diffusion; mobility; simulation; traps

Beilstein J. Nanotechnol. **2013,** *4,* 180–188.
doi:10.3762/bjnano.4.18

Received: 12 November 2012
Accepted: 27 February 2013
Published: 11 March 2013

This article is part of the Thematic Series "High-resolution electrical and chemical characterization of nm-scale organic and inorganic devices".

Guest Editors: E. Meyer and P. Eyben

Abstract

Numerical simulations of current–voltage curves in electron-only devices are used to discuss the influence of charged defects on the information derived from fitting space-charge-limited current models to the data. Charged, acceptor-like defects lead to barriers impeding the flow of electrons in electron-only devices and therefore lead to a reduced current that is similar to the situation where the device has a built-in voltage. This reduced current will lead to an underestimation of the mobilities and an overestimation of characteristic tail slopes if analytical equations are used to analyze the data. Correcting for the barrier created by the charged defects can, however, be a successful way to still be able to obtain reasonably accurate mobility values.

Introduction

A frequently used method to analyze charge carrier transport in organic semiconductors is based on space-charge-limited current measurements performed on single carrier devices [1-14]. These devices consist of two contacts that are either both electron-injecting or both hole-injecting, meaning that the current–voltage curve of these devices is not determined by the recombination of electrons and holes in the volume of the device [15] but instead by the mobility and concentration of carriers and the electric field in the device. If a device with two electron injecting contacts were doped to be sufficiently n-type that the electron concentration were determined by the doping and not by the injected charges in a certain range of voltages, the current–voltage curve in that range would be essentially ohmic, and the conductivity of the system would depend on mobility and electron concentration [16,17]. If the electron-only device were, however, undoped and the injection at the contacts efficient, the current density J would to a first approximation not depend on the equilibrium electron concentration anymore. Instead J would just depend on the mobility μ, which is typically the only unknown parameter, as well as the voltage V, the device thickness d and the permittivity $\varepsilon = \varepsilon_0\varepsilon_r$ and would ideally follow the Mott–Gurney law [18,19]

$$J = \frac{9}{8}\varepsilon_0\varepsilon_r\mu\frac{V^2}{d^3} \quad (1)$$

Here ε_0 is the vacuum permittivity and ε_r is the relative permittivity. The Mott–Gurney law is frequently used to determine the mobility of organic semiconductors used for light emitting diodes and solar cells. However, its derivation uses three assumptions that are often not applicable in organic semiconductors, namely that the device is trap-free, that diffusion is negligible and that the electric field at the injecting contact is zero. All three assumptions are in general not correct, in particular the assumption that there are no charged defects in organic semiconductors [20-26]. While there have been numerous attempts to develop models to take traps in unipolar devices into account [27-31], nearly all of them still rely on drift as the only transport mechanism. However, traps will often lead to a situation where diffusion currents cannot be neglected anymore, which makes analytical approximations for this situation problematic [7,10,13].

In this article numerical simulations are used to show how the presence of traps leads to deviations from the analytical equations typically used to analyze single-carrier current–voltage curves. I will focus on acceptor-like traps in electron-only devices, i.e., situations where the traps are negatively charged when below the Fermi level. These negative charges will behave like p-type dopants and create a barrier for electrons. The electrons first have to diffuse over the barrier created by the negatively charged defects before they drift to the other contact. This barrier leads to an exponential increase of current with voltage for low voltages similar to the situation in a bipolar diode with a nonzero built-in voltage. To understand the influence of the trap-induced barrier on the interpretation of current–voltage curves, current–voltage curves are simulated for different concentrations of traps using a drift–diffusion solver, and then analytical equations are fitted to the simulated curves to compare the apparent mobility and density of states derived from the fit to the ones that were used as input for the drift–diffusion simulation. The results of the simulations show that using analytical equations in electron-only devices with substantial concentrations of negatively charged defects can result in strongly underestimated mobilities and overestimated width of the exponentially decaying density of states.

Details of the simulation

The simulations are performed by using a commercial device simulator called Advanced Semiconductor Analysis (ASA) that was developed by the group of M. Zeman at the TU Delft (Netherlands) [32,33]. The software solves the Poisson equation

$$\Delta\varphi(x) = -\frac{\rho(x)}{\varepsilon_0\varepsilon_r} \quad (2)$$

and the continuity equations for the electrons and holes

$$-\frac{1}{q}\frac{dJ_n(x)}{dx} = -D_n\frac{d^2n(x)}{dx^2} - F(x)\mu_n\frac{dn(x)}{dx} = -R(x,n,p) \quad (3)$$

$$\frac{1}{q}\frac{dJ_p(x)}{dx} = -D_p\frac{d^2p(x)}{dx^2} + F(x)\mu_p\frac{dp(x)}{dx} = -R(x,n,p) \quad (4)$$

Here, q is the elementary charge, φ is the electrical potential, ρ is the space charge, x the spatial coordinate, n and p the free electron and hole concentrations, F the electric field, $D_{n,p}$ the diffusion constant, and J_n and J_p are the electron and the hole current. Note that the classical Einstein relation ($D_{n,p} = kT/q\ \mu_{n,p}$) is used to connect the diffusion constant and the mobility. The Einstein relation is applicable even in disordered semiconductors if the continuity equations are expressed in terms of free carriers, as has been done here. The occupation of the traps follows Shockley–Read–Hall statistics and is described in detail in [34-36]. I use a Gaussian distribution of traps

$$N(E) = N_T\frac{1}{\sigma_T\sqrt{2\pi}}\exp\left(-\frac{(E-E_T)^2}{2\sigma_T^2}\right) \quad (5)$$

with a peak energy E_T at midgap and a width of σ_T = 100 meV similar to the values used by Nicolai et al. [13]. The total trap concentration N_T was varied in the simulations. It is assumed that the defects are acceptor-like defects, i.e., that the defect is negatively charged if occupied with an electron and neutral when empty. The opposite situation would be a donor-like effect that is positively charged when empty (occupied by a hole) and neutral when occupied with an electron. The rationale of using acceptor-like defects is that many organic semiconductors are known to be p-type, i.e., to have acceptor like defects, and to show improved transport after compensation of the p-type dopants with n-type dopants [8,23,26,37,38].

Because organic semiconductors are generally disordered materials, it is important to investigate the effects of energetic disorder on the results of our simulations. In order to take the effect of disorder into account, a multiple trapping model together with exponential band tails is used in some simulations (Figure 3 and Figure 5, see below). The energy-dependent densities of states N_{CBT} and N_{VBT} of these tails follow

$$N_{\mathrm{CBT}} = N_0 \exp\left(\frac{E - E_{\mathrm{C}}}{E_{\mathrm{ch}}}\right) \quad (6)$$

for the conduction-band tail and

$$N_{\mathrm{VBT}} = N_0 \exp\left(-\frac{E - E_{\mathrm{V}}}{E_{\mathrm{ch}}}\right) \quad (7)$$

for the valence-band tail. Here, N_0 is a prefactor with the unit $1/(\mathrm{cm}^3 \cdot \mathrm{eV})$ and defines the concentration of tail states per volume and energy interval at the conduction band and valence band edge E_{C} and E_{V}. The conduction band tail is assumed to consist of acceptor-like defects and the valence band tail of donor-like defects [34,39]. It is assumed that the mobility of electrons is zero below the conduction band edge and has a constant value above, i.e., the influence from Poole–Frenkel type effects is neglected for simplicity. The slope of the tails is given by E_{ch} and assumed to be the same for the conduction and valence band in all cases. The boundary conditions at the contacts are defined by keeping the distance between conduction band edge and Fermi level constant at 0.1 eV for both contacts. Both contacts have high (10^5 cm/s) recombination velocities for electrons and holes (cf. [40] for an exact definition of the boundary conditions).

Results and Discussion

The influence of diffusion on the current–voltage curves

To understand the effect of charged defects on the current–voltage curve of electron-only devices it is most instructive to compare the simulated current–voltage curves with band diagrams. Figure 1 compares the situation with and without acceptor-like traps and depicts both the current–voltage curves as well as the band diagrams at $V = 1$ V forward bias (electrons are injected on the right and extracted on the left). Table 1 gives the parameters used for the simulations. Both simulated current–voltage curves are compared to the analytical equation (Mott–Gurney law) given by Equation 1. Interestingly, already the simulation without any traps is only well reproduced by the Mott–Gurney law at higher voltages, while its slope tends to be more ohmic ($\sim V$) than space-charge-limited ($\sim V^2$) at lower voltages. This phenomenon has been described in the past [41] and is related to the movement of the virtual cathode (the point of zero electric field) as a function of voltage. Figure 1b shows that the point of zero field is close to but not at the cathode, even in the cases without traps. In the derivation of the Mott–Gurney law it is assumed that the point of zero electric field is fixed at the actual cathode, which has previously been shown to be incorrect [10].

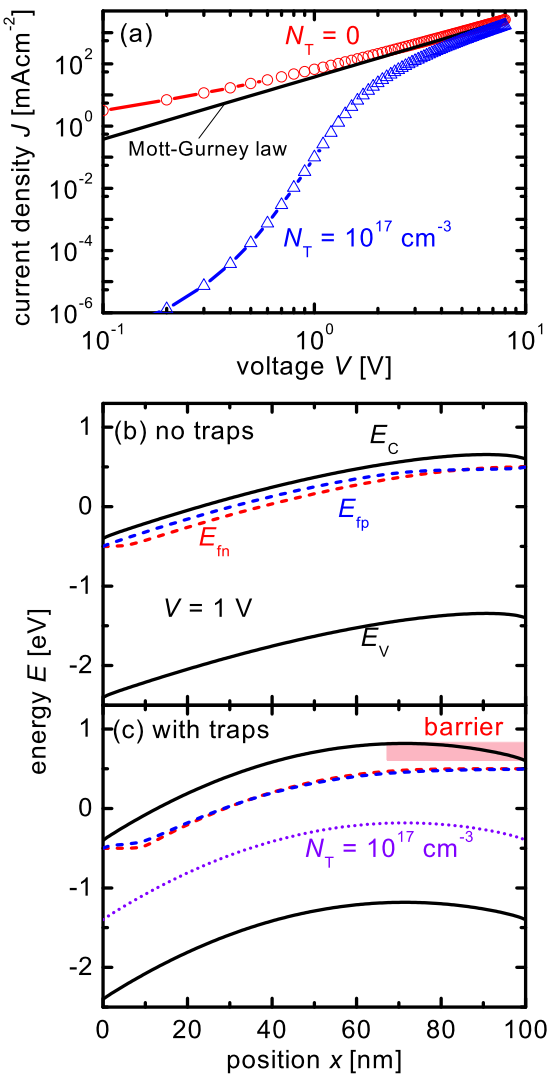

Figure 1: (a) Current–voltage curves of a device with and without charged acceptor-like defects with a total concentration N_T = 10^{17} cm^{-3} and a Gaussian width of σ = 100 meV are compared to the Mott–Gurney law (Equation 1). Band diagram of the device (b) without charged defects and (c) with charged defects. The acceptor-like defects in (c) create a barrier (indicated with a light red background) due to their negative charge. The diffusion of electrons up the barrier causes the reduced current in (a).

The most obvious effect, however, is that the current–voltage curve of the device with traps is strongly reduced at low voltages relative to both the simulation without traps and the Mott–Gurney law. This is due to the barrier formed by the charged defects as highlighted by the light red background in the band diagram in Figure 1c. The traps are essentially always below the quasi Fermi levels for electrons and holes and will therefore be occupied with electrons. The space charge of the electrons on the traps creates an electrostatic barrier (highlighted in red) close to the injecting contact that impedes the flow of electrons from the injecting cathode at $x = d$ towards the

Table 1: All the parameters used in the simulations, if not stated otherwise. For the definition of the capture coefficients see Figure 2 in [39]. The contact barrier is the distance between the Fermi level and conduction band edge at both contacts. This value is kept constant for all simulations except for the one with V_{bi} = 1 V in Figure 2, where the contact barrier at the cathode ($x = d$) is 0.1 eV and the contact barrier at the anode ($x = 0$) is 1.1 eV. The relative permittivity used in all simulations is $\varepsilon_r = 3.8$ and the capture coefficient for the Gaussian defect is 10^{-10} cm^3·s^{-1} for electrons and holes.

		no tails	with tails
figure no.		1–4	3,5
mobility	μ_0 [cm^2/Vs]	10^{-4}	10^{-3}
effective density of states	$N_C = N_V$ [cm^{-3}]	10^{20}	10^{20}
density of tail states	N_0 [eV^{-1}cm^{-3}]	0	10^{20}
characteristic tail slope	E_{ch} [meV]	0	variable or 50
capture coefficients (tails)	β_n^+ [cm^3·s^{-1}]	0	10^{-12}
	β_p^0 [cm^3·s^{-1}]	0	10^{-10}
	β_p^- [cm^3·s^{-1}]	0	10^{-12}
	β_n^0 [cm^3·s^{-1}]	0	10^{-10}
band gap	E_g [eV]	2.0	2.0
thickness	d [nm]	100	100
surface recombination velocity	S [cm/s]	10^5	10^5
contact barrier	φ_b [meV]	0.1	0.1

electron extracting contact at $x = 0$. The existence of this barrier means that more voltage has to be applied to achieve the same current flow than without the barrier. Thus, the current at a given voltage is reduced as seen in Figure 1a. In this context, it is not important where the energy level of the defect is; as long as it is an acceptor-like defect that is energetically below the quasi Fermi levels for electrons and holes, the behavior will be the same. However, when the Gaussian distribution of defects is close to the quasi Fermi level at a given voltage only part of the distribution will be occupied by electrons and therefore only part of the distribution will contribute to the band bending.

Apart from acceptor-like defects, also nonzero built-in voltages can lead to a situation where diffusion currents dominate the current–voltage curve at low voltages. Figure 2a shows the current–voltage curves of a device with a built-in voltage V_{bi} = 1 V as compared to the current–voltage curve of the device with traps that has been shown already in Figure 1. The built-in voltage is created by setting the distance $E_C - E_F$ = 1.1 eV at the extracting contact while keeping $E_C - E_F$ = 0.1 eV at the injecting contact. In both cases, the qualitative behavior is similar with a strongly reduced current at low voltages. The band diagrams in Figure 2b and Figure 2c are now depicted at short circuit and show that the shape of the barrier is completely different in both cases but the height correlates with the amount of reduction in current. The barrier in the case of the asymmetric contacts is 1 V and leads to a stronger reduction in current at low voltages than the smaller barrier in the case of the symmetric contacts with traps.

The determination of mobilities using analytical equations

This comparison between two types of barriers is relevant because the built-in voltage is often not known precisely [11] and it is customary to correct for its influence by using $V - V_{bi}$ as the voltage axis [4,5]. At first, this seems like a problem, because with the built-in voltage as a free parameter, it might be possible to erroneously assign the influence of a trap to a higher V_{bi}. To investigate that problem drift–diffusion simulations were performed for a device with $V_{bi} = 0$ but with a varying concentration of trap states, and the resulting current–voltage curves were fitted to the Murgatroyd equation [19]

$$J_{sclc} = \frac{9}{8}\varepsilon\mu\frac{{V_{eff}}^2}{d^3}\exp\left(\frac{0.89\beta\sqrt{V_{eff}}}{\sqrt{d}}\right) \quad (8)$$

that is frequently used to determine the mobility of organic semiconductors [9,42]. Here the parameter β controls the field dependence of the current that is meant to describe the Poole–Frenkel effect. However, in practice the factor β may be affected by the influence of traps and trap-induced diffusion currents. For the simulations shown in Figure 3 (see below), the voltage V_{eff} is defined as $V_{eff} = V - V_{bi}$ with V_{bi} being a fit parameter to understand the situation when the influence of traps is erroneously attributed to an increased V_{bi}.

Figure 3 shows the mobility resulting from the fit of Equation 8 to the numerical simulation normalized to the value that was

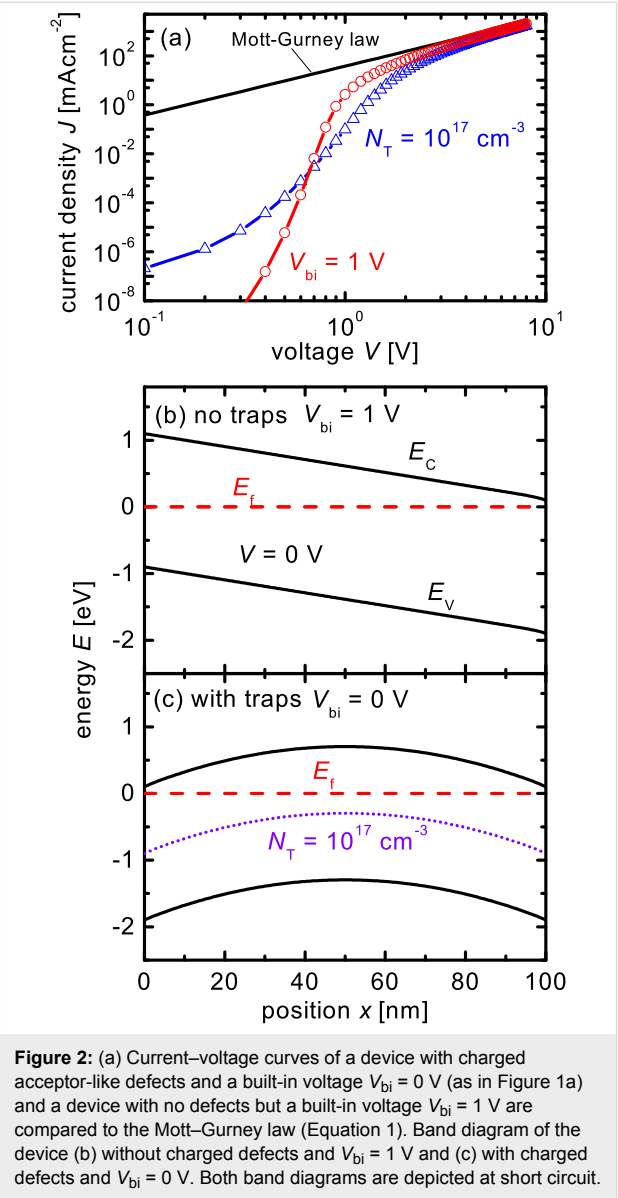

Figure 2: (a) Current–voltage curves of a device with charged acceptor-like defects and a built-in voltage V_{bi} = 0 V (as in Figure 1a) and a device with no defects but a built-in voltage V_{bi} = 1 V are compared to the Mott–Gurney law (Equation 1). Band diagram of the device (b) without charged defects and V_{bi} = 1 V and (c) with charged defects and V_{bi} = 0 V. Both band diagrams are depicted at short circuit.

used as input for the simulation ($\mu = \mu_n = \mu_p = 10^{-4}$ cm^2/Vs). Note that the results hardly change when changing the mobility in the range typical for organic semiconductors, therefore the absolute value of the mobility is of limited importance in this context. The simulated device is an electron-only device with a thickness of 100 nm. See Table 1 for the parameters used in the simulation. The first data set (line + filled squares) assumes that there are no exponential tails and it leads to a nearly perfect reproduction of the actual mobility. Thus, although the correction for V_{bi} is completely nonphysical the fitted mobilities are very close to the ones used as input for the simulations. Even in a case where there are exponential tails in addition to the variable concentration of midgap defects (line + open triangles), the correction for V_{bi} leads to a reasonably well approximated value for the mobility. Although there is a mismatch between fitted mobility and real mobility, this mismatch is only weakly dependent on the concentration of traps and not unexpected given that the Murgatroyd equation was not developed to deal with exponential tails. Note that in the case with exponential tails, the mobility is an effective value calculated as

$$\mu = \mu_0 \frac{n}{n + n_{\text{tail}}} \tag{9}$$

where μ_0 is the band mobility of the free electrons, n is the concentration of free electrons and n_{tail} the concentration of electrons trapped in the conduction band tail. The voltage at which the carrier concentrations are evaluated was arbitrarily chosen as V = 1 V. This effective value takes into account that only a part of the electrons is able to move and another part is trapped in the shallow tail states.

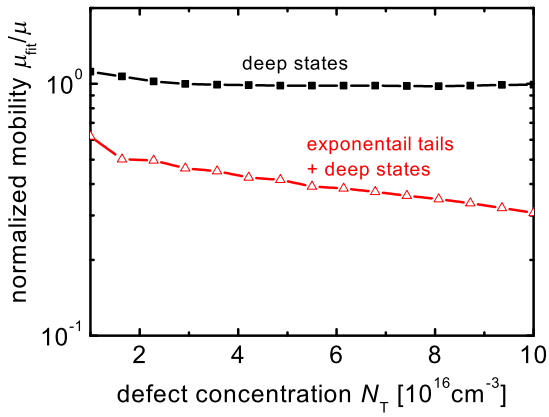

Figure 3: Normalized mobility obtained by fitting the Murgatroyd equation to the simulated current–voltage curves of electron-only devices as a function of the concentration of midgap defects. The fitted mobility is normalized to the actual mobility that is used as an input parameter in the simulation and the built-in voltage in Equation 8 is a free parameter. The actual built-in voltage used as input for the simulated current–voltage curves is zero. The comparison between fitted and actual mobility is done for two situations, one (lines + filled squares) with only a variable concentration of midgap defects and one (lines + open triangles) with the same variable concentration of defects and additional exponential tails.

If the built-in voltage in the fit of Equation 8 is set to the correct value of zero, obtaining the correct mobility using the Murgatroyd equation becomes impossible at high trap concentrations. Figure 4a shows the normalized mobility as a function of trap concentration for two different voltage ranges in which the Murgatroyd equation is fitted to the simulated data. Because the analytical equation neglects the predominant effect of diffusion at low voltages and high defect concentrations, the fits predict mobilities that are a strong function of defect concentration and that change dramatically depending on the voltage range that is analyzed. There are two voltage ranges in which the Murgatroyd equation can lead to a reasonable fit to the data.

For high voltages $V > 1$ V (see Figure 4b), the influence of space charge on the current–voltage curves is relatively weak and the Murgatroyd equation gives a good fit with a moderate uncertainty in mobility (one order of magnitude for a trap density $N_T = 10^{17}$ cm^{-3}). For low voltages $V < 1$ V, the exponential dependence of current density on $\sqrt{V_{eff}}$ can lead to a good fit by using high values of β and extremely low values of the mobility μ as shown in Figure 4c. In an ideal case with $V_{bi} = 0$ and a negligible series resistance it would not be possible to fit the whole range of voltages from around 0.1 V to $V >> 1$ V well by using the Murgatroyd equation. However, as shown in Supporting Information File 1, when correcting for series resistances the shape of a fit using the Murgatroyd equation can look very similar to a simulation with charged defects.

The result that good fits are possible if data is corrected for a voltage barrier means that the physical situations of having an actual built-in voltage (see Figure 2b) and having a concentration of traps that leads to a barrier for majority-carrier transport (Figure 2c) are similar in their effect on the current–voltage curve. In both cases, the device behaves like a series connection of a diode-like element (the barrier) and a space-charge-limited current regime. Correcting the voltage axis for the effective barrier will in both cases allow us to isolate the contribution from the space-charge-limited current regime. In this context it may therefore be more important to understand that there may be different origins of voltage barriers (the contacts or the properties of the bulk), than to actually use a different strategy to analyze the data in terms of mobilities. In addition, the results suggest that any data analysis based on interpreting the diffusion currents at low forward voltages in order to determine properties of traps [7,13] needs to exercise care in attributing the diffusion to bulk or contact effects (see Figure S1 in Supporting Information File 1). To discriminate between barriers due to bulk or contact effects, forward and reverse bias current–voltage curves should be analyzed. Because bulk effects would be symmetric while contact effects are not (see Figure S2 in Supporting Information File 1), the reverse-bias current–voltage curve may be used to determine the built-in voltage. An alternative method could be to measure the capacitance of the single-carrier device and analyze it as suggested by van Mensfoort and Coehoorn [43].

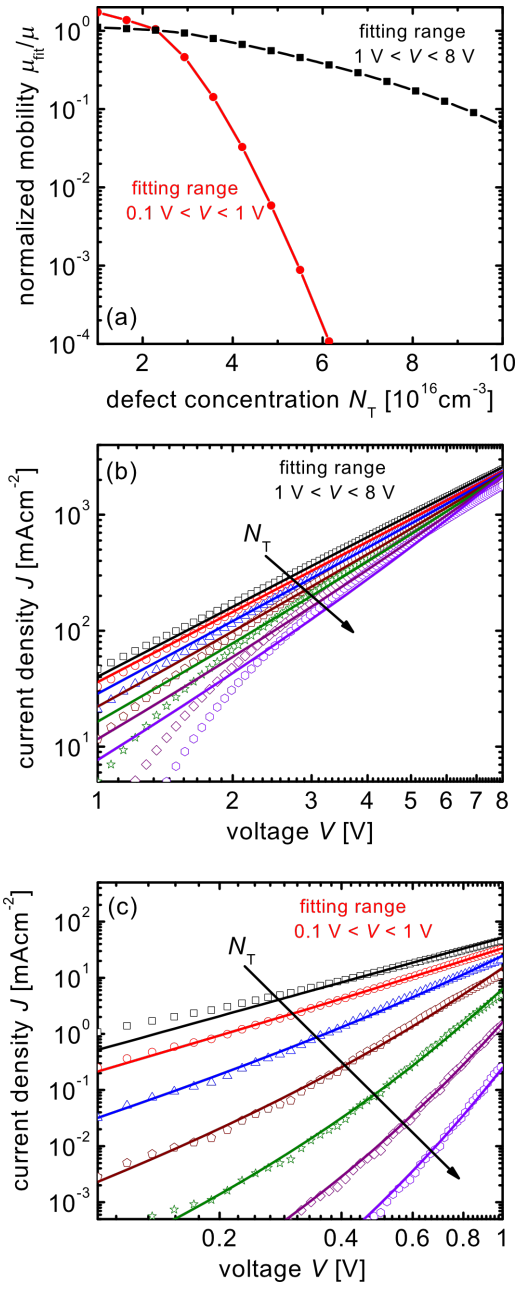

Figure 4: Normalized mobility as a function of defect concentration if the built-in voltage in Equation 8 is set to 0. Now, no correction for the barrier created by the charged defects is done and the mobility is underestimated at high trap concentrations. Because the current–voltage curve is affected by the traps mostly at low voltages, the mobility resulting from the fit will depend strongly on the range used for fitting. Reasonable fit quality is either reached if the fit is done for higher voltages $V > 1$ V or for lower $V < 1$ V. (b) and (c) show the fits (lines) to the drift–diffusion simulations (symbols) for the two different fitting ranges. Every second datapoint in (a) is presented in (b) and (c).

The determination of characteristic tail slopes from current–voltage curves

Although space-charge-limited current measurements are most frequently used to measure mobilities in organic semiconductors, there have been attempts to use the slope of the current–voltage curve on a log–log plot as a measure of the density of localized states. The density of localized states is an important property of the material, affecting both transport [44,45] and recombination [36,39,46-57], and one that can change as a function of device processing and during device degradation [55]. Usually, an exponential tail of states is assumed

that is characterized by a characteristic energy E_{ch} as defined in Equation 6 and Equation 7. Then, analytical equations are used, as for instance the one by Mark and Helfrich [28]. While the analytical approximations usually vary in their prefactors, they agree on the proportionality between current and voltage that follows [1,27,29,31,58]

$$J \propto V^{m+1} \tag{10}$$

where

$$m = \frac{E_{ch}}{kT} \tag{11}$$

This approximation, however, still requires diffusion currents to be negligible. Thus, it is useful to look at the relation between the tail slope that is used as input for the model and the tail slope determined from a fit of Equation 10 to the current–voltage curve. Figure 5 depicts this comparison for different values of the concentration of midgap defects. The more defects the system contains, the more diffusion will be relevant. Diffusion currents however, as shown in Figure 1a and Figure 2a, lead to a steeper increase of current with voltage than predicted by the Mott–Gurney law. This steep increase of current will be interpreted as a high value of m and therefore E_{ch}, when fitting Equation 10 to the data. Thus, for higher concentrations of charged acceptor-like defects, the tail slope determined by the fit (see Supporting Information File 1 for the fits and simulations) will overestimate the real tail slope. However, for intermediate and low concentrations of charged defects, Equation 10 actually underestimates the tail slope showing that even in intrinsic devices, the approximations of negligible diffusion and zero field at the cathode are not correct and lead to deviations between a full numerical model and the analytical approximation.

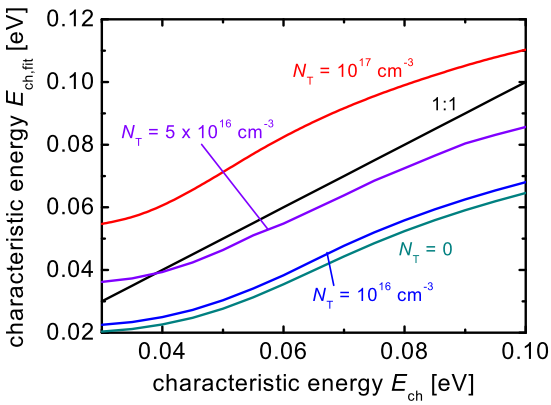

Figure 5: Comparison of the characteristic energy $E_{ch,fit}$ obtained by fitting Equation 10 to simulated current–voltage curves of electron-only devices assuming the characteristic energy E_{ch} of the tail states that was used as input in the simulation. A high concentration of defects (N_T = 10^{17} cm^{-3}) leads to a reduction of the current as shown in Figure 1a, which implies a much steeper slope of the curve in a certain voltage range. This will then be interpreted as a broader tail slope by Equation 10. If the concentration of defects is zero or low, Equation 10 will however underestimate the tail slope. The voltage range for the fits is 1 V < V < 8 V for the case with N_T = 10^{17} cm^{-3} and 0.1 V < V < 8 V for all other cases.

Conclusion

It has been shown that charged acceptor-like defects lead to barriers in electron-only devices that increase the relevance of diffusion currents. Because diffusion currents are always neglected when analytical equations are used to analyze either the mobility μ or the slope E_{ch} of an exponential band tail from single carrier devices, these defects will lead to incorrect results. Interestingly, when the voltage is corrected for a current-independent barrier, as is often done in practice to correct for a nonzero built-in voltage, the error in the mobility determined by fitting of an analytical equation and the one used as input for the simulation is low. In contrast, when the data is uncorrected, the mobility will both depend strongly on the voltage range of the fit and the concentration of charged defects. For instance, defect concentrations of N_T = 10^{17} cm^{-3} can lead to a fitted mobility that is several orders of magnitude smaller than the actual mobility. In case of the determination of the tail slope from the current–voltage curve of electron-only devices, a higher concentration of acceptor-like defects will lead to an overestimation and a lower concentration to an underestimation of the actual tail slope. Here it is important to note that even without any charged defects, the tail slope is not particularly well reproduced by the typically used analytical equations.

Supporting Information

Figure S1 shows the similarity between current–voltage curves affected by (i) a nonzero built-in voltage and (ii) space charge due to charged defects. The effect of built-in voltage on forward- and reverse-bias current–voltage curves is shown in Figure S2. Figure S3 discusses the effect of series resistances of fitting current–voltage curves with the Murgatroyd equation. Figures S4 to Figure S6 are the fits used to create Figure 5.

Supporting Information File 1

Additional simulations.
[http://www.beilstein-journals.org/bjnano/content/supplementary/2190-4286-4-18-S1.pdf]

Acknowledgements

T. K. acknowledges support by an Imperial College Junior Research Fellowship.

References

1. Beiley, Z. M.; Hoke, E. T.; Noriega, R.; Dacuña, J.; Burkhard, G. F.; Bartelt, J. A.; Salleo, A.; Toney, M. F.; McGehee, M. D. *Adv. Energy Mater.* **2011,** *1,* 954–962. doi:10.1002/aenm.201100204
2. Nicolai, H. T.; Wetzelaer, G. A. H.; Kuik, M.; Kronemeijer, A. J.; de Boer, B.; Blom, P. W. M. *Appl. Phys. Lett.* **2010,** *96,* 172107. doi:10.1063/1.3391668
3. Lenes, M.; Shelton, S. W.; Sieval, A. B.; Kronholm, D. F.; Hummelen, J. C.; Blom, P. W. M. *Adv. Funct. Mater.* **2009,** *19,* 3002–3007. doi:10.1002/adfm.200900459
4. Lenes, M.; Morana, M.; Brabec, C. J.; Blom, P. W. M. *Adv. Funct. Mater.* **2009,** *19,* 1106–1111. doi:10.1002/adfm.200801514
5. Mihailetchi, V. D.; Koster, L. J. A.; Blom, P. W. M.; Melzer, C.; de Boer, B.; van Duren, J. K. J.; Janssen, R. A. J. *Adv. Funct. Mater.* **2005,** *15,* 795–801. doi:10.1002/adfm.200400345
6. Mihailetchi, V. D.; van Duren, J. K. J.; Blom, P. W. M.; Hummelen, J. C.; Janssen, R. A. J.; Kroon, J. M.; Rispens, M. T.; Verhees, W. J. H.; Wienk, M. M. *Adv. Funct. Mater.* **2003,** *13,* 43–46. doi:10.1002/adfm.200390004
7. Nicolai, H. T.; Mandoc, M. M.; Blom, P. W. M. *Phys. Rev. B* **2011,** *83,* 195204. doi:10.1103/PhysRevB.83.195204
8. Lu, M. T.; Nicolai, H. T.; Wetzelaer, G.-J. A. H.; Blom, P. W. M. *J. Polym. Sci., Part B: Polym. Phys.* **2011,** *49,* 1745–1749. doi:10.1002/polb.22372
9. Azimi, H.; Senes, A.; Scharber, M. C.; Hingerl, K.; Brabec, C. J. *Adv. Energy Mater.* **2011,** *1,* 1162–1168. doi:10.1002/aenm.201100331
10. Dacuña, J.; Salleo, A. *Phys. Rev. B* **2011,** *84,* 195209. doi:10.1103/PhysRevB.84.195209
11. Dacuña, J.; Xie, W.; Salleo, A. *Phys. Rev. B* **2012,** *86,* 115202. doi:10.1103/PhysRevB.86.115202
12. Kuik, M.; Wetzelaer, G.-J. A. H.; Laddé, J. G.; Nicolai, H. T.; Wildeman, J.; Sweelssen, J.; Blom, P. W. M. *Adv. Funct. Mater.* **2011,** *21,* 4502–4509. doi:10.1002/adfm.201100374
13. Nicolai, H. T.; Kuik, M.; Wetzelaer, G. A. H.; de Boer, B.; Campbell, C.; Risko, C.; Brédas, J. L.; Blom, P. W. M. *Nat. Mater.* **2012,** *11,* 882–887. doi:10.1038/nmat3384
14. Faist, M. A.; Shoaee, S.; Tuladhar, S.; Dibb, G. F. A.; Foster, S.; Gong, W.; Kirchartz, T.; Bradley, D. D. C.; Durrant, J. R.; Nelson, J. *Adv. Energy Mater.* **2013,** in press. doi:10.1002/aenm.201200673
15. Wetzelaer, G. A. H.; Kuik, M.; Lenes, M.; Blom, P. W. M. *Appl. Phys. Lett.* **2011,** *99,* 153506. doi:10.1063/1.3651752
16. Jain, S. C.; Geens, W.; Mehra, A.; Kumar, V.; Aernouts, T.; Poortmans, J.; Mertens, R.; Willander, M. *J. Appl. Phys.* **2001,** *89,* 3804–3810. doi:10.1063/1.1352677
17. Zhang, X.-G.; Pantelides, S. T. *Phys. Rev. Lett.* **2012,** *108,* 266602. doi:10.1103/PhysRevLett.108.266602
18. Mott, N. F.; Gurney, R. W. *Electronic Processes in Ionic Crystals,* 1st ed.; Oxford University Press: New York, NY, 1940.
19. Murgatroyd, P. N. *J. Phys. D: Appl. Phys.* **1970,** *3,* 151. doi:10.1088/0022-3727/3/2/308
20. Gregg, B. A.; Gledhill, S. E.; Scott, B. *J. Appl. Phys.* **2006,** *99,* 116104. doi:10.1063/1.2201859
21. Liang, Z.; Nardes, A.; Wang, D.; Berry, J. J.; Gregg, B. A. *Chem. Mater.* **2009,** *21,* 4914–4919. doi:10.1021/cm902031n
22. Hains, A. W.; Liang, Z.; Woodhouse, M. A.; Gregg, B. A. *Chem. Rev.* **2010,** *110,* 6689–6735. doi:10.1021/cr9002984
23. Liang, Z.; Gregg, B. A. *Adv. Mater.* **2012,** *24,* 3258–3262. doi:10.1002/adma.201201157
24. Liang, Z.; Nardes, A. M.; van de Lagemaat, J.; Gregg, B. A. *Adv. Funct. Mater.* **2012,** *22,* 1087–1091. doi:10.1002/adfm.201102813
25. Khelifi, S.; Decock, K.; Lauwaert, J.; Vrielinck, H.; Spoltore, D.; Piersimoni, F.; Manca, J.; Belghachi, A.; Burgelman, M. *J. Appl. Phys.* **2011,** *110,* 094509. doi:10.1063/1.3658023
26. Bisquert, J.; Garcia-Belmonte, G. *J. Phys. Chem. Lett.* **2011,** *2,* 1950–1964. doi:10.1021/jz2004864
27. Lampert, M. A. *Phys. Rev.* **1956,** *103,* 1648–1656. doi:10.1103/PhysRev.103.1648
28. Mark, P.; Helfrich, W. *J. Appl. Phys.* **1962,** *33,* 205–215. doi:10.1063/1.1728487
29. Rose, A. *Phys. Rev.* **1955,** *97,* 1538–1544. doi:10.1103/PhysRev.97.1538
30. Woellner, C. F.; Freire, J. A. *J. Chem. Phys.* **2011,** *134,* 084112. doi:10.1063/1.3548884
31. Campbell, A. J.; Bradley, D. D. C.; Lidzey, D. G. *J. Appl. Phys.* **1997,** *82,* 6326–6342. doi:10.1063/1.366523
32. Zeman, M.; Krc, J. *J. Mater. Res.* **2008,** *23,* 889–898. doi:10.1557/jmr.2008.0125
33. Pieters, B. E.; Stiebig, H.; Zeman, M.; van Swaaij, R. A. C. M. M. *J. Appl. Phys.* **2009,** *105,* 044502. doi:10.1063/1.3078044
34. Pieters, B. E. Characterization of Thin-Film Silicon Materials and Solar Cells through Numerical Modelling. Ph.D. Thesis, Delft University of Technology, Delft, 2008.
35. Pieters, B. E.; Decock, K.; Burgelman, M.; Stangl, R.; Kirchartz, T. One-Dimensional Electro-Optical Simulations of Thin-Film Solar Cells. *Advanced Characterization Techniques for Thin Film Solar Cells;* Wiley-VCH Verlag GmbH & Co. KGaA: Weinheim, 2011; pp 501–527.
36. Kirchartz, T.; Nelson, J. *Phys. Rev. B* **2012,** *86,* 165201. doi:10.1103/PhysRevB.86.165201
37. Zhang, Y.; de Boer, B.; Blom, P. W. M. *Phys. Rev. B* **2010,** *81,* 085201. doi:10.1103/PhysRevB.81.085201
38. Lu, M.; Nicolai, H. T.; Wetzelaer, G.-J. A. H.; Blom, P. W. M. *Appl. Phys. Lett.* **2011,** *99,* 173302. doi:10.1063/1.3656735
39. Kirchartz, T.; Pieters, B. E.; Kirkpatrick, J.; Rau, U.; Nelson, J. *Phys. Rev. B* **2011,** *83,* 115209. doi:10.1103/PhysRevB.83.115209
40. Kirchartz, T.; Gong, W.; Hawks, S. A.; Agostinelli, T.; MacKenzie, R. C. I.; Yang, Y.; Nelson, J. *J. Phys. Chem. C* **2012,** *116,* 7672–7680. doi:10.1021/jp300397f
41. Grinberg, A. A.; Luryi, S. *J. Appl. Phys.* **1987,** *61,* 1181–1189. doi:10.1063/1.338165
42. Mihailetchi, V. D.; Xie, H. X.; de Boer, B.; Koster, L. J. A.; Blom, P. W. M. *Adv. Funct. Mater.* **2006,** *16,* 699–708. doi:10.1002/adfm.200500420
43. van Mensfoort, S. L. M.; Coehoorn, R. *Phys. Rev. Lett.* **2008,** *100,* 086802. doi:10.1103/PhysRevLett.100.086802
44. Choulis, S. A.; Nelson, J.; Kim, Y.; Poplavskyy, D.; Kreouzis, T.; Durrant, J. R.; Bradley, D. D. C. *Appl. Phys. Lett.* **2003,** *83,* 3812–3814. doi:10.1063/1.1624636
45. Chatten, A. J.; Tuladhar, S. M.; Choulis, S. A.; Bradley, D. D. C.; Nelson, J. *J. Mater. Sci.* **2005,** *40,* 1393–1398. doi:10.1007/s10853-005-0572-4
46. Garcia-Belmonte, G.; Boix, P. P.; Bisquert, J.; Lenes, M.; Bolink, H. J.; La Rosa, A.; Filippone, S.; Martin, N. *J. Phys. Chem. Lett.* **2010,** *1,* 2566–2571. doi:10.1021/jz100956d
47. Garcia-Belmonte, G.; Bisquert, J. *Appl. Phys. Lett.* **2010,** *96,* 113301. doi:10.1063/1.3358121
48. Tachiya, M.; Seki, K. *Phys. Rev. B* **2010,** *82,* 085201. doi:10.1103/PhysRevB.82.085201
49. Nelson, J. *Phys. Rev. B* **2003,** *67,* 155209. doi:10.1103/PhysRevB.67.155209

50. MacKenzie, R. C. I.; Kirchartz, T.; Dibb, G. F. A.; Nelson, J. *J. Phys. Chem. C* **2011,** *115,* 9806–9813. doi:10.1021/jp200234m
51. Schafer, S.; Petersen, A.; Wagner, T. A.; Kniprath, R.; Lingenfelser, D.; Zen, A.; Kirchartz, T.; Zimmermann, B.; Würfel, U.; Feng, X. J.; Mayer, T. *Phys. Rev. B* **2011,** *83,* 165311. doi:10.1103/PhysRevB.83.165311
52. Street, R. A.; Schoendorf, M.; Roy, A.; Lee, J. H. *Phys. Rev. B* **2010,** *81,* 205307. doi:10.1103/PhysRevB.81.205307
53. Street, R. A.; Song, K. W.; Northrup, J. E.; Cowan, S. *Phys. Rev. B* **2011,** *83,* 165207. doi:10.1103/PhysRevB.83.165207
54. Street, R. A. *Phys. Rev. B* **2011,** *84,* 075208. doi:10.1103/PhysRevB.84.075208
55. Street, R. A.; Krakaris, A.; Cowan, S. R. *Adv. Funct. Mater.* **2012,** *22,* 4608–4619. doi:10.1002/adfm.201200031
56. MacKenzie, R. C. I.; Shuttle, C. G.; Chabinyc, M. L.; Nelson, J. *Adv. Energy Mater.* **2012,** *2,* 662–669. doi:10.1002/aenm.201100709
57. Blakesley, J. C.; Neher, D. *Phys. Rev. B* **2011,** *84,* 075210. doi:10.1103/PhysRevB.84.075210
58. Paasch, G.; Scheinert, S. *J. Appl. Phys.* **2009,** *106,* 084502. doi:10.1063/1.3243283

License and Terms

Beilstein Journal of Nanotechnology

Photoresponse from single upright-standing ZnO nanorods explored by photoconductive AFM

Igor Beinik[1], Markus Kratzer[1], Astrid Wachauer[1], Lin Wang[1], Yuri P. Piryatinski[2], Gerhard Brauer[3], Xin Yi Chen[4], Yuk Fan Hsu[4], Aleksandra B. Djurišić[4] and Christian Teichert[*1]

Full Research Paper

Open Access

Address:
[1]Institute of Physics, Montanuniversität Leoben, Austria, [2]Institute of Physics, National Academy of Sciences, Kiev, Ukraine, [3]Helmholtz-Zentrum Dresden-Rossendorf, Institut für Strahlenphysik, Dresden, Germany and [4]Department of Physics, University of Hong Kong, P.R. China

Email:
Christian Teichert[*] - teichert@unileoben.ac.at

* Corresponding author

Keywords:
AFM; nanorods; photoconductive AFM; photoconductivity; ZnO

Beilstein J. Nanotechnol. **2013,** *4,* 208–217.
doi:10.3762/bjnano.4.21

Received: 14 November 2012
Accepted: 27 February 2013
Published: 21 March 2013

This article is part of the Thematic Series "High-resolution electrical and chemical characterization of nm-scale organic and inorganic devices".

Guest Editors: E. Meyer and P. Eyben

Abstract

Background: ZnO nanostructures are promising candidates for the development of novel electronic devices due to their unique electrical and optical properties. Here, photoconductive atomic force microscopy (PC-AFM) has been applied to investigate transient photoconductivity and photocurrent spectra of upright-standing ZnO nanorods (NRs). With a view to evaluate the electronic properties of the NRs and to get information on recombination kinetics, we have also performed time-resolved photoluminescence measurements macroscopically.

Results: Persistent photoconductivity from single ZnO NRs was observed for about 1800 s and was studied with the help of photocurrent spectroscopy, which was recorded locally. The photocurrent spectra recorded from single ZnO NRs revealed that the minimum photon energy sufficient for photocurrent excitation is 3.1 eV. This value is at least 100 meV lower than the band-gap energy determined from the photoluminescence experiments.

Conclusion: The obtained results suggest that the photoresponse in ZnO NRs under ambient conditions originates preferentially from photoexcitation of charge carriers localized at defect states and dominates over the oxygen photodesorption mechanism. Our findings are in agreement with previous theoretical predictions based on density functional theory calculations as well as with earlier experiments carried out at variable oxygen pressure.

Introduction

One-dimensional ZnO nanostructures, so called ZnO nanorods (NRs), exhibit technological potential for many device applications. Having a wide band gap (3.37 eV at room temperature) and high exciton binding energy (60 meV) and being piezoelectric, ZnO is one of the most promising semiconductor materials. Fields of application include solar cells [1-4], piezo-actuators [5], energy harvesting devices [6], and photosensors [7-16].

A common feature of wide-band-gap semiconductors, such as ZnO, GaN, etc., is the presence of deep levels in the forbidden gap. The appearance of such levels as well as the density of electronic states associated with them depends on the number of defects within a semiconductor and is determined very often by the growth conditions [17,18]. The number of defects in ZnO is also known to be dependent on a post-growth sample treatment and even storage time [19], which may substantially alter its properties. Besides that, a diverse range of electronic properties appears in response to different surface conditions. The surface conductivity of ZnO is highly dependent on the presence of adsorbates [20-23]. Such surface defects serve as binding sites for chemisorption processes and may contribute to the scattering and trapping of carriers [24], which lower the intrinsic conductivity of the material. Moreover, the exposure of ZnO surfaces to light irradiation induces photodesorption of oxygen molecules from the surface [22], which leads in turn to a rise of conductivity. Therefore, the photoresponse in ZnO is very often considered as an exclusively surface-induced process whereas the role of the bulk properties is negligible. It has been shown recently that the phenomenon of persistent photoconductivity in ZnO can also be attributed to the presence of oxygen vacancies in the bulk [25]. Thus, more precise confirmation of the origin of this phenomenon is required and the characterization of single, separated as-grown ZnO NRs is of great importance.

In this work, we focus on the investigation of opto-electronic properties of single as-grown ZnO NRs by means of conductive force microscopy (C-AFM) and photoconductive atomic force microscopy (PC-AFM) techniques. C-AFM allows simultaneous but independent probing of the topography and electrical properties at the nanoscale [26] and is well suited to study the electric peculiarities of semiconductor nanostructures [27-29] and ZnO NRs in particular [30,31]. The capability of C-AFM to characterize local photocurrents has already been demonstrated more than a decade ago [32]. Recently, a similar approach of so called PC-AFM has been used to map local photocurrents in different types of solar cells [33-36] and to perform local, AFM-based photocurrent spectroscopy [37,38].

In contrast to the first setups where the sample was illuminated through the substrate [32-34,38], we use here a configuration of PC-AFM where the sample is illuminated from the top as already successfully applied to Si and SiGe nanostructures [39,40]. Such a scheme allows us to stay away from any limitations imposed by the substrate. Here, we employ this technique to study the electrical transport in individual upright standing ZnO NRs grown by thermal evaporation [41]. The results obtained together with those of time-resolved photoluminescence (PL) suggest that the photoresponse in ZnO NRs originates preferentially from the photoexcitation of charge carriers from defect-localized states. The experimental findings are in good agreement with previous theoretical predictions based on density functional theory calculations [42] and will be discussed on the basis of the presence of oxygen vacancies.

Experimental

ZnO nanorods were grown by thermal evaporation of Zn in dry argon flow following a procedure described in more detail elsewhere [41]. The morphology of the resulting arrays of upright standing ZnO NRs was precharacterized by means of scanning electron microscopy (SEM) and intermittent contact mode AFM using PPP-NCHR™ probes from Nanosensors™ with a cantilever resonance frequency of approximately 330 kHz, a tip-curvature radius smaller than 10 nm, and a half-cone angle at the tip apex of about 10°. The applied forces have to be tuned carefully to avoid breaking the ZnO NRs [30,43]. For all experiments we used fresh probes as received from the provider without any additional treatment. Load-induced tip changes during the experiments could be ruled out by subsequent measurement of 2.5 nm high *para*-hexaphenyl islands grown on SiO_2 as a reference [44].

The local photoelectric properties of the NRs were investigated using an MFP3D™ AFM from Asylum Research equipped with the standard ORCA™ module which allows one to carry out C-AFM experiments and to measure currents in the range of 1 pA to 20 nA. We also used an external amplifier (Model 1211 from DL Instruments) in order to extend the range of measured currents during the investigation of transient photoconductivity and photocurrent spectroscopy. Unlike the ORCA module, the setup with an external amplifier does not provide the possibility of voltage ramping. Therefore, the current-to-voltage curves were exclusively measured with the ORCA module in the limited range of ±20 nA. In order to carry out PC-AFM experiments, the setup was extended with an external illumination system, which consists of a 150 W Xenon lamp (white-light source) connected to an Omni-λ 150 monochromator (LOT-Oriel, wavelength continuously tunable from about 300 nm to over 1 μm), an optical fiber, and several collimating lenses. A calibration curve, which accounts for both the transmittance of the optical system and the emission spectrum of the light

source, was recorded and used for the correction of the photocurrent spectra. The illumination from the AFM feedback laser diode, which has a wavelength of ≈850 nm, was also coupled to the illumination system. Nevertheless, the illumination at this wavelength does not affect the measurement since its wavelength lies in the region of transparency for ZnO.

We employed two different setups for measuring PC-AFM, which are described in the following. All measurements were carried out under ambient conditions on as-grown samples. The current–voltage (I–V) characteristics were recorded at the sample surface, which was under illumination directly from the optical fiber placed at an angle of about 15 to 20° with respect to the surface. For these measurements, we used a standard ORCA™ C-AFM holder and conductive diamond-coated DCP11™ probes from NT-MDT with a force constant of ≈5.5 N/m. The tip height for probes of this type is ca. 15–20 µm, which implies a restriction to the angle of illumination to the aforementioned 15–20° with respect to the sample surface due to shadowing. The illumination at large angle of incidence causes also an increase in the reflection from the surface, therefore the photoresponse is significantly suppressed in this configuration of illumination.

For the investigation of transient photocurrent and photocurrent spectroscopy from single upright-standing ZnO NRs, the following procedure was employed. ZnO NRs were located in intermittent contact mode, and then the system was switched to contact mode AFM for the investigation of the transient photocurrent behavior of ZnO NRs. The loading force during the transient PC-AFM characterization was on the order of 20–30 nN, which is sufficient to establish a stable contact, but does not result in NR bending. For these experiments, we used Pt coated ATEC-CONTPt™ probes [45] with the force constant k = 0.02–0.75 N/m, and with the tip (tip-curvature radius smaller than 20 nm) located at the very end of the cantilever and visible from the top. As is depicted in Figure 1, the use of such conductive probes allows illumination of the ZnO NRs through the AFM's optical system from the top.

To find the optimal probe location and to avoid possible probe damage, we performed imaging of the sample surface with the slow scan axis of the AFM switched off. After stable conditions were achieved, the conductive ATEC-CONTPt probe was located on the top facet of one of the upright-standing NRs, and the sample bias was applied. The photocurrent was recorded over a long period of time (ca. 3 h) at a sample bias of U_{smp} = −10 V. Such a high bias was applied to ensure a well detectable response. In order to determine the rise and decay time constants, we applied several cycles of illumination using white light (full spectrum) of the Xe lamp at 150 W.

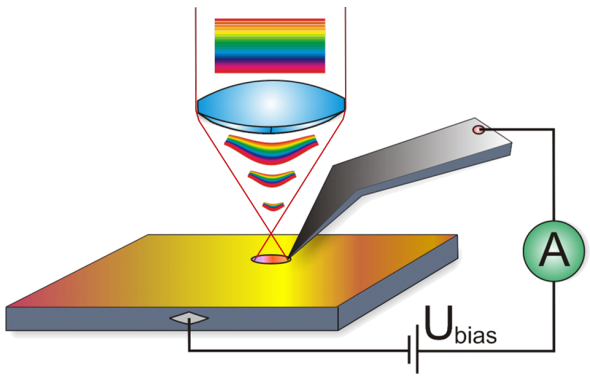

Figure 1: Schematic drawing of the PC-AFM setup. The sample in the present configuration was illuminated from the top side and biased. Use of ATEC-CONTPt™ probes helps to avoid shadowing by the cantilever.

The optical properties of ZnO NRs have been characterized macroscopically by means of time-resolved photoluminescence (TR-PL). The conventional steady-state PL and TR-PL were measured at 300 K. The monochromator used for both types of PL experiments has a linear dispersion of 0.8 nm/mm and was equipped with a photomultiplier tube as photodetector. The setup for the TR-PL experiments utilizes a stroboscopic oscilloscope with 0.1 ns gating registration system. As a source of optical excitation for PL measurements, we used the 337.1 nm emission line of a nitrogen laser with a pulse duration of 8 ns and a repetition rate of 100 Hz. PL emission was detected during the laser excitation pulse either at the leading edge of the laser excitation pulse (starting from ≈0.7 ns after the pulse onset), or at the trailing edge of the laser pulse after a variable delay time with respect to the onset of the laser pulse.

Results

As it is determined from the AFM image and the SEM micrograph presented in Figure 2a, the ZnO NR diameters vary in a wide range from 150 nm to 1.2 µm, whereas the rod lengths are ≈1.5 µm. Their cross-sectional shape is hexagonal; frequently it is even a regular hexagon. Their orientation is normal to the substrate surface with about 4% of the NRs deviating from the normal within about ±30°. Photoluminescence spectra of a ZnO NR array recorded using the 337 nm line of a pulsed nitrogen laser are presented in Figure 2b. The red curve shows the steady-state PL spectrum, each point on the plot averages the PL signal measured over approximately one second. The blue curve represents a TR-PL spectrum where each point was measured in a time frame from 0 to 0.7 ns from the moment of excitation.

Figure 3 shows the influence of illumination on the I–V characteristics of a single upright-standing ZnO NR. The dark and

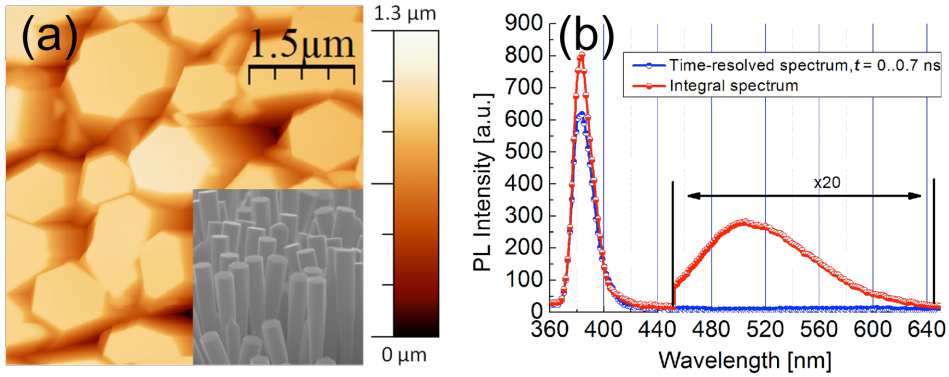

Figure 2: (a) 5 µm × 5 µm intermittent contact mode AFM image and SEM micrograph (inset) of ZnO nanorods grown by thermal evaporation, (b) time-resolved (blue curve) and integral (red curve) PL spectra from the array of upright standing ZnO nanorods, of photoluminescence obtained at 300 K.

illuminated *I–V* characteristics were both recorded with 30 s delay between the measurements, the voltage was applied to the substrate and ramped forth and back with a rate of 20 V/s. The *I–V* curve was first measured in the dark, then under illumination. A repetition of this sequence after an additional delay of ca. 10 min did not yield any changes in the characteristics.

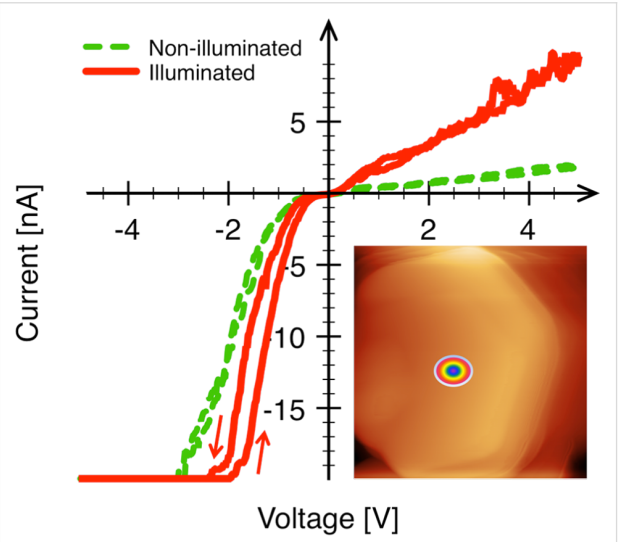

Figure 3: Current–voltage characteristics of dark (green curve, dashed) and illuminated state (red curve, solid) recorded from a single upright-standing ZnO nanorod by using a standard ±20 nA range amplifier. The illuminated characteristic was recorded by shining white light (150 W Xe lamp) at an angle of ca. 15–20° onto the sample. The arrows at the bottom indicate the direction of the voltage ramp.

Both, illuminated and dark characteristics demonstrate rectifying behavior with a rather significant deviation of the reverse current from the zero level. Moreover, the reverse current in both cases demonstrates a linear dependence on the applied voltage, which can be attributed to the photoexcitation of charge carriers from the valence band to a defect-perturbed host state (PHS, depicted as transition (3) in Figure 6, see below). The *I–V* characteristics recorded from ZnO NRs under illumination are degenerated with high currents at reverse (positive) sample bias, which indicates an increase of the charge-carrier concentration. The rectifying *I–V* characteristics are associated with the Schottky contact between AFM tip and ZnO NR. The Schottky barrier heights (SBHs) were estimated, using the same method as applied in [31], to be 0.22 ± 0.06 eV for the dark and 0.18 ± 0.06 eV for the illuminated case. The corresponding ideality factor was ≈2.2 in both cases.

In Figure 4, we present the PC-AFM results for a single ZnO NR under illumination from the top using the setup shown in Figure 1. Here, a bias of $U_{smp} = -10$ V has been applied to the substrate and the current was measured as a function of time in the dark and under illumination. For illumination, the full spectrum of the Xe-lamp was used. The transient photocurrent curve recorded during the first cycle of the illumination is shown in Figure 4a. The bias was applied at time 0, which caused a current jump from 0 to 12 mA, followed by an exponential current decrease (blue shaded area in Figure 4a), which can be fitted well by:

$$I = I_0 + C_1 e^{-(t-t_0)/\tau} \quad (1)$$

where t is time, τ is the decay time constant, t_0 is the decay time offset, I_0 and C_1 are the offset and amplitude of the current decay, respectively. The time constant of the dark current decay after the initial application of sample bias was determined to be $\tau \approx 18$ s.

The illumination of the sample surface for the first cycle was started at $t = 75$ s and stopped at $t = 300$ s when the current was saturated. After the illumination was switched on, the photocur-

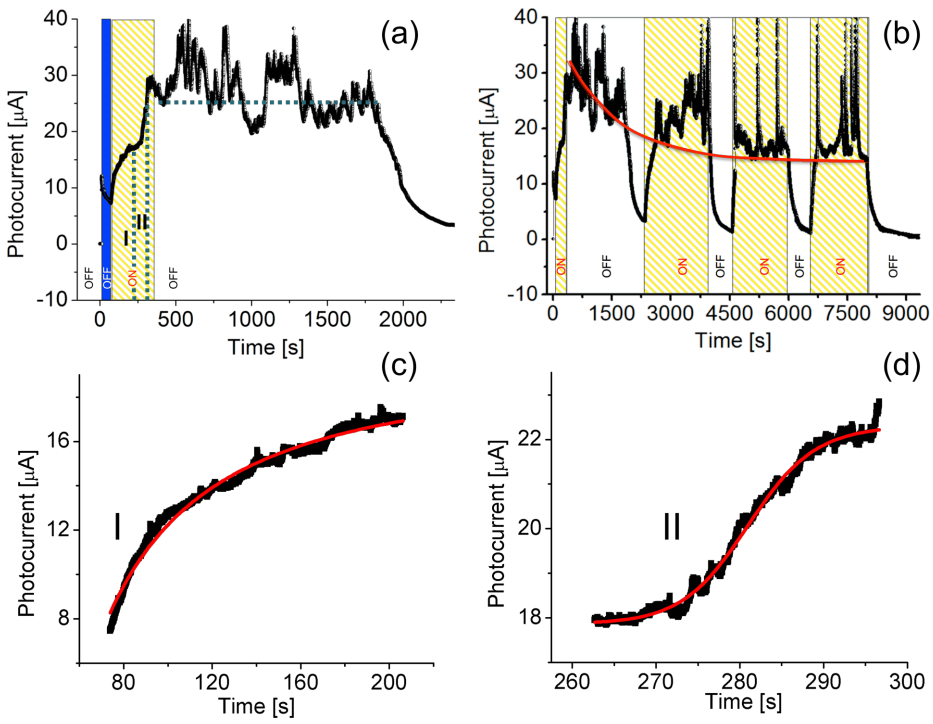

Figure 4: (a) Photocurrent rise and relaxation during the first cycle of the experiment. The bias of −10 V was applied at 0 s, the blue shaded area indicates the initial dark current decay. After the illumination was switched on the photocurrent rose in two steps, which are separated on the figure by vertical dashed lines and marked as I and II. (b) Several cycles of the illumination; the sample bias is −10 V, the source of illumination is a 150 W Xe lamp (white-light source). The periods under illumination are marked by the yellow shaded areas. (c), (d) First two steps of the photocurrent increase, marked as I and II in (a), fitted by Equation 2 (red curves).

rent raised in two steps. Each step of this raise is best approximated by the so called logistic equation:

$$I = I_i + \frac{I_f - I_i}{1 + (t / t_0)^p} \qquad (2)$$

where p is a number that can take various real values, increasing with p = 1.5 for the first step, t_0 is the rise-time offset, and I_i and I_f are the initial and final current levels. These first two steps of the photocurrent increase marked as I and II in Figure 4a fitted by Equation 2 (red curves) are presented in Figure 4c and Figure 4d, respectively. Surprisingly, the photocurrent persisted at about the level of saturation from t = 500 s to t = 1835 s (marked by the horizontal dashed line in Figure 4a). There are instabilities in the form of pronounced current spikes and slumps, which appear randomly and originate likely from mechanical instabilities in the tip-to-sample contact. At t = 1835 s the current abruptly decreases, which again can be well fitted by Equation 1. In this case the best fit yields a decay time constant of $\tau \approx 163$ s.

Figure 4b shows in addition to the first cycle further cycles of illumination of the sample and corresponding transient photocurrent behavior. During all cycles, excluding the first one, the photocurrent raised, reached the saturation level, and stayed there until the illumination was switched off. The exponential current decrease in each cycle is well fitted by Equation 1 resulting in an average decay time constant of τ = 140 ± 20 s, and the corresponding average raise time constant, also determined from Equation 1, is equal to τ = 20 ± 9 s. The slow return of the dark current value after illumination, known as persistent photoconductivity, has frequently been reported for ZnO material [22,46]. Interestingly, the saturation level is decreasing in time. When fitted, by using again Equation 1 (red curve in Figure 4b), it gives a decay time constant of $\tau \approx 1400$ s for the saturation level. The transient photocurrent experiments performed on a single separated NR provide information about the characteristic rise and decay time of the photoresponse. An interesting peculiarity of the transient photocurrent measured at different ZnO NRs is the already mentioned observation that the current initially stays at the saturation level during the first cycle of the illumination, even when illumination is switched off, and then rapidly decays. In principle, this behavior can be caused by several mechanisms, such as water dissociation and desorption, recharging of defects, etc. We believe that this phenomenon should be considered as a current-induced electrochemical process as we will argue in the discussion.

In order to gain insight into the electronic structure of single upright standing ZnO NRs, we measured the spectral characteristics of the photocurrent by means of PC-AFM. The result of these measurements at a sample bias of −10 V is presented in Figure 5. The photocurrent spectra were measured starting from longer wavelengths with a time delay varying in the range from 30 s to 2 min between acquisition of two neighboring data points. This time delay was sufficient to account for the time needed for photocurrent saturation. Each data point in the photocurrent spectrum represents the average value of 100 points measured at 1 kHz acquisition rate. In addition to the measured data (Figure 5a), we present also the extrapolation of the normalized spectrum to $I_{PN} \cdot \hbar\omega = 0$ (Figure 5b). The latter provides the energy corresponding to the transition involved in the photocarrier generation process. Interestingly, it has been found that the NRs are already sensitive to illumination with a wavelength of 400 nm, i.e., with a corresponding photon energy of 3.1 eV which is smaller than the band gap of ZnO (3.37 eV).

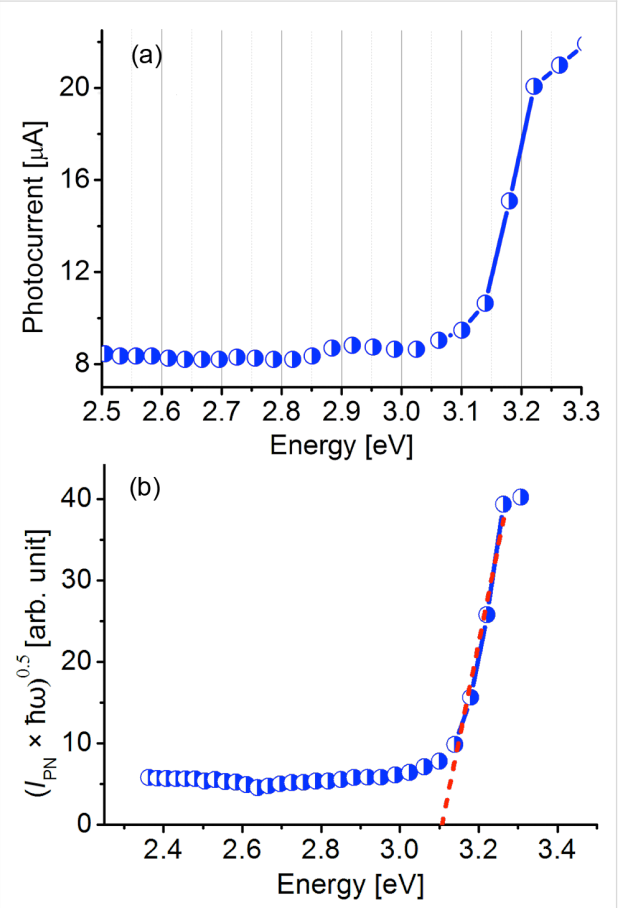

Figure 5: (a) The photoconductivity spectral response from a single upright standing ZnO NR recorded using a 150 W Xe lamp connected to the monochromator. The sample bias was −10 V. (b) The quantum efficiency of light conversion linearized in coordinates $(I_{PN}\hbar\omega)^{0.5}$ versus $\hbar\omega$. The dashed line represents extrapolation of the linearized region until the intersection with the x-axis.

Discussion

The standard model to explain the photoresponse in ZnO involves the photodesorption of oxygen molecules [22]. Adsorption of oxygen on the ZnO surface causes the capture of electrons leading to the formation of a negatively charged layer and a depletion region near the surface. The presence of adsorbed oxygen introduces a trap surface state within the band gap. The probability of population of this state drops with an increasing amount of oxygen adsorbed on the surface. As a result, the process of electron transport from the bulk to the surface is also becoming slower. The level of saturation is achieved when the energy of the trap state reaches the Fermi level due to the band bending. It is generally assumed that when the surface is exposed to light with photon energies higher than the band gap in ZnO, electron–hole pairs are created [22]. Then, the holes move toward the surface in the electric field of the surface depletion region and recombine with the electrons there $[h^+ + O_2^- \rightarrow O_2(g)]$. This results in an excess of electrons, which were generated by the light absorption contributing to the photocurrent when the sample is biased. This model implies also that the photoconductivity in ZnO is limited to the fundamental absorption range (i.e., for photon energies higher than the band gap). For photon energies smaller than the band gap, the conductivity could increase only at the expense of photoexcited electrons from defect levels. This process excludes the generation of free holes and photodesorption due to the recombination of free holes with trapped electrons on the oxygen molecules. Moreover, the slow kinetics of the photocurrent decay, even under high oxygen partial pressures, is not explained satisfactorily by this model. The photocurrent spectrum presented in Figure 5a reveals that the sample becomes photosensitive at ≈400 nm (3.1 eV). To estimate a band-gap energy that could be compared with the values derived from the PL experiments, we normalized the data presented in Figure 5a taking into account the emission spectrum of our light source (i.e., we switched to the presentation of the characteristic of quantum efficiency of light conversion). A linearization of the data by plotting in coordinates $(I_{PN}\hbar\omega)^{0.5}$ versus $\hbar\omega$, where the I_{PN} is the normalized photocurrent for incident photons of energy $\hbar\omega$, is presented in Figure 5b. An extrapolation of the linear region marked by the dashed line in Figure 5b yields the transition energies involved in the photocarrier generation process. The obtained value $E_{\min} \approx 3.1$ eV is the minimum photon energy sufficient for the photoexcitation of mobile charge carriers.

The value of 3.1 eV turned out to be at least 100 meV lower than the band gap energy determined from the PL experiments as will be discussed in the following. The TR-PL spectra presented in Figure 2b reveal both band-edge and defect emission. There a strong peak at 383 nm (3.2 eV), which occurs

within 0.7 ns after onset of the excitation pulse can be attributed to the emission of localized excitons. Therefore, the absorption of light with photon energies of 3.2 eV and higher may lead to the generation of excitons with possible subsequent dissociation into free charge carriers. The broad band visible in Figure 2b (integral spectrum) with the maximum at 504 nm is commonly attributed to the presence of oxygen vacancies [17]. The crystalline quality can be estimated by a simple comparison of the intensities of the exciton peak and defect band. From the PL measurements we conclude that the generation of electron–hole pairs at room temperature becomes possible with a photon energy $\hbar\omega \geq 3.2$ eV under the formation of free excitons, indicative of the possible presence of oxygen vacancies. Based on the latter findings, we conclude that the experimentally observed photocurrent cannot be simply explained by band-to-band transition with subsequent electron–hole pair generation and oxygen desorption, as assumed in the standard model [22].

A theoretical explanation of the persistent photoconductivity in ZnO, which also explains the lowering of the minimum photon energy, has been provided by Lany and Zunger on the basis of density functional theory calculations [42]. The corresponding energy-level diagram also accounting for the band bending due to surface states is presented in Figure 6. The model involves a two-step process where an oxygen vacancy V_O changes its state from nonconductive (α-configuration of defect localized state (DLS), V_O^0) to conductive (β-configuration of DLS, $V_O^{2+} + 2e^-$) with the subsequent appearance of a PHS below the conduction band minimum under illumination. Recently, this model was also supported by experiments carried out under different oxygen levels [10]. The electrons from the energy level that corresponds to the α-configuration are photoexcited to the conduction band contributing to the photocurrent. The existence of the PHS state implies also a trapping of the mobile charge carriers in this state. The transition back to the nonconductive state requires a simultaneous thermal activation of the electrons from the PHS state to the conduction band and capturing them back at the defect. Both conditions, thermal excitation from the PHS and capture by the DLS, have to be fulfilled simultaneously, which implies slow kinetics for the photocurrent decay. The presence of the PHS state makes a transition from the valence band to the PHS state possible, which leads to the formation of holes and therefore to an increase in p-type conductivity under illumination. In fact, both experimental observations, i.e., the photoresponse for illumination at wavelengths from 400 nm on (Figure 5) as well as the increased p-type conductivity upon light exposure (Figure 3), are consistent with the model of Lany and Zunger provided the presence of defect states around 100 meV above the ZnO valence band edge.

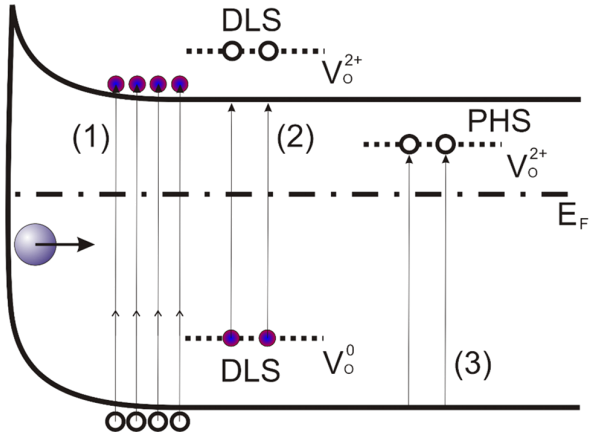

Figure 6: Schematic energy-level diagram of ZnO taking into account the existence of theoretically predicted [42] α- and β-type configurations of oxygen vacancies. The processes of electron–hole pair generation via band-to-band absorption, charge carrier photoexcitation from a defect localized state (DLS) and to a perturbed host state (PHS) of an oxygen vacancy are marked as (1), (2) and (3), respectively.

Indeed it has been demonstrated and discussed in a recent paper [47] that the difference between the nominal band gap $E_g = 3.37$ eV at 300 K known for ZnO and the optically determined band gap values E_g^{opt}, being at least 100 meV smaller, indicates the presence of optically active defects in all ZnO samples investigated. This means that the corresponding defects are characterized by this energetic amount from either the valence or conduction band within the band gap. The true nature of these defects still has to be determined and may depend on the method of crystal growth. Thereby, an involvement of hydrogen cannot be excluded and should at least be considered as well [43,47].

A further point to discuss is the observed transient current behavior. Especially, the deviation of the current evolution during the first cycle of illumination compared to the successive illumination cycles is puzzling. When the illumination was switched off after the initial light exposure, the current remained fluctuating around the level of saturation (marked by the dashed line in Figure 4a) for about 21.6 min and then dropped exponentially. Although we observe this behavior reproducibly for different NRs, we can still only speculate on the origin of this phenomenon. In fact several contributions may occur. Initially, the ZnO surface under the AFM tip is covered with adsorbates such as water and oxygen. Under the applied conditions, the water layer may be several monolayers thick. Once the current rises the initial surface conditions will be changed due to electrochemical processes, electromigration and local power dissipation. One of the major changes will be a reduction of the water present due to thermal desorption. On the

one hand, this changes the contact properties significantly and on the other hand, the contact becomes more stable. Obviously, this situation occurs only in the first cycle. For all successive illumination cycles the exponential current decrease set in immediately when the light was switched off. Additionally, a decrease of the photocurrent saturation level with an increasing number of illumination cycles is observed. Such a behavior might be explained by different mechanisms. The pronounced current fluctuations around the current saturation level are most likely caused by contact instabilities, even though the experiments were carried out in a regime where the tip loading force should be sufficient to provide a stable contact.

It should also be noted that the current level is in the μA range, which leads to a considerable power dissipation and heating of the contact between AFM tip and NR. For the applied contact forces, the effective contact radius between AFM tip and ZnO NR can be estimated to be $r_C \approx 1.6$ nm [48-53]. Assuming that most of the applied potential drops across the AFM-tip–NR contact, the average dissipated power at the contact is $P = U \cdot I \approx 0.25$ mW. Since the effective contact radius is small compared to the radius of curvature of the AFM tip (≈20 nm), the contact region may be modeled as a flat disc with diameter $2r_C$ and the NR as a semi-infinite solid (NR diameter >> $2r_C$). For this case, $\Delta T \approx 0.5 \cdot P/(k_{th} \cdot 4r_C) = 195$ K [54], with the thermal conductivity of ZnO, $k_{th}(\text{ZnO}) \approx 100\ \text{W}\cdot\text{m}^{-1}\cdot\text{K}^{-1}$ [51]. The factor 0.5 was introduced to take into account that a part of the energy dissipated at the contact is conducted via the tip. This means that local NR temperatures of at least 495 K can be expected. Further evidence for a pronounced temperature increase at the contact point can be found by comparing the SBHs obtained in a previous study [31]. There, an amplifier with higher gain, allowing lower currents, was used. The SBH between a diamond coated tip and the ZnO NR was determined to be 0.54 eV. The large difference between the 0.22 eV found here and the 0.54 eV can be simply explained by a higher junction temperature induced by the higher current. On the one hand, this "heating" affects the surface properties due to increased desorption, and on the other hand it might lead to a local annealing of the nanorod. Since the resulting annealing takes place in an oxygen-rich environment, a decrease of the ZnO oxygen vacancies near the contact region is possible. It has been shown recently that annealing at temperatures below 700 K already has an effect on the structural and optical properties of ZnO [55,56]. This could be responsible for the quenching of the saturation current with increasing number of illumination repetitions (indicated by the red curve in Figure 4b). Within the size range of the NRs investigated here, no indication of a size-dependent photoresponse was noticed. A systematic study on the size dependence has not been performed yet and is a topic for future investigations.

Conclusion

A novel PC-AFM technique enabling sample illumination from the top has been implemented to study the optoelectronic properties of individual upright-standing ZnO nanorods under ambient conditions. The corresponding photocurrent spectrum revealed that the minimum photon energy sufficient for photocurrent excitation is 3.1 eV. This value turns out to be at least 100 meV lower than the band-gap energy determined from macroscopic photoluminescence experiments. This is inconsistent with the frequently applied model for ZnO photoconductivity involving electron–hole pair generation by light induced band-to-band excitation and subsequent oxygen desorption as a surface process [22]. We suggest instead that the observed peculiarities of photoconductivity under ambient conditions can be attributed to the presence of defect states in the band gap. In fact, our findings support theoretical predictions based on density functional theory calculations [42], which state the presence of oxygen defect states above the valence band edge. Our observations also agree well with earlier experiments carried out at variable oxygen pressure [10]. The observed transient photocurrent may also be related to the local annealing of oxygen defects due to power-dissipation heating at the nanocontact formed between the ZnO NR and the conductive AFM tip.

Acknowledgements

This work was financially supported by the Austrian Science Fund (FWF) under Project No. P19636-N20.

References

1. Baxter, J. B.; Aydil, E. S. *Appl. Phys. Lett.* **2005,** *86,* 053114. doi:10.1063/1.1861510
2. Law, M.; Greene, L. E.; Johnson, J. C.; Saykally, R.; Yang, P. *Nat. Mater.* **2005,** *4,* 455–459. doi:10.1038/nmat1387
3. Olson, D. C.; Piris, J.; Collins, R. T.; Shaheen, S. E.; Ginley, D. S. *Thin Solid Films* **2006,** *496,* 26–29. doi:10.1016/j.tsf.2005.08.179
4. Ji, L. W.; Shih, W. S.; Fang, T. H.; Wu, C. Z.; Peng, S. M.; Meen, T. H. *J. Mater. Sci.* **2010,** *45,* 3266–3269. doi:10.1007/s10853-010-4336-4
5. Wang, Z. L. *Mater. Sci. Eng., R* **2009,** *64,* 33–71. doi:10.1016/j.mser.2009.02.001
6. Wang, Z. L.; Song, J. *Science* **2006,** *312,* 242–246. doi:10.1126/science.1124005
7. Lupan, O.; Chow, L.; Chai, G. *Sens. Actuators, B* **2009,** *141,* 511–517. doi:10.1016/j.snb.2009.07.011
8. Lupan, O.; Chai, G.; Chow, L.; Emelchenko, G. A.; Heinrich, H.; Ursaki, V. V.; Gruzintsev, A. N.; Tiginyanu, I. M.; Redkin, A. N. *Phys. Status Solidi A* **2010,** *207,* 1735–1740. doi:10.1002/pssa.200983706
9. Yadav, H. K.; Sreenivas, K.; Gupta, V. *Appl. Phys. Lett.* **2010,** *96,* 223507. doi:10.1063/1.3427417
10. Hullavarad, S.; Hullavarad, N.; Look, D.; Claflin, B. *Nanoscale Res. Lett.* **2009,** *4,* 1421–1427. doi:10.1007/s11671-009-9414-7

11. Zhou, J.; Gu, Y.; Hu, Y.; Mai, W.; Yeh, P.; Bao, G.; Sood, A. K.; Polla, D. L.; Wang, Z. L. *Appl. Phys. Lett.* **2009,** *94,* 191103. doi:10.1063/1.3133358
12. Kim, W.; Chu, K. S. *Phys. Status Solidi A* **2009,** *206,* 179–182. doi:10.1002/pssa.200824338
13. Cheng, G.; Li, Z.; Wang, S.; Gong, H.; Cheng, K.; Jiang, X.; Zhou, S.; Du, Z.; Cui, T.; Zou, G. *Appl. Phys. Lett.* **2008,** *93,* 123103. doi:10.1063/1.2989129
14. Law, J. B. K.; Thong, J. T. L. *Appl. Phys. Lett.* **2006,** *88,* 133114. doi:10.1063/1.2190459
15. Guo, Z.; Zhao, D.; Liu, Y.; Shen, D.; Zhang, J.; Li, B. *Appl. Phys. Lett.* **2008,** *93,* 163501. doi:10.1063/1.3003877
16. Hu, Y.; Zhou, J.; Yeh, P.-H.; Li, Z.; Wei, T.-Y.; Wang, Z. L. *Adv. Mater.* **2010,** *22,* 3327–3332. doi:10.1002/adma.201000278
17. Djurišić, A. B.; Leung, Y. H. *Small* **2006,** *2,* 944–961. doi:10.1002/smll.200600134
18. Djurišić, A. B.; Ng, A. M. C.; Chen, X. Y. *Prog. Quantum Electron.* **2010,** *34,* 191–259. doi:10.1016/j.pquantelec.2010.04.001
19. Merz, T. A.; Doutt, D. R.; Bolton, T.; Dong, Y.; Brillson, L. J. *Surf. Sci.* **2011,** *605,* L20–L23. doi:10.1016/j.susc.2010.12.021
20. Collins, R. J.; Thomas, D. G. *Phys. Rev.* **1958,** *112,* 388–395. doi:10.1103/PhysRev.112.388
21. Shapira, Y.; McQuistan, R. B.; Lichtman, D. *Phys. Rev. B* **1977,** *15,* 2163–2169. doi:10.1103/PhysRevB.15.2163
22. Zhang, D. H. *Mater. Chem. Phys.* **1996,** *45,* 248–252. doi:10.1016/0254-0584(96)80115-5
23. Latu-Romain, E.; Gilet, P.; Chevalier, N.; Mariolle, D.; Bertin, F.; Feuillet, G.; Perillat-Merceroz, G.; Ferret, P.; Levy, F.; Muret, P.; Chelnokov, A. *J. Appl. Phys.* **2010,** *107,* 124307. doi:10.1063/1.3436596
24. Chen, C.-Y.; Chen, M.-W.; Ke, J.-J.; Lin, C.-A.; Retamal, J. R. D.; He, J.-H. *Pure Appl. Chem.* **2010,** *82,* 2055–2073. doi:10.1351/PAC-CON-09-12-05
25. Liu, P.; She, G.; Liao, Z.; Wang, Y.; Wang, Z.; Shi, W.; Zhang, X.; Lee, S.-T.; Chen, D. *Appl. Phys. Lett.* **2009,** *94,* 063120. doi:10.1063/1.3082173
26. Olbrich, A.; Ebersberger, B.; Boit, C. *Appl. Phys. Lett.* **1998,** *73,* 3114. doi:10.1063/1.122690
27. Kočka, J.; Stuchlíková, H.; Stuchlík, J.; Rezek, B.; Švrček, V.; Fojtík, P.; Pelant, I.; Fejfar, A. Microcrystalline Silicon: Relation between Transport and Microstructure. In *Polycrystalline Semiconductors VI;* Bonnaud, O.; Mohammed-Brahim, T.; Strunk, H. P.; Werner, J. H., Eds.; Solid State Phenomena; Trans Tech Publications Inc.: Durnten-Zurich, Switzerland, 2001; p 213.
28. Teichert, C.; Beinik, I. Conductive Atomic-Force Microscopy Investigation of Nanostructures in Microelectronics. In *Scanning Probe Microscopy in Nanoscience and Nanotechnology 2;* Bhushan, B., Ed.; Springer: Berlin Heidelberg, 2011; pp 691–721.
29. Yang, T.; Hertenberger, S.; Morkötter, S.; Abstreiter, G.; Koblmüller, G. *Appl. Phys. Lett.* **2012,** *101,* 233102. doi:10.1063/1.4768001
30. Brauer, G.; Anwand, W.; Grambole, D.; Egger, W.; Sperr, P.; Beinik, I.; Wang, L.; Teichert, C.; Kuriplach, J.; Lang, J.; Zviagin, S.; Cizmar, E.; Ling, C. C.; Hsu, Y. F.; Xi, Y. Y.; Chen, X.; Djurišić, A. B.; Skorupa, W. *Phys. Status Solidi C* **2009,** *6,* 2556–2560. doi:10.1002/pssc.200982081
31. Beinik, I.; Kratzer, M.; Wachauer, A.; Wang, L.; Lechner, R. T.; Teichert, C.; Motz, C.; Anwand, W.; Brauer, G.; Chen, X. Y.; Hsu, Y. F.; Djurišić, A. B. *J. Appl. Phys.* **2011,** *110,* 052005. doi:10.1063/1.3623764
32. Sakaguchi, H.; Iwata, F.; Hirai, A.; Sasaki, A.; Nagamura, T. *Jpn. J. Appl. Phys., Part 1* **1999,** *38,* 3908–3911. doi:10.1143/JJAP.38.3908
33. Coffey, D. C.; Reid, O. G.; Rodovsky, D. B.; Bartholomew, G. P.; Ginger, D. S. *Nano Lett.* **2007,** *7,* 738–744. doi:10.1021/nl062989e
34. Pingree, L. S. C.; Reid, O. G.; Ginger, D. S. *Nano Lett.* **2009,** *9,* 2946–2952. doi:10.1021/nl901358v
35. Dang, X.-D.; Tamayo, A. B.; Seo, J.; Hoven, C. V.; Walker, B.; Nguyen, T.-Q. *Adv. Funct. Mater.* **2010,** *20,* 3314–3321. doi:10.1002/adfm.201000799
36. Heng, L.; Tian, D.; Chen, L.; Su, J.; Zhai, J.; Han, D.; Jiang, L. *Chem. Commun.* **2010,** *46,* 1162–1164. doi:10.1039/b916026d
37. Smoliner, J.; Brezna, W. *Rev. Sci. Instrum.* **2007,** *78,* 106104. doi:10.1063/1.2794062
38. Brezna, W.; Fasching, G.; Unterrainer, K.; Strasser, G.; Smoliner, J. *Phys. Status Solidi C* **2009,** *6,* 793–796. doi:10.1002/pssc.200880611
39. Ledinský, M.; Fejfar, A.; Vetushka, A.; Stuchlík, J.; Rezek, B.; Kočka, J. *Phys. Status Solidi RRL* **2011,** *5,* 373–375. doi:10.1002/pssr.201105413
40. Kratzer, M.; Rubezhanska, M.; Prehal, C.; Beinik, I.; Kondratenko, S. V.; Kozyrev, Yu. N.; Teichert, C. *Phys. Rev. B* **2012,** *86,* 245320. doi:10.1103/PhysRevB.86.245320
41. Hsu, Y. F.; Xi, Y. Y.; Djurišić, A. B.; Chan, W. K. *Appl. Phys. Lett.* **2008,** *92,* 133507. doi:10.1063/1.2906370
42. Lany, S.; Zunger, A. *Phys. Rev. B* **2005,** *72,* 035215. doi:10.1103/PhysRevB.72.035215
43. Brauer, G.; Anwand, W.; Grambole, D.; Skorupa, W.; Hou, Y.; Andreev, A.; Teichert, C.; Tam, K. H.; Djurišić, A. B. *Nanotechnology* **2007,** *18,* 195301. doi:10.1088/0957-4484/18/19/195301
44. Lorbek, S.; Hlawacek, G.; Teichert, C. *Eur. Phys. J.: Appl. Phys.* **2011,** *55,* 23902. doi:10.1051/epjap/2011100428
45. http://www.nanosensors.com/ATEC-CONT.htm (accessed Nov 6, 2012).
46. Bao, J.; Shalish, I.; Su, Z.; Gurwitz, R.; Capasso, F.; Wang, X.; Ren, Z. *Nanoscale Res. Lett.* **2011,** *6,* 404. doi:10.1186/1556-276X-6-404
47. Anwand, W.; Brauer, G.; Grynszpan, R. I.; Cowan, T. E.; Schulz, D.; Klimm, D.; Čižek, J.; Kuriplach, J.; Procházka, I.; Ling, C. C.; Djurišić, A. B.; Klemm, V.; Schreiber, G.; Rafaja, D. *J. Appl. Phys.* **2011,** *109,* 063516. doi:10.1063/1.3559264
48. Sarid, D. *Exploring scanning probe microscopy with mathematica;* Wiley-VCH: Weinheim, 2007.
49. Beinik, I.; Galiana, B.; Kratzer, M.; Teichert, C.; Rey-Stolle, I.; Algora, C.; Tejedor, P. *J. Vac. Sci. Technol., B* **2010,** *28,* C5G5. doi:10.1116/1.3454373
50. Agrawal, R.; Peng, B.; Espinosa, H. D. *Nano Lett.* **2009,** *9,* 4177–4183. doi:10.1021/nl9023885
51. Özgür, U.; Alivov, Y. I.; Liu, C.; Teke, A.; Reshchikov, M. A.; Doğan, S.; Avrutin, V.; Cho, S.-J.; Morkoc, H. *J. Appl. Phys.* **2005,** *98,* 041301. doi:10.1063/1.1992666
52. Farraro, R.; Mclellan, R. B. *Metall. Trans. A* **1977,** *8,* 1563–1565. doi:10.1007/BF02644859
53. Merker, J.; Lupton, D.; Topfer, M.; Knake, H. *Platinum Met. Rev.* **2001,** *45,* 74–82.
54. Polifke, W.; Kopitz, J. *Wärmeübertragung: Grundlagen, analytische und numerische Methoden,* 2nd ed.; Addison-Wesley Verlag, 2009.
55. Zhu, B. L.; Zhao, X. Z.; Su, F. H.; Li, G. H.; Wu, X. G.; Wu, J.; Wu, R. *Vacuum* **2010,** *84,* 1280–1286. doi:10.1016/j.vacuum.2010.01.059
56. Golshahi, S.; Rozati, S. M.; Ghasempoor, T. *Dig. J. Nanomater. Biostruct.* **2011,** *6,* 445–450.

Beilstein Journal of Nanotechnology

Micro- and nanoscale electrical characterization of large-area graphene transferred to functional substrates

Gabriele Fisichella[1,2], Salvatore Di Franco[1], Patrick Fiorenza[1], Raffaella Lo Nigro[1], Fabrizio Roccaforte[1], Cristina Tudisco[3], Guido G. Condorelli[3], Nicolò Piluso[1], Noemi Spartà[4], Stella Lo Verso[4], Corrado Accardi[4], Cristina Tringali[4], Sebastiano Ravesi[4] and Filippo Giannazzo[*1]

Full Research Paper

Open Access

Address:
[1]CNR-IMM, VIII Strada, 5, 95121, Catania, Italy, [2]Department of Electronic Engineering, University of Catania, Viale A. Doria 6, 95125 Catania, Italy, [3]Department of Chemistry, University of Catania, Catania, Italy and [4]STMicroelectronics, Stradale Primosole, 50, 95121, Catania, Italy

Email:
Filippo Giannazzo[*] - filippo.giannazzo@imm.cnr.it

* Corresponding author

Keywords:
conductive AFM; contact resistance; graphene; mobility; PEN; sheet resistance; SiO_2

Beilstein J. Nanotechnol. **2013,** *4,* 234–242.
doi:10.3762/bjnano.4.24

Received: 17 November 2012
Accepted: 07 March 2013
Published: 02 April 2013

This article is part of the Thematic Series "High-resolution electrical and chemical characterization of nm-scale organic and inorganic devices".

Guest Editors: E. Meyer and P. Eyben

Abstract

Chemical vapour deposition (CVD) on catalytic metals is one of main approaches for high-quality graphene growth over large areas. However, a subsequent transfer step to an insulating substrate is required in order to use the graphene for electronic applications. This step can severely affect both the structural integrity and the electronic properties of the graphene membrane. In this paper, we investigated the morphological and electrical properties of CVD graphene transferred onto SiO_2 and on a polymeric substrate (poly(ethylene-2,6-naphthalene dicarboxylate), briefly PEN), suitable for microelectronics and flexible electronics applications, respectively. The electrical properties (sheet resistance, mobility, carrier density) of the transferred graphene as well as the specific contact resistance of metal contacts onto graphene were investigated by using properly designed test patterns. While a sheet resistance $R_{sh} \approx 1.7$ kΩ/sq and a specific contact resistance $\rho_c \approx 15$ kΩ·µm have been measured for graphene transferred onto SiO_2, about 2.3× higher R_{sh} and about 8× higher ρ_c values were obtained for graphene on PEN. High-resolution current mapping by torsion resonant conductive atomic force microscopy (TRCAFM) provided an insight into the nanoscale mechanisms responsible for the very high ρ_c in the case of graphene on PEN, showing a ca. 10× smaller "effective" area for current injection than in the case of graphene on SiO_2.

Introduction

Graphene is the single layer of graphite and can be described as a 2D crystal of sp^2 hybridised carbon atoms in a honeycomb lattice [1]. Its electrical and optical characteristics are mainly related to the peculiar energy band structure, i.e., to the linear dispersion relation and to the zero band gap. For neutral (undoped) graphene the Fermi level is coincident with the Dirac point, that is, the intersection point between the valence and the conduction band. From these properties originate the high intrinsic field-effect mobility [2-4] of graphene, its high thermal conductivity [5], and its optical transparency [6].

Due to its excellent mobility, graphene has been proposed as a channel material in high-frequency devices operating in the 100 GHz to terahertz range [7]. Thanks to the very high specific capacitance, it is an excellent candidate for fabricating highly efficient supercapacitors [8]. Furthermore, the unique combination between high optical transparency (≈97%) in a wide range of wavelengths (from near IR to near UV), high conductivity, and excellent flexibility, make it the ideal candidate as a transparent electrode for flat-panel displays, for OLEDs, and for the next generation of flexible organic solar cells [9,10].

Currently, the most used method of graphene production for basic studies is the mechanical exfoliation of graphite [1], which was the first method to obtain graphene under ambient laboratory conditions. This method yields graphene fragments of excellent crystalline quality, but of small size (1–100 μm) and which are randomly distributed on the substrate. Carrier mobilities $>10^5$ $cm^2 \cdot V^{-1} \cdot s^{-1}$ have been measured on exfoliated graphene flakes suspended between electrodes [4], whereas values from 10,000 to 30,000 $cm^2 \cdot V^{-1} \cdot s^{-1}$ are obtained for flakes on common dielectric substrates [11]. As a matter of fact, future applications in large-scale electronics will require wafer-scale sheets of graphene that can be deterministically placed on a substrate.

Other methods, such as epitaxial graphene growth by controlled graphitization of silicon carbide [12-15] and by chemical vapour deposition (CVD) on catalytic metals [9], are more suitable for large-area applications, as has been demonstrated in the past few years.

Considering the case of CVD, the two main catalytic metals used for graphene growth are nickel and copper [16]. In the case of CVD growth on copper foils, due to the extremely low solubility of carbon in the solid metal, the graphene formation is purely a surface process and this allows one to obtain single-layer graphene on a very large fraction (above 90%) of the metal surface [17]. In order to use CVD-grown graphene for electronic applications, the graphene membrane must be transferred to a properly chosen insulating substrate [18].

A commonly used method to transfer graphene grown on copper foil onto the target substrate is the use of a resist film deposited on the graphene surface, which is used as a support during the etching of the underlying Cu foil. After the etching process, the graphene membrane attached to the resist scaffold is mechanically attached to the target substrate and the resist is eliminated. There are two crucial points in this transfer technique: (i) promoting the adhesion of graphene onto the target substrate; and (ii) cleaning the transferred graphene from resist residues.

The first issue is especially critical, because a bad compatibility between graphene and the substrate typically causes the formation of macroscopic defects (cracks) or folding of the graphene membrane when placed onto the substrate. Several aspects can influence the surface adhesion between graphene and the substrate, including the substrate roughness and the surface energy. Though a complete understanding of this issue has not yet been achieved, it can be argued that, due to the inherent hydrophobic character of graphene, the adhesion of large-area membranes can be favoured on substrates with a similar hydrophobic character.

Resist and, more generally, polymeric residues adsorbed onto graphene are known to severely degrade graphene transport properties [19]. However, a complete cleaning of the transferred graphene from those residues is particularly difficult, because it requires thermal treatments at temperatures of up to 400 °C in vacuum [19] or under reducing (N_2/H_2 or Ar/H_2) ambient conditions [20]. Such high thermal budgets are not compatible with some substrates of interest for future graphene electronics, such as the flexible polymeric ones.

In this paper, the transfer and electrical properties of CVD-grown graphene on different substrates have been addressed. In particular, two substrates of interest for electronic applications were taken into consideration:

1. SiO_2 (300 nm thick) thermally grown on Si, for its large-scale use in microelectronics;
2. poly(ethylene-2,6-naphthalene dicarboxylate) or PEN, a transparent polymer analogue to the more common PET, but with stronger mechanical resistance, higher degradation temperature and higher chemical inertness in acid and alkaline conditions, which can be useful for transparent and flexible electronic applications.

The electronic properties of the transferred graphene have been characterized both at the macro- and nanoscale, by using properly fabricated test patterns and conductive atomic force microscopy, respectively. This characterization provided an insight into the different electronic properties of graphene transferred to the two kinds of substrates.

Graphene growth and transfer

Graphene was grown by CVD on ca. 25 μm thick polycrystalline copper foils at a temperature of 1000 °C by using CH_4/H_2 as precursors. In Figure 1a an optical microscopy image of the Cu surface after graphene growth is reported, showing the typical size of Cu grains, ranging from about 20 to 200 μm. The graphene membrane, uniformly covering the Cu foil, is mostly composed of a single layer of graphene (over 90% of the surface area), while bilayers or multilayers can be typically found at Cu grain boundaries. A representative Raman spectrum on the Cu surface is reported in Figure 1b, showing the characteristic G peak (at ≈1580 cm^{-1}) and 2D peak (at ≈2640 cm^{-1}) of the graphitic material. In particular, the high ratio of the 2D versus G peak and the symmetric character of the 2D peak (fitted by a single Lorentzian component with FWHM ≈ 38 cm^{-1}, as shown in the insert of Figure 1b) are consistent with the presence of a single layer of graphene. The D peak (at ≈1320 cm^{-1}) indicates the presence of a certain density of defects in the as-grown material. Morphology and phase images of as-grown graphene on Cu, obtained by tapping mode atomic force microscopy (AFM), are also reported in Figure 1c and Figure 1d. In particular, from the phase image it is possible to see the presence of peculiar corrugations (wrinkles) in the graphene membrane over the copper foil. The origin of these corrugations will be discussed in the following.

Graphene transfer onto silicon dioxide

The graphene membrane was transferred from the Cu foil onto a Si wafer coated by 300 nm thick thermally grown SiO_2. This oxide thickness was properly selected because it ensures the best optical contrast between bare SiO_2 regions and regions coated by the monoatomic thick membrane, due to an effect of constructive optical interference [21].

Since as-grown SiO_2 typically exhibits a hydrophilic behaviour (as shown by contact-angle measurements, yielding values of 10 ± 2°), before graphene transfer proper surface treatments were performed to achieve a partially hydrophobic character (with contact-angle values of 52 ± 2°). The chemical status of the SiO_2 surface before graphene transfer was also characterized by X-ray photoelectron spectroscopy (XPS) measurements.

In Figure 2a the optical image of a large-area (cm^2) graphene membrane transferred onto SiO_2 is shown. Due to the good optical contrast between the graphene-coated and bare SiO_2 areas, a homogenous graphene membrane, free from macroscopic cracks, can be observed. Higher resolution morphological analyses of the graphene layer onto SiO_2 were carried out by tapping mode AFM. Two representative AFM images at different magnifications are reported in Figure 2b and Figure 2c. As evident from Figure 2b, a high density of submi-

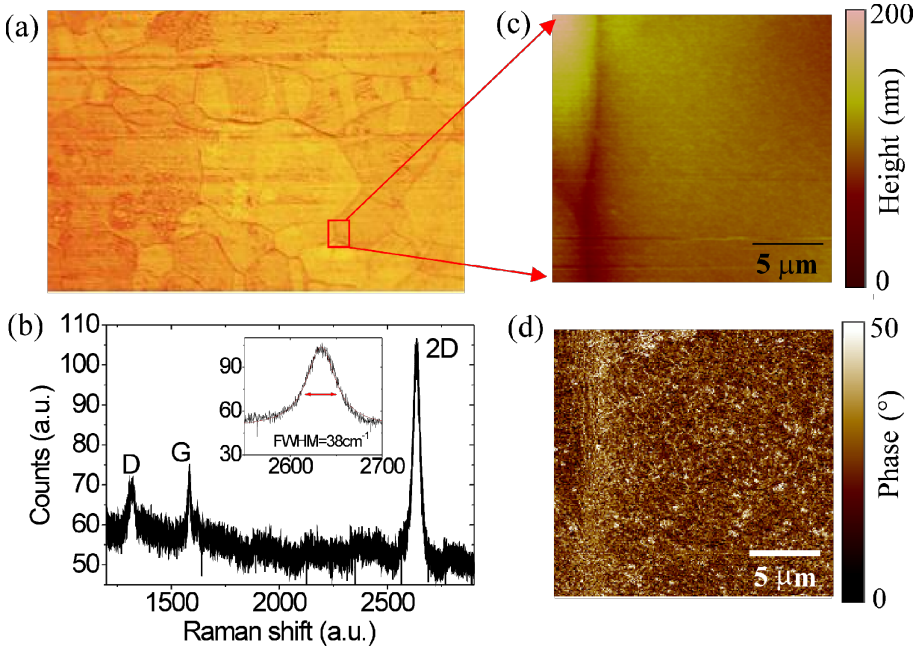

Figure 1: As-grown graphene on a copper foil: (a) Optical image, (b) Raman Spectroscopy, (c) AFM morphology and (d) phase.

crometric features can be observed on the graphene, mainly represented by contaminations (polymer residues) left after removal of the thick resist film employed for the transfer process. Furthermore, some typical defects of the graphene membrane, such as small cracks or peculiar corrugations (wrinkles), are indicated in Figure 2b. While the first kind of defect is mostly related to the mechanical handling of graphene during transfer, wrinkles can be present also in the as-grown graphene on Cu (as already shown in Figure 1d). Corrugations in as-grown graphene originate from the cooling-down step of the CVD process, due to the different thermal expansion coefficients between graphene and Cu. However, some of the wrinkles can also be produced during the transfer process to the substrate. In Figure 2d the height profile of a wrinkle is displayed, whereas in Figure 2e the step height between graphene and bare SiO_2 on a crack region extracted from Figure 2c is shown. The measured step height (≈0.8 nm) is consistent with the typical values reported by AFM for a single layer of graphene on SiO_2 [22]. Both cracks and corrugations contribute to the degradation of the electronic transport properties in graphene [23].

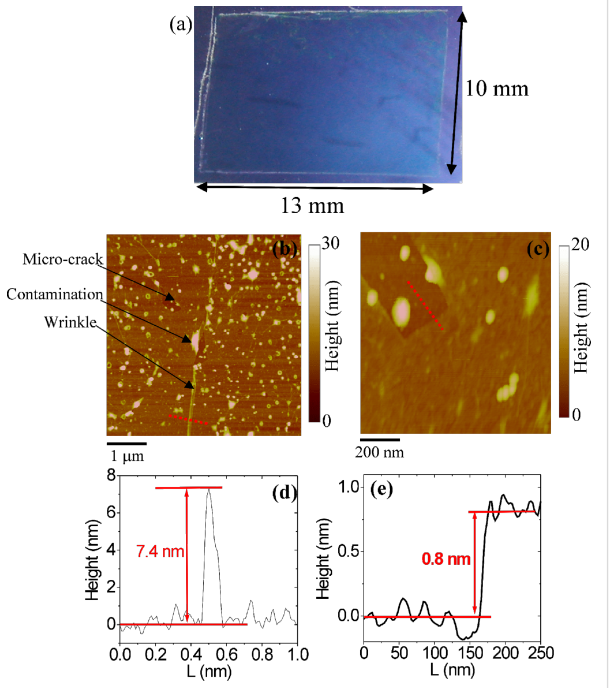

Figure 2: Optical image of a (13 × 10) mm^2 graphene membrane transferred onto SiO_2 (a), and AFM morphologies at (5 × 5) μm^2 (b) and (1 × 1) μm^2 (c) magnifications. Line scans on a peculiar corrugation of the graphene membrane (d) and across a microscopic crack (e).

Graphene transfer onto PEN

In contrast to the case of virgin SiO_2, which is naturally hydrophilic and requires proper treatments to be converted into a hydrophobic surface, contact-angle measurements on the as-received PEN substrate typically yield high values of the contact angle (≈80°), indicating the highly hydrophobic character of this surface. A representative morphological image of the PEN substrate is reported in Figure 3a, showing a high surface roughness (RMS ≈ 6.3 nm). When transferred onto PEN, graphene conformally covers the substrate morphology. By carefully comparing Figure 3b on graphene-coated PEN with Figure 3a on bare PEN, the presence of a pleated and wrinkled membrane superimposed on the rough substrate can be deduced. The higher roughness value in graphene-coated PEN can also be partially ascribed to the presence of resist residues from the transfer process.

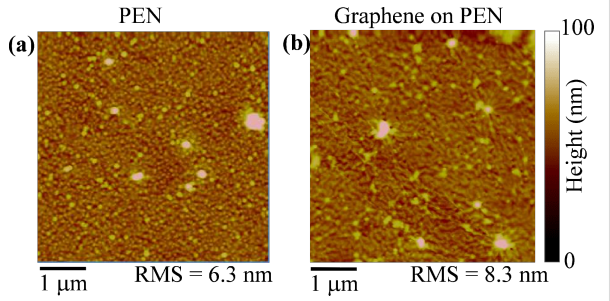

Figure 3: Tapping-mode AFM images of the bare PEN surface (a) and of graphene transferred onto PEN (b).

The homogeneity of graphene membranes on the transparent PEN substrate can be characterized in a straightforward way by optical transmittance microscopy, since a contrast between graphene-coated and uncoated regions arises from the finite absorbance (≈2.7%) of the graphene monolayer. Optical images (not reported) demonstrate the absence of macroscopic cracks and fractures in the graphene transferred onto PEN, which can be explained as a consequence of a very good compatibility between the two materials.

Results and Discussion

Microscale electrical characterization

The electronic transport properties of the large-area graphene transferred onto the two different substrates have been characterized on the macroscopic scale by electrical measurements on transmission line model (TLM) test structures. An optical microscopy image of a TLM test pattern fabricated in graphene on SiO_2 is reported in Figure 4a. It consists of a set of metal contacts (Ni/Au) with identical geometry (width W = 200 μm and length L = 100 μm) and different spacing, d, deposited onto a laterally insulated rectangular graphene area. The current–voltage (I–V) characteristics for different distances between adjacent contacts are reported in Figure 4b, showing an Ohmic behaviour for all the contact distances. In Figure 4c the

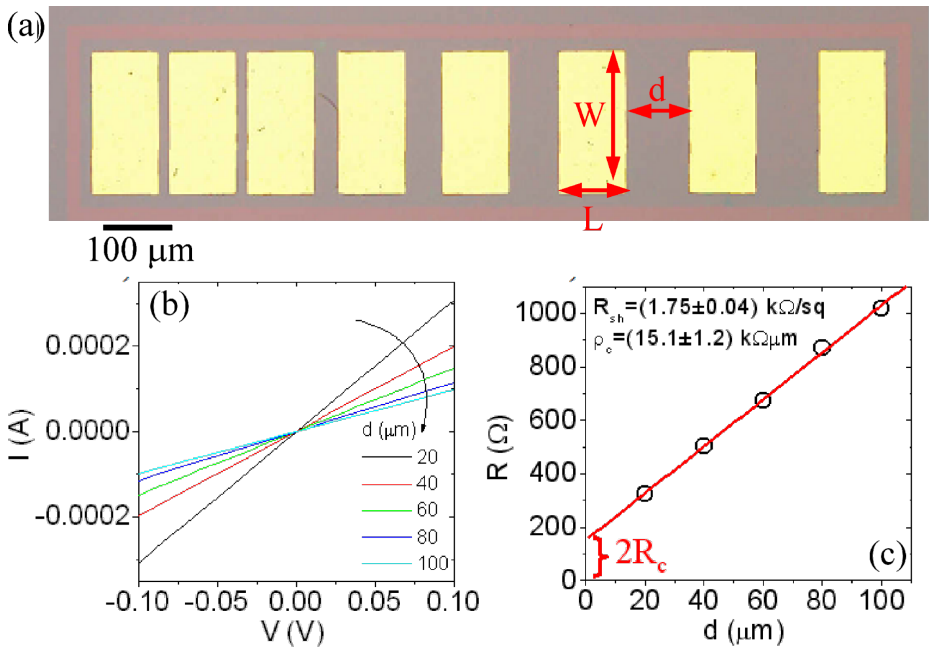

Figure 4: (a) Optical Image of a TLM structure, (b) *I–V* characteristics measured between pairs of contacts at different distances and (c) extracted resistance plotted versus distance. From the linear fit of *R* versus *d*, the sheet resistance and the specific contact resistance were evaluated.

resistance R, obtained from the slope of each curve, is plotted versus the contact distance. According to the TLM theory [24], R is related to the metal/graphene contact resistance R_c and to the graphene sheet resistance R_{sh} according to the relation

$$R = 2R_c + \frac{R_{sh}}{W} d \,. \tag{1}$$

By linear fitting of the data in Figure 4c by Equation 1, the sheet resistance (R_{sh} = 1.75 ± 0.04 kΩ/sq) and the contact resistance (R_c = 75 ± 6 Ω) contributions have been determined. Since R_c clearly depends on the pad size, the specific contact resistance $\rho_c = R_c \cdot W$ normalized to the contact width was also evaluated, obtaining a value ρ_c = 15.1 ± 1.2 kΩ·µm.

For graphene transferred onto the SiO_2(300nm)/Si substrate, the n^+-doped Si substrate can be employed as global back-gate (see schematic in Figure 5a) to induce an electrostatic shift of the Fermi level of graphene and, hence, to tune the carrier density of the material. In Figure 5b the resistance versus the distance between adjacent contacts is reported for different values of the back-gate bias V_g from −40 to 40 V. By linear fitting of each curve, the dependence of the specific contact resistance (ρ_c) and of the sheet resistance (R_{sh}) on the gate bias was extracted (see Figure 5c and Figure 5d, respectively). It is worth noting that both R_{sh} and ρ_c exhibit a monotonically increasing behaviour with the back-gate bias values in the considered bias range.

Compared to the typically ambipolar behaviour observed in back-gated FET devices fabricated in graphene exfoliated from HOPG onto SiO_2 (which exhibit hole conduction for negative gate bias and electron conduction for positive bias) [10,11], a p-type doping can be deduced from the electrical characterization of CVD-grown graphene membranes transferred onto SiO_2. This doping can probably be ascribed to the adsorbed resist impurities left after transfer. Furthermore, the measured ρ_c is almost one order of magnitude higher than in the case of the same nickel–gold contacts on graphene exfoliated onto SiO_2 [25].

The hole conductance $\sigma = 1 / R_{sh}$ in graphene is related to the hole mobility μ_p and density p by the following relation

$$\sigma = q\mu_p p = q\mu_p \left(\frac{C_{ox} V_g}{q} + p_0 \right) \tag{2}$$

where p has been expressed as the sum of p_0, i.e., the doping at V_g = 0, and of the doping induced by the back-gate bias ($C_{ox} \cdot V_g / q$), with q being the electron charge and $C_{ox} = \varepsilon_0 \varepsilon_{ox} / t_{ox}$ the oxide capacitance per unit area.

By linear fitting of the experimental σ versus V_g data with Equation 2 (see insert of Figure 5d), the values of μ_p = 793 ± 18 $cm^2 \cdot V^{-1} \cdot s^{-1}$ and $p_0 = (4.4 \pm 0.1) \times 10^{12}$ cm^{-2} have

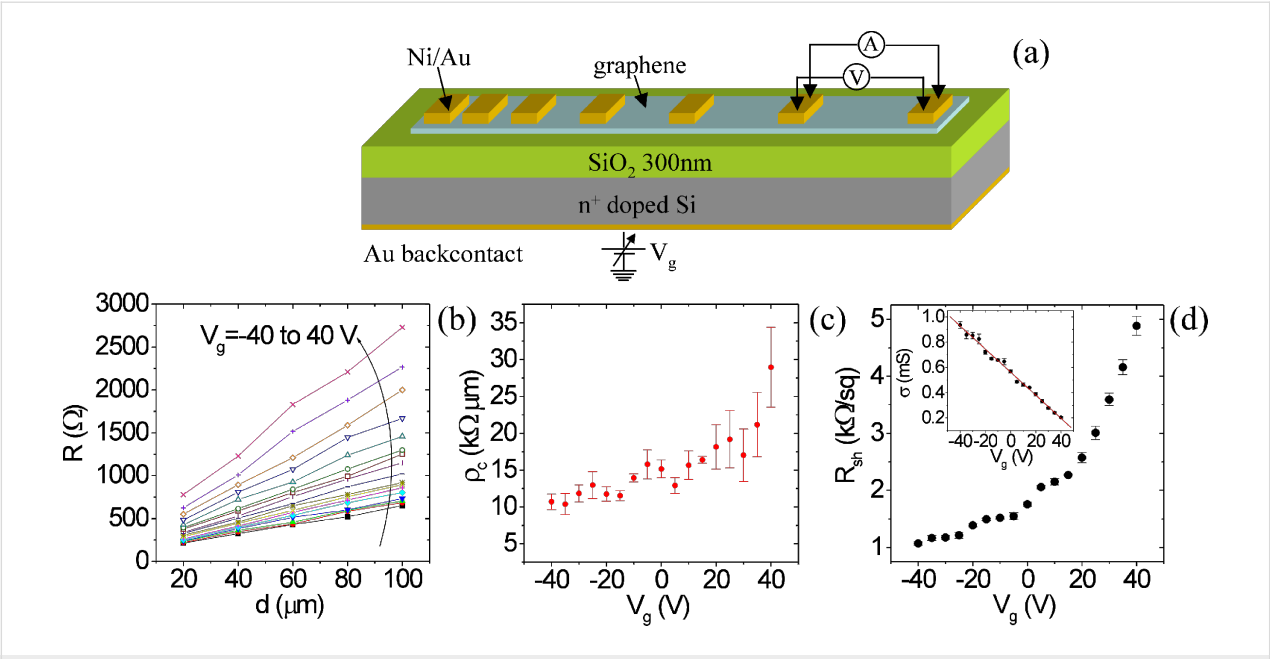

Figure 5: (a) Schematic representation of the back-gated TLM device. (b) Resistance versus distance between adjacent contacts for different V_g values from −40 to 40 V. Extracted specific contact resistance ρ_c (c) and sheet resistance R_{sh} (d) versus V_g. The insert in (d) displays the linear fit of the conductance data to extract the hole density and mobility in graphene.

been obtained. It is worth noting that the effect of traps at the graphene/SiO_2 interface is not accounted for in the determination of μ_p from Equation 2. This approximation implies an overestimation of the hole density p, which is actually reduced with respect to the value induced by the field effect due to carrier trapping, and, consequently, an underestimation of the carrier mobility. Furthermore, the presence of charged traps at the graphene/substrate interface strongly affects the mobility in graphene due to Coulomb scattering [11,26], leading to a degradation with respect to the ideal value in the absence of interface traps.

A similar macroscopic electrical characterization using TLM structures was performed also in CVD graphene transferred onto PEN. In this case, the sheet resistance and specific contact resistance only were measured, whereas an estimate of mobility and carrier density was not feasible due to the absence of a back gate. A comparison between the R_{sh} and ρ_c values for graphene on the two substrates (obtained with a back-gate bias $V_g = 0$ for graphene on SiO_2 and without a back-gate bias for graphene on PEN) is reported in Table 1.

It is worth noting that the R_{sh} of graphene on PEN is about 2.3× higher than on SiO_2, whereas the ρ_c is about 8× higher. Since the same CVD graphene was used for both samples and similar transfer quality has been achieved on both substrates, these electrical differences can be ascribed to the different kind of interaction between graphene and SiO_2 and graphene and PEN.

Table 1: Comparison between the sheet resistance and the metal/graphene specific contact resistance of graphene deposited on SiO_2 and on PEN.

	SiO_2	PEN
R_{sh} (kΩ/sq)	1.7 ± 0.1	3.9 ± 0.1
ρ_c (kΩ·μm)	15.1 ± 1.2	114.4 ± 2.3

In fact, a van der Waals interaction occurs between graphene and SiO_2, whereas it cannot be excluded that other kind of bonds occur locally between graphene and the polymeric substrate, leading to a partial sp^3 hybridization of graphene C atoms and, hence, to a local disruption of graphene electronic properties. This idea is supported by the presence of a certain density of defects in the initial graphene (as shown by Raman measurements), that can represent preferential sites for bonding with the polymeric chains.

Nanoscale electrical characterization

In order to get a deeper insight into the mechanisms leading to the different electronic properties of transferred graphene on the two substrates, and, in particular, to the very different specific contact resistance values, the local electrical properties of graphene on SiO_2 and on PEN were characterized by torsion resonance conductive AFM (TRCAFM).

TRCAFM is an evolution of the more widely used contact mode conductive atomic force microscopy (CAFM). It is a dynamic

scanning probe method based on a conductive tip scanned at close proximity (0.3–3.0 nm) to the sample surface, while oscillating in the torsional mode. The torsion amplitude is used as the feedback signal to measure surface morphology.

A dc bias was applied to a macroscopic metal contact deposited onto graphene, and the current locally injected from the nanometric conductive tip into graphene was probed by a high sensitivity (fA) current sensor connected to the tip. In this way, TRCAFM combines the high resolution of dynamic scanning probe microscopy for morphological mapping with the ability for nanoscale-resolution current mapping of CAFM. This operation mode has been demonstrated to be particularly useful to perform high-resolution morphology and current maps in graphene [27,28].

Figure 6a and Figure 6b show the surface morphology and current map for graphene on SiO_2. In Figure 6c and Figure 6d the histograms of the height and of the current values extracted from the two maps are reported, respectively. Similarly, Figure 6e and Figure 6f show the morphology and current maps in graphene on PEN, while Figure 6g and Figure 6h show the derived histograms of height and current values. As evident from this comparison, the morphology of graphene on SiO_2 is much flatter than the morphology of graphene on PEN, due to the very different roughness of the substrates. The most interesting aspect is represented by the comparison of the current maps and of the current histograms. Clearly, both histograms exhibit two peaks, but it is worth noting that the integrated percentage of counts under the higher conductivity peak is much higher for graphene on SiO_2 (85%) than for graphene on PEN (9%). This striking difference indicates that in the case of graphene on SiO_2 most of the area contributes to current injection from the tip to graphene, whereas in the case of graphene on PEN only a small fraction of the area contributes to the current injection. This observation is in close agreement with the difference in the specific contact resistance values obtained from macroscopic TLM measurements. The physical origin of this difference is still the subject of investigation.

Conclusion

In conclusion, the transfer of CVD-grown graphene onto different substrates (SiO_2 and PEN) and its morphological and electrical properties have been investigated in detail. Using TLM test patterns the electrical properties (sheet resistance, mobility, carrier density) of the transferred graphene and the specific contact resistance of metal contacts on graphene were determined. While a sheet resistance $R_{sh} \approx 1.7$ kΩ/sq and a specific contact resistance $\rho_c \approx 15$ kΩ·μm were measured (at $V_g = 0$ V) for graphene transferred onto SiO_2, about 2.3× higher R_{sh} and about 8× higher ρ_c values were obtained for graphene on PEN. High-resolution current mapping by torsion resonant conductive atomic force microscopy (TRCAFM) revealed a ca. 10× smaller "effective" area for current injection in the case of graphene on PEN than in the case of CVD graphene transferred on SiO_2 ,which is consistent with higher ρ_c values. These electrical differences could be ascribed also to the different kind of interaction of graphene with SiO_2 and PEN. While a van der Waals bond occurs between graphene and SiO_2, other kind of bonds can be locally formed between graphene and the polymeric chains of PEN, leading to a partial sp^3 hybridization of graphene and, hence, to a local modification of its electronic properties.

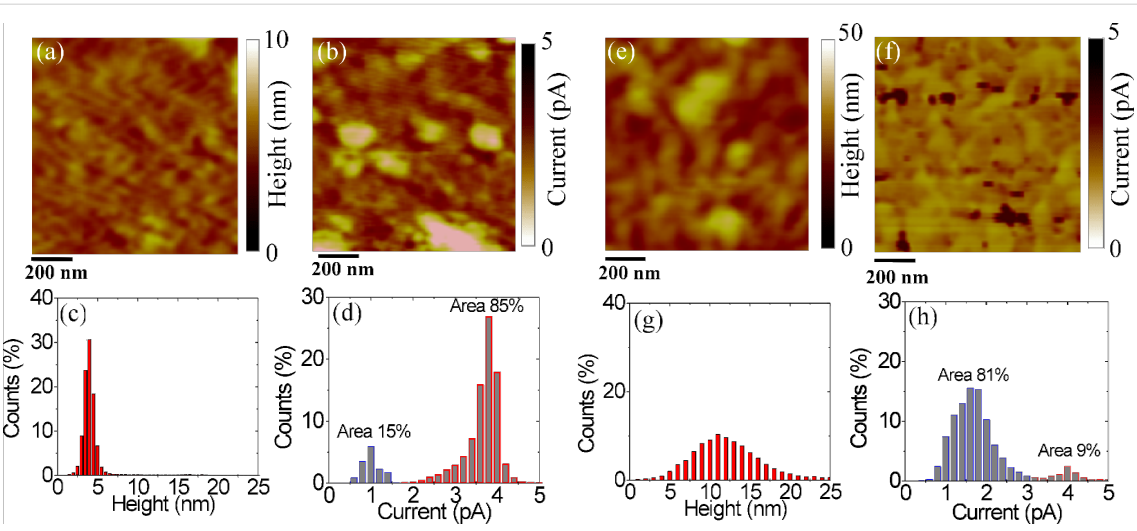

Figure 6: TRCAFM of Graphene on SiO_2: (a) morphology and (c) the related histogram, (b) current map and (d) the related histogram. TRCAFM of Graphene on PEN: (a) morphology and (c) the related histogram, (b) current map and (d) the related histogram.

Experimental

Tapping mode AFM and TRCAFM: Both tapping-mode AFM and torsion resonant conductive atomic force microscopy (TRCAFM) measurements were performed by using a DI3100 microscope with Nanoscope V electronics. For TRCAFM, we used Pt/Ir-coated Si tips with an apex radius of curvature of 10 nm, which were driven in torsional motion at a frequency of 940 kHz.

TLM fabrication and electrical characterization: The transmission line model (TLM) test patterns were fabricated on the transferred graphene membranes by using the following procedure. First, rectangular graphene areas were isolated from the external membrane by lithographically defining and opening a rectangular frame in a hard mask resist and by performing graphene etching of the frame by O_2 plasma treatments. Subsequently, a set of nickel-gold rectangular contacts were deposited by sputtering and defined by the lift-off method. The contacts had identical geometry (200 μm width and 100 μm length) and the distance between the pairs of adjacent contacts were 20, 20, 40, 60, 80, 100 and 100 μm, respectively. The current–voltage (*I*–*V*) characteristics were measured in a Karl-Süss probe station by using a HP 4156B parameter analyzer.

Raman spectroscopy: Raman measurements were performed by using a Horiba-Jobin Yvon spectrometer. Spectra were collected in the backscattering configuration with a ≈633 nm laser source and a 100× objective, focusing the excitation light to a ≈1 μm spot.

XPS: SiO_2 atomic surface composition was determined by X-ray photoelectron analysis (XPS) by using a PHI ESCA/SAM 5600 Multitechnique spectrometer. XPS experiments were carried out with a base pressure of 2×10^{-10} torr. A monochromated Al Kα radiation source (hν = 1486.6 eV) was used, and XPS spectra were collected at various photoelectron angles (relative to the sample surface) in the 20–45° range.

Acknowledgements

The authors want to thank S. Rizzolo and M. Cannas from the Department of Physics of University of Palermo for participation in the sample characterization and for useful discussions, respectively. This work was supported, in part, by the GraphicRF project funded by ESF.

References

1. Novoselov, K. S.; Geim, A. K.; Morozov, S. V.; Jiang, D.; Zhang, Y.; Dubonos, S. V.; Grigorieva, I. V.; Firsov, A. A. *Science* **2004,** *306,* 666–669. doi:10.1126/science.1102896
2. Morozov, S. V.; Novoselov, K. S.; Katsnelson, M. I.; Schedin, F.; Elias, D. C.; Jaszczak, J. A.; Geim, A. K. *Phys. Rev. Lett.* **2008,** *100,* 016602. doi:10.1103/PhysRevLett.100.016602
3. Chen, J.-H.; Jang, C.; Xiao, S.; Ishigami, M.; Fuhrer, M. S. *Nat. Nanotechnol.* **2008,** *3,* 206–209. doi:10.1038/nnano.2008.58
4. Bolotin, K. I.; Sikes, K. J.; Jiang, Z.; Klima, M.; Fudenberg, G.; Hone, J.; Kim, P.; Stormer, H. L. *Solid State Commun.* **2008,** *146,* 351–355. doi:10.1016/j.ssc.2008.02.024
5. Balandin, A. A.; Ghosh, S.; Bao, W.; Calizo, I.; Teweldebrhan, D.; Miao, F.; Lau, C. N. *Nano Lett.* **2008,** *8,* 902–907. doi:10.1021/nl0731872
6. Nair, R. R.; Blake, P.; Grigorenko, A. N.; Novoselov, K. S.; Booth, T. J.; Stauber, T.; Peres, N. M. R.; Geim, A. K. *Science* **2008,** *320,* 1308. doi:10.1126/science.1156965
7. Lin, Y.-M.; Dimitrakopoulos, C.; Jenkins, K. A.; Farmer, D. B.; Chiu, H.-Y.; Grill, A.; Avouris, P. *Science* **2010,** *327,* 662. doi:10.1126/science.1184289
8. Stoller, M. D.; Park, S.; Zhu, Y.; An, J.; Ruoff, R. S. *Nano Lett.* **2008,** *8,* 3498–3502. doi:10.1021/nl802558y
9. Kim, K. S.; Zhao, Y.; Jang, H.; Lee, S. Y.; Kim, J. M.; Kim, K. S.; Ahn, J.-H.; Kim, P.; Choi, J.-Y.; Hong, B. H. *Nature* **2009,** *457,* 706–710. doi:10.1038/nature07719
10. Bonaccorso, F.; Sun, Z.; Hasan, T.; Ferrari, A. C. *Nat. Photonics* **2010,** *4,* 611–622. doi:10.1038/nphoton.2010.186
11. Giannazzo, F.; Sonde, S.; Lo Nigro, R.; Rimini, E.; Raineri, V. *Nano Lett.* **2011,** *11,* 4612–4618. doi:10.1021/nl2020922
12. Emtsev, K. V.; Bostwick, A.; Horn, K.; Jobst, J.; Kellogg, G. L.; Ley, L.; McChesney, J. L.; Ohta, T.; Reshanov, S. A.; Röhrl, J.; Rotenberg, E.; Schmid, A. K.; Waldmann, D.; Weber, H. B.; Seyller, T. *Nat. Mater.* **2009,** *8,* 203. doi:10.1038/nmat2382
13. Virojanadara, C.; Syväjarvi, M.; Yakimova, R.; Johansson, L. I.; Zakharov, A. A.; Balasubramanian, T. *Phys. Rev. B* **2008,** *78,* 245403. doi:10.1103/PhysRevB.78.245403
14. Vecchio, C.; Sonde, S.; Bongiorno, C.; Rambach, M.; Yakimova, R.; Raineri, V.; Giannazzo, F. *Nanoscale Res. Lett.* **2011,** *6,* 269. doi:10.1186/1556-276X-6-269
15. Giannazzo, F.; Raineri, V. *Riv. Nuovo Cimento Soc. Ital. Fis.* **2012,** *35,* 267–304. doi:10.1393/ncr/i2012-10076-7
16. Li, X.; Cai, W.; Colombo, L.; Ruoff, R. S. *Nano Lett.* **2009,** *9,* 4268–4272. doi:10.1021/nl902515k
17. Li, X.; Cai, W.; An, J.; Kim, S.; Nah, J.; Yang, D.; Piner, R.; Velamakanni, A.; Jung, I.; Tutuc, E.; Banerjee, S. K.; Colombo, L.; Ruoff, R. S. *Science* **2009,** *324,* 1312. doi:10.1126/science.1171245
18. Kang, J.; Shin, D.; Bae, S.; Hong, B. H. *Nanoscale* **2012,** *4,* 5527–5537. doi:10.1039/c2nr31317k
19. Pirkle, A.; Chan, J.; Venugopal, A.; Hinojos, D.; Magnuson, C. W.; McDonnell, S.; Colombo, L.; Vogel, E. M.; Ruoff, R. S.; Wallace, R. M. *Appl. Phys. Lett.* **2011,** *99,* 122108. doi:10.1063/1.3643444
20. Kedzierski, J. T.; Hsu, P.-L.; Reina, A.; Kong, J.; Healey, P. D.; Wyatt, P. W.; Keast, C. L. *IEEE Electron Device Lett.* **2009,** *30,* 745–747. doi:10.1109/LED.2009.2020615
21. Giannazzo, F.; Sonde, S.; Raineri, V.; Patanè, G.; Compagnini, G.; Aliotta, F.; Ponterio, R.; Rimini, E. *Phys. Status Solidi C* **2010,** *7,* 1251–1255. doi:10.1002/pssc.200982967
22. Giannazzo, F.; Sonde, S.; Raineri, V.; Rimini, E. *Nano Lett.* **2009,** *9,* 23. doi:10.1021/nl801823n
23. Zhu, W.; Low, T.; Perebeinos, V.; Bol, A. A.; Zhu, Y.; Yan, H.; Tersoff, J.; Avouris, P. *Nano Lett.* **2012,** *12,* 3431–3436. doi:10.1021/nl300563h

24. Schroder, D. K. *Semiconductor Material and Device Characterization,* 3rd ed.; John Wiley & Sons: Hoboken, NJ, 2006.
25. Venugopal, A.; Colombo, L.; Vogel, E. M. *Appl. Phys. Lett.* **2010,** *96,* 013512. doi:10.1063/1.3290248
26. Sonde, S.; Giannazzo, F.; Vecchio, C.; Yakimova, R.; Rimini, E.; Raineri, V. *Appl. Phys. Lett.* **2010,** *97,* 132101. doi:10.1063/1.3489942
27. Sonde, S.; Giannazzo, F.; Raineri, V.; Yakimova, R.; Huntzinger, J.-R.; Tiberj, A.; Camassel, J. *Phys. Rev. B* **2009,** *80,* 241406. doi:10.1103/PhysRevB.80.241406
28. Giannazzo, F.; Deretzis, I.; La Magna, A.; Roccaforte, F.; Yakimova, R. *Phys. Rev. B* **2012,** *86,* 235422. doi:10.1103/PhysRevB.86.235422

License and Terms

Beilstein Journal of Nanotechnology

A look underneath the SiO_2/4H-SiC interface after N_2O thermal treatments

Patrick Fiorenza*[1], Filippo Giannazzo[1], Lukas K. Swanson[1], Alessia Frazzetto[2,3], Simona Lorenti[3], Mario S. Alessandrino[3] and Fabrizio Roccaforte[1]

Full Research Paper

Open Access

Address:
[1]Consiglio Nazionale delle Ricerche - Istituto per la Microelettronica e Microsistemi (CNR-IMM) Strada VIII n. 5, Zona Industriale, 95121, Catania, Italy, [2]Scuola Superiore di Catania - Università degli Studi di Catania, Via Valdisavoia 9, 95123, Catania, Italy and [3]STMicroelectronics, Stadale Primosole 50, 95121, Catania, Italy

Email:
Patrick Fiorenza* - patrick.fiorenza@imm.cnr.it

* Corresponding author

Keywords:
4H-SiC; metal/oxide/semiconductor; nitrogen incorporation

Beilstein J. Nanotechnol. **2013,** *4,* 249–254.
doi:10.3762/bjnano.4.26

Received: 16 November 2012
Accepted: 26 March 2013
Published: 08 April 2013

This article is part of the Thematic Series "High-resolution electrical and chemical characterization of nm-scale organic and inorganic devices".

Guest Editors: E. Meyer and P. Eyben

Abstract

The electrical compensation effect of the nitrogen incorporation at the SiO_2/4H-SiC (p-type) interface after thermal treatments in ambient N_2O is investigated employing both scanning spreading resistance microscopy (SSRM) and scanning capacitance microscopy (SCM). SSRM measurements on p-type 4H-SiC areas selectively exposed to N_2O at 1150 °C showed an increased resistance compared to the unexposed ones; this indicates the incorporation of electrically active nitrogen-related donors, which compensate the p-type doping in the SiC surface region. Cross-sectional SCM measurements on SiO_2/4H-SiC metal/oxide/semiconductor (MOS) devices highlighted different active carrier concentration profiles in the first 10 nm underneath the insulator–substrate interface depending on the SiO_2/4H-SiC roughness.

The electrically active incorporated nitrogen produces both a compensation of the acceptors in the substrate and a reduction of the interface state density (D_{it}). This result can be correlated with the 4H-SiC surface configuration. In particular, lower D_{it} values were obtained for a SiO_2/SiC interface on faceted SiC than on planar SiC. These effects were explained in terms of the different surface configuration in faceted SiC that enables the simultaneous exposition at the interface of atomic planes with different orientations.

Introduction

The SiO_2/4H-SiC interface is the main building block of SiC-based MOSFET devices and its electrostructural quality typically has a direct impact on the device performance in power-electronics applications. In particular, electrically active defects at the SiO_2/SiC interfaces, such as carbon clusters, silicon suboxide bonds, or intrinsic defects in the near-interfacial oxide

layers have been indicated as the origin of the commonly observed low-channel mobility in SiC MOSFETs [1,2]. To alleviate the mobility problem, different postoxidation annealings (POA) of the gate oxide in NO or N_2O have been explored [3], which can be efficient to provide adequate mobility values in the range of 30–50 $cm^2 \cdot V^{-1} \cdot s^{-1}$ [4,5], but still significantly lower than the theoretical limits.

While it is commonly accepted that POA treatments in ambient NO or N_2O have a beneficial effect on the SiO_2 insulator and on the SiO_2/4H-SiC interface due to the passivation of oxide defects and interface traps by the incorporated nitrogen, the impact of these thermal treatments on the electrical properties of the 4H-SiC substrate is still under debate. Recently, Kosugi et al. [6] performed X-ray photoelectron spectroscopy (XPS) measurements on 4H-SiC directly exposed to ambient NO at 1200 °C, demonstrating that a significant density of nitrogen atoms (10^{14} cm^{-3}) is incorporated in the 4H-SiC near surface region and remains even after removing the thin (ca. 5 Å) SiO_2 layer formed on SiC during the annealing by sustained etching in hydrofluoric acid. The same group [7] demonstrated by the electrically detected magnetic resonance technique that shallow donor levels can be associated with a fraction of the incorporated N atoms. However, information on the electrical activation of the incorporated nitrogen and on the depth extension of the nitrogen profile is still lacking. Moreover, the role of the 4H-SiC surface morphology and in particular of the crystallographic planes exposed at the SiO_2/4H-SiC interface on the nitrogen incorporation have to be clarified.

In this paper, we applied scanning spreading resistance microscopy (SSRM) and scanning capacitance microscopy (SCM) to get a deeper insight into the electrical activation of nitrogen incorporated into 4H-SiC during thermal treatments in N_2O at 1150 °C. These two scanning probe methods have been applied in the past to study the electrical activation of ion doped and annealed SiC [8-11]. Due to the different measuring principles, i.e., differential capacitance measurements for SCM and current measurements for SSRM, the two techniques exhibit complementary performances especially in terms of dynamic range, with SSRM more suitable for higher concentrations and SCM more sensitive to lower concentrations, respectively. These complementary characters have been fully exploited in the present study. SSRM measurements were performed on p^+-doped ($\approx 10^{19}$ cm^{-3}) 4H-SiC areas selectively exposed to ambient N_2O (without the presence of the gate oxide to maximize the effect of nitrogen incorporation), revealing a significant increase of the SiC resistivity with respect to unexposed areas, i.e., a compensation effect from the N-related donors. SCM measurements were performed also on p-doped ($\approx 10^{17}$ cm^{-3}) 4H-SiC exposed to ambient N_2O through a 30 nm thick gate oxide, to simulate the real metal/oxide/semiconductor stack used in the MOSFET device. To evaluate the impact of 4H-SiC surface morphology on the nitrogen incorporation, SiC samples with properly prepared *flat* or *faceted* surfaces were considered. Cross-sectional SCM measurements provided information on the depth extension of N-compensated 4H-SiC and revealed a more efficient compensation in the faceted 4H-SiC sample.

Description of the experiment

SSRM is employed to investigate the changes in the resistivity of p^+-type doped 4H-SiC substrate regions selectively exposed to N_2O at 1150 °C for four hours, with respect to unexposed ones. The results of this analysis demonstrate that during the low-temperature (1150 °C) thermal treatment, N atoms are incorporated in SiC and a fraction of them occupy a substitutional position, becoming electrically active and acting as donors. The role played by 4H-SiC surface morphology on N incorporation has also been investigated, considering two different samples with a smooth (*flat*) and with a macroscopically stepped (*faceted*) surface, respectively. Details of the surface preparation of the samples can be found in the experimental section. Cross-sectional scanning capacitance microscopy (SCM) was used to profile the active doping concentration in the SiC interfacial region of MOS devices, showing a higher compensation for the *faceted* sample than for the *flat* one. Recently, we demonstrated that MOS on the *faceted* surface exhibit also a lower interface-state density ($\approx 3 \times 10^{11}$ $cm^{-2} \cdot eV^{-1}$) with respect to devices on the *flat* surface ($\approx 7 \times 10^{11}$ $cm^{-2} \cdot eV^{-1}$) [12,13]. Here, both the different values of D_{it} at SiO_2/4H-SiC interface and the different doping in the near interface SiC region have been explained in terms of the peculiar surface morphology of *faceted* samples, assuming a preferential nitrogen incorporation in the 4H-SiC substrate when it exposes a larger percentile of $(11-2n)$ planes.

Results and Discussion

To gain an insight into the effect of nitrogen on SiC during the annealing in N_2O, a patterned hard mask was defined onto a p^+-type SiC surface (as described in the Experimental section) in order to obtain regions selectively exposed and unexposed to N_2O. After the thermal treatment of the patterned samples (Figure 1a), the hard mask was removed (Figure 1b) followed by SSRM measurements on the bare SiC surface (Figure 1c) [14]. The SSRM map in Figure 1c shows a locally increased resistance in the SiC surface regions that were exposed to N_2O relative to the regions that were protected by the hard mask. Hence, through SSRM we are able to directly demonstrate that the introduction of nitrogen at the surface of SiC by exposure to N_2O and the low thermal budget (1150 °C) enables, surprisingly, a compensation effect that reduces the effective concen-

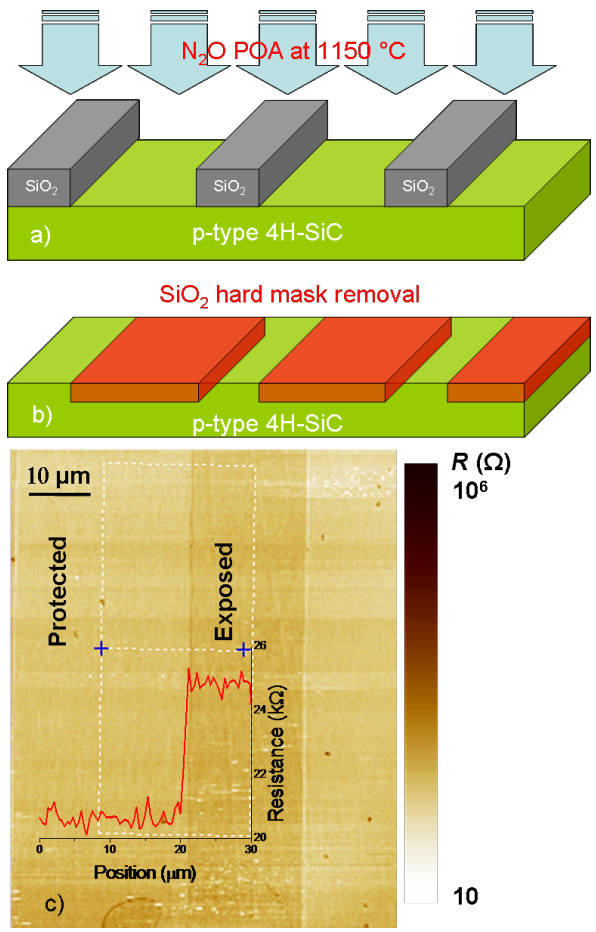

Figure 1: Schematic description of the POA treatment. (a) A SiO_2 hard mask is used to protect selectively the 4H-SiC during the POA. (b) After removal of the hard mask (by HF wet etch) on the 4H-SiC surface there are regions protected and exposed to the POA. (c) SSRM imaged on the patterned SiC surface; the two dimensional map of the substrate surface. The resistance line profile going from protected to exposed strips demonstrates a higher resistance value in the exposed region.

tration of p-type acceptors. Such a scenario has been previously proposed on the basis of physical measurements quantifying nitrogen incorporation and the reduction of D_{it} [3]. However, a direct measurement of the local electrical modifications has yet to be reported.

In the following it will be shown that this compensation effect due to nitrogen incorporation in the SiC near-surface region strongly depends on the SiC morphology, i.e., on the exposed planes at the interface with SiO_2. High-resolution scanning capacitance microscopy across the interface region was applied to get a deeper insight into this aspect. Figure 2 shows the SCM signal versus depth profiles collected both on the *faceted* and *flat* samples in the 40 nm 4H-SiC region under the SiO_2/SiC interface. The two depth profiles are laterally averaged over

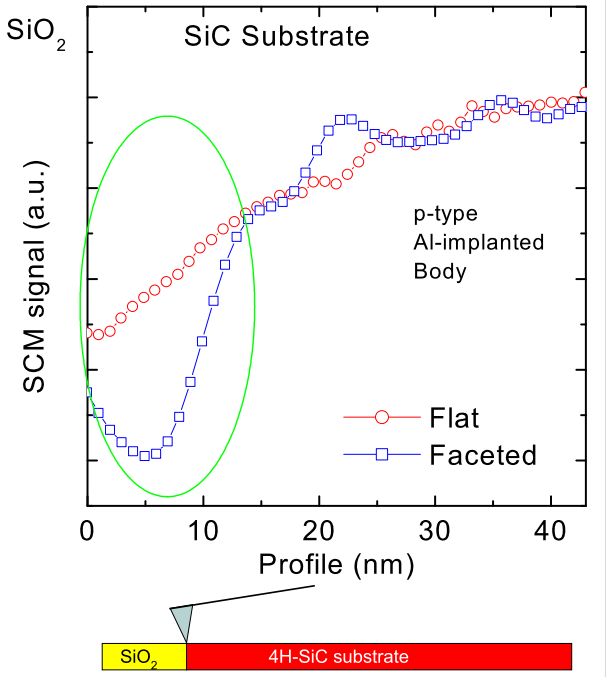

Figure 2: SCM profiling across the SiO_2/4H-SiC interfaces on the *faceted* (blue squares) and *flat* (red circles) samples respectively.

1 µm. They are almost coincident for depths greater than about 20 nm, while they are significantly different in the SiC interfacial region up to about 15 nm, where the SCM signal in the *faceted* sample is lower than in the *flat* sample. The lower SCM signal indicates a higher compensation of Al acceptors, which is consistent with a more efficient incorporation of substitutional (electrically active) nitrogen atoms in SiC.

The simultaneous presence of different planes at the SiO_2/4H-SiC interface in the *faceted* sample can be invoked to explain the better nitrogen incorporation during POA, leading to a more efficient passivation of interface traps and to a higher compensation of interfacial SiC. In fact, for a macroscopically stepped surface, the SiO_2/SiC interface is not only formed on the basal plane (0001), but a significant fraction of the interface area is formed on the (11−2*n*) facets [15]. Accordingly, a different efficiency of nitrogen incorporation on the (0001) and (11−2*n*) facets during the POA process could explain the different D_{it} values in the two samples.

Figure 3a shows the morphology profiles (acquired by AFM data in [12]) of the 4H-SiC substrates surfaces both for the faceted (blue squares) and flat (red circles) samples respectively. The surface roughness (RMS) was 0.36 nm and 1.75 nm for the flat sample and for the faceted sample, respectively. The facets have a typical height of about 5 nm and their orientation is correlated to the original miscut direction of the wafers. In the

present case, the substrates are cut along the (0001) basal plane with a 4° off-axis orientation toward the <11−20> direction. Each of these steps exposes both the (0001) basal plane and the plane along the <11−2*n*> direction. On the other hand, the flat sample shows no facets. The line profile in Figure 3a (circles) shows the typical 4H-SiC steps with ca. 0.5 nm height, corresponding to two Si–C pairs. This peculiar morphology of the interface can explain the macroscopic electrical behaviour of the capacitors (D_{it}).

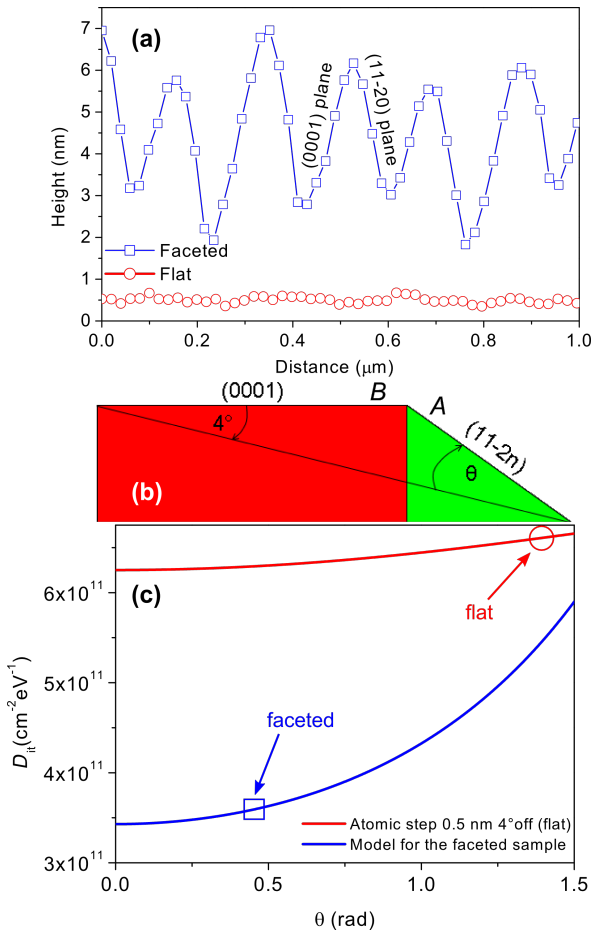

Figure 3: (a) AFM single scan line taken on the surfaces of the *faceted* and *flat* samples. (b) Schematic cross section of the basal-plane–facet orientation considering a 4° off-axis cut angle. (c) Simulated density of interface states for the ideal case and single atomic steps (red), and including the experimental measured facets (AFM section) changing the θ (11−2*n*) facet orientation (blue). The calculated values are compared with the experimental values.

In fact, for our MOS capacitors fabricated on a faceted surface as in Figure 3a, a significant fraction of the total SiO_2/4H-SiC interface area is formed on (11−2*n*) planes, with lower D_{it} than the basal plane (0001). This latter can justify the reduced D_{it} in the faceted sample.

Recently, Saitoh et al. demonstrated [15] the variation in the density of the interface states in MOS capacitors fabricated on 4H-SiC epilayers with different misorientation angles, moving from 8°, i.e., the (0001) largest basal plane, up to 90° toward the <11−20> direction, i.e., the (11−20) plane.

The D_{it} at 0.2 eV below the conduction band was found to decrease from $D_{it,(0001);8°\text{-off axis}} = 5 \times 10^{12}$ $cm^{-2}{\cdot}eV^{-1}$ for MOS capacitors fabricated on the (0001) face to $D_{it,(11-20)} = 3 \times 10^{11}$ $cm^{-2}{\cdot}eV^{-1}$ for capacitors on the (11−20) face. By geometrical calculations based on the AFM morphology in Figure 3a, it was possible to estimate the weighted average between the impact of the (11−2*n*) and the (0001) interface areas in terms of the macroscopic D_{it} measured values. The real experimental 4H-SiC structure can be schematically described as in Figure 3b (cross-section configuration).

Considering an ideal $D_{it,(0001)} = 1 \times 10^{12}$ $cm^{-2}{\cdot}eV^{-1}$ (for the 0° off-axis angle) at 0.2 eV from the conduction band edge, higher than the interface state density in the face (11−20), the total macroscopic density of interface states can be written:

$$D_{it;macroscopic} = n\left(D_{it,(11-20)}\frac{A}{A+B} + D_{it,(0001)}\frac{B}{A+B}\right) \quad (1)$$

where

$$n = S\Big/\Big(B\cos\theta + A\cos\left(90° - \theta\right)\Big) \quad (2)$$

And where S is a scale factor, A and B are the mean experimental dimensions of the (11−2*n*) facets and of the basal planes, respectively (taken from the AFM profiles in Figure 3a). Moreover, the angle θ is the incremental angle with respect to the off-axis cut angle [16].

Equations 1 and 2 predict the total macroscopic D_{it}, which is the geometrically weighted average between the two limiting conditions, i.e., the interface state density along the (11−20) plane ($D_{it,(11-20)}$) and the interface state density along the (0001) plane ($D_{it,(0001)}$). For the flat sample the used parameters are based on A = 0.5 nm, $B = A/\tan 4°$ (4° miscut angle). The final D_{it} value is found taking the value for θ = (90 – 4)° because in the ideal case no facet is formed (Figure 3c). For the faceted sample the used parameters are based on A = 4.5 nm and B = 5.5 nm. The final D_{it} value can be found by taking the variable value θ from 10–20°, because the facet is formed and its angle can vary between 10 and 20°, as reported in the literature [17]. The simulations explain perfectly the experimental results. Figure 3c compares the calculated curves that took to

account the geometrical configuration of the SiO_2/4H-SiC interface in the two cases and the experimental D_{it} value measured on MOS prototypes. Recently, J. Rozen et al. [3] pointed out that the D_{it} reduction is strongly correlated to the nitrogen incorporation during the POA. Now it is possible to associate the lowering of the density of the interface states (in the faceted sample) with enhanced nitrogen incorporation during the POA when the sample surface exposes a higher percentage of (11−20) planes of the SiO_2/4H-SiC interface.

Conclusion

In this paper, the electrical activation of the nitrogen incorporated in the SiC near-surface region during low-temperature POA has been demonstrated. Moreover, nanometre-scale cross-sectional SCM investigation figured out the depth profile of the activated nitrogen. A correlation between the electrostructural properties of SiO_2/4H-SiC interfaces and the interface-state density of MOS was established. In particular, irrespective of the different interface roughness, lower values of D_{it} were found in the faceted sample. The different values of the interface states density can be explained by the peculiar surface morphology of the devices channel region with particular regard to the different nitrogen incorporation through interfaces exposing different ratios between (0001) and (11−20) planes.

Experimental

Scanning Probe Microscopy (SPM) measurements were carried out by using a Digital Instrument D3100 equipped with the Nanoscope® V controller. Local resistance measurements were carried out by using the scanning spreading resistance module (SSRM) [18,19], and cross-sectional local active-doping profiling was carried out employing differential capacitance (dC/dV) imaging with the scanning capacitance module (SCM) [20,21].

The MOS capacitor for the measurements of D_{it} was fabricated on an n-type 4H-SiC epitaxial layer grown onto heavily doped n^+-type substrates with a 4° off-axis disorientation towards the <11−20> direction. [22]. A 30 nm thick SiO_2 layer deposited by plasma-enhanced chemical vapour deposition was used as the gate dielectric. After deposition of the gate oxide, a POA annealing at 1150 °C was performed under an N_2O atmosphere.

MOSFET devices were fabricated on two different surfaces (*flat* and *faceted*). Both samples were subjected to p-type doping by Al ion implantation and to a subsequent high-temperature (1650 °C) postimplantation annealing for dopant activation. On one sample, the SiC surface was coated by a protective carbon capping layer during the annealing, resulting in a smooth morphology. A rough surface formed by facets exposing both the (0001) basal plane and the (11−2n) facets, was obtained for the second sample annealed without the cap layer. MOS capacitors were fabricated on both wafers [12]. Cross-sectional SCM was performed for carrier-depth profiling under the gate oxide region.

The sample for the selective exposure of 4H-SiC bare surface to the postoxidation annealing (POA) was fabricated as follows: the surface of a p^+-type 4H-SiC layer was selectively exposed to the same POA process in N_2O, by using a pattern width of 20 μm of exposed substrate separated by 40 μm of protected substrate onto a thick SiO_2 hard mask. After removing the hard mask, SSRM was performed on bare 4H-SiC exposed to cleaning, wet-etching in diluted HF, and standard rinsing.

Acknowledgements

The authors would like to thank S. Di Franco for his support during fabrication of the device prototypes. ST Microelectronics R&D in Catania is acknowledged for funding and invaluable assistance. This work was partially funded by the Marie Curie ITN NetFISiC (EC FP7 grant agreement no. 264613), by the national project PON Ambition Power (PON01_00700), and by ST Microelectronics, Catania (under the research contract 04.03.2011.002 D.B. Legal Dept. 3774).

References

1. Ciobanu, F.; Pensl, G.; Afanas'ev, V. V.; Schöner, A. *Mater. Sci. Forum* **2005,** *483–485,* 693–696. doi:10.4028/www.scientific.net/MSF.483-485.693
2. Afanas'ev, V. V.; Ciobanu, F.; Dimitrijev, S.; Pensl, G.; Stesmans, A. *J. Phys.: Condens. Matter* **2004,** *16,* S1839–S1856. doi:10.1088/0953-8984/16/17/019
3. Rozen, J.; Ahyi, A. C.; Zhu, X.; Williams, J. R.; Feldman, L. C. *IEEE Trans. Electron Devices* **2010,** *58,* 3808–3811. doi:10.1109/TED.2011.2164800
4. Wang, Y.; Khan, T.; Koushik Balasubramanian, M.; Naik, H.; Wang, W.; Chow, T. P. *IEEE Trans. Electron Devices* **2008,** *55,* 2046–2053. doi:10.1109/TED.2008.926674
5. Ryu, S.-H.; Dhar, S.; Haney, S.; Agarwal, A.; Lelis, A.; Geil, B.; Scozzie, C. *Mater. Sci. Forum* **2009,** *615–617,* 743–748. doi:10.4028/www.scientific.net/MSF.615-617.743
6. Kosugi, R.; Umeda, T.; Sakuma, Y. *Appl. Phys. Lett.* **2011,** *99,* 182111. doi:10.1063/1.3659689
7. Umeda, T.; Esaki, K.; Kosugi, R.; Fukuda, K.; Ohshima, T.; Morishita, N.; Isoya, J. *Appl. Phys. Lett.* **2011,** *99,* 142105. doi:10.1063/1.3644156
8. Osterman, J.; Hallén, A.; Anand, S. *Appl. Phys. Lett.* **2002,** *81,* 3004–3006. doi:10.1063/1.1514829
9. Song, X.; Bazin, A. E.; Michaud, J. F.; Cayrel, F.; Zielinski, M.; Portail, M.; Chassagne, T.; Collard, E.; Alquier, D. *Mater. Sci. Forum* **2011,** *679–680,* 193–196. doi:10.4028/www.scientific.net/MSF.679-680.193
10. Giannazzo, F.; Calcagno, L.; Raineri, V.; Ciampolini, L.; Ciappa, M.; Napolitani, E. *Appl. Phys. Lett.* **2001,** *79,* 1211. doi:10.1063/1.1394956

11. Giannazzo, F.; Musumeci, P.; Calcagno, L.; Makhtari, A.; Raineri, V. *Mater. Sci. Semicond. Process.* **2001,** *4,* 195. doi:10.1016/S1369-8001(00)00129-3
12. Frazzetto, A.; Giannazzo, F.; Fiorenza, P.; Raineri, V.; Roccaforte, F. *Appl. Phys. Lett.* **2011,** *99,* 072117. doi:10.1063/1.3627186
13. Fiorenza, P.; Giannazzo, F.; Frazzetto, A.; Roccaforte, F. *J. Appl. Phys.* **2012,** *112,* 084501. doi:10.1063/1.4759354
14. Swanson, L. K.; Fiorenza, P.; Giannazzo, F.; Frazzetto, A.; Roccaforte, F. *Appl. Phys. Lett.* **2012,** *101,* No. 193501. doi:10.1063/1.4766175
15. Saitoh, H.; Seki, A.; Manabe, A.; Kimoto, T. *Mater. Sci. Forum* **2007,** *556–557,* 659–662. doi:10.4028/www.scientific.net/MSF.556-557.659
16. Nakagawa, H.; Tanaka, S.; Suemune, I. *Phys. Rev. Lett.* **2003,** *91,* 226107. doi:10.1103/PhysRevLett.91.226107
17. Camarda, M.; Severino, A.; Fiorenza, P.; Raineri, V.; Scalese, S.; Bongiorno, C.; La Magna, A.; La Via, F.; Mauceri, M.; Crippa, D. *Mater. Sci. Forum* **2011,** *679–680,* 358–361. doi:10.4028/www.scientific.net/MSF.679-680.358
18. Eyben, P.; Xu, M.; Duhayon, N.; Clarysse, T.; Callewaert, S.; Vandervorst, W. *J. Vac. Sci. Technol., B* **2002,** *20,* 471–478. doi:10.1116/1.1424280
19. Giannazzo F; Roccaforte F; Raineri, V. *Appl. Phys. Lett.* **2007,** *91,* 202104. doi:10.1063/1.2813022
20. Fiorenza, P.; Raineri, V.; Ebbinghaus, S. G.; Lo Nigro, R. *CrystEngComm* **2011,** *13,* 3900–3904. doi:10.1039/c0ce00948b
21. Fiorenza, P.; Raineri, V.; Ferrarelli, M. C.; Sinclair, D. C.; Lo Nigro, R. *Nanoscale* **2011,** *3,* 1171–1175. doi:10.1039/c0nr00828a
22. Schroder, D.K. *Semiconductor Material and Device Characterization,* 3rd ed.; John Wiley and Sons: Hoboken, New Jersey, 2006. doi:10.1002/0471749095

License and Terms

Beilstein Journal of Nanotechnology

Photoelectrochemical and Raman characterization of In_2O_3 mesoporous films sensitized by CdS nanoparticles

Mikalai V. Malashchonak[1], Sergey K. Poznyak[1], Eugene A. Streltsov[1], Anatoly I. Kulak[2], Olga V. Korolik[1] and Alexander V. Mazanik[*1]

Full Research Paper

Open Access

Address:
[1]Belarusian State University, Nezalezhnastsi Av. 4, Minsk 220030, Belarus and [2]Institute of General and Inorganic Chemistry, National Academy of Sciences of Belarus, Surganova str., 9/1, Minsk 220072, Belarus

Email:
Alexander V. Mazanik* - amazanik1@rambler.ru

* Corresponding author

Keywords:
cadmium sulfide (CdS); indium oxide (In_2O_3); nanoparticles; successive ionic layer adsorption and reaction (SILAR)

Beilstein J. Nanotechnol. **2013,** *4,* 255–261.
doi:10.3762/bjnano.4.27

Received: 27 October 2012
Accepted: 21 March 2013
Published: 11 April 2013

This article is part of the Thematic Series "High-resolution electrical and chemical characterization of nm-scale organic and inorganic devices".

Associate Editor: N. Motta

Abstract

The method of successive ion layer adsorption and reaction was applied for the deposition of CdS nanoparticles onto a mesoporous In_2O_3 substrate. The filling of the nanopores in In_2O_3 films with CdS particles mainly occurs during the first 30 cycles of the SILAR deposition. The surface modification of In_2O_3 with CdS nanoparticles leads to the spectral sensitization of photoelectrochemical processes that manifests itself in a red shift of the long-wavelength edge in the photocurrent spectrum by 100–150 nm. Quantum-confinement effects lead to an increase of the bandgap from 2.49 to 2.68 eV when decreasing the number of SILAR cycles from 30 to 10. The spectral shift and the widening of the Raman line belonging to CdS evidences the lattice stress on the CdS/In_2O_3 interfaces and confirms the formation of a close contact between the nanoparticles.

Introduction

In third-generation solar cells molecular dyes (in the Grätzel cells [1]) as well as nanoparticles of semiconducting metal chalcogenides (CdS, CdSe, CdTe, PbS, PbSe, Ag_2S, Bi_2S_3 and others) immobilized onto the surface of mesoporous films of wide-bandgap oxides (TiO_2, ZnO, SnO_2, Nb_2O_5, Ta_2O_5, WO_3, In_2O_3) are used as the sensitizing components [2-5]. It is considered that the best technique for the in situ deposition of such nanoparticles is the successive ionic layer adsorption and reaction (SILAR) method [6-11], which allows the precise control of the growth of the nanoparticles. To efficiently inject electrons from the photo-excited semiconductor nanoparticles or molecular dyes into the oxide matrix, the energy of the oxide conduction-band edge (E_c) should be lower than the lowest unoccupied level (LUMO) of the sensitizer, to which the electrons from the highest occupied level are transferred under photoexcitation. The sensitizing efficiency of the photoelectro-

chemical system depends on (a) the efficiency of separation of the photo-induced charge-carriers at the sensitizer, (b) a wide-bandgap oxide interface that is mainly determined by the difference $E_{LUMO} - E_c$, as well as (c) on the further transport of the charge carriers through the mesoporous oxide matrix to the substrate. Previous investigations have demonstrated that, in comparison to TiO_2, In_2O_3 possesses higher electron affinity [12] allowing the use of sensitizers with a smaller bandgap $E_g = E_{LUMO} - E_{HOMO}$. Besides, indium oxide is characterized by an essentially higher (by an order of magnitude) lifetime of the injected photoelectrons [12]. Interest in a more profound investigation of nanostructured In_2O_3 sensitization is also explained by the fact that the E_c level of In_2O_3 can be managed by the thermal treatment during preparation by the sol–gel method.

The aim of this work was to investigate the photoelectrochemical behavior of mesoporous nanocrystalline In_2O_3 films sensitized by CdS nanoparticles and to characterize these systems by using different methods (SEM, TEM, AES, UV–vis absorption, BET surface area measurements and Raman spectroscopy).

Experimental

Mesoporous In_2O_3 films were prepared by spin-coating deposition of a colloidal indium hydroxide solution onto transparent ITO-coated glass or quartz (for optical measurements) substrates with a subsequent thermal treatment for 1 h in air. To study the effect of the spectral sensitization we used two kinds of In_2O_3 films: films annealed at 200 °C (hereafter referred to as In_2O_3(200)) and films annealed at 400 °C (hereafter referred to as In_2O_3(400)). The indium hydroxide sol was obtained as described in detail in [13]. Briefly, the indium hydroxide was precipitated by the titration of a 0.25 M $In(NO_3)_3$ aqueous solution with a concentrated NH_3 solution under vigorous stirring at 0 °C. The precipitate was then thoroughly washed and ultrasonically treated after the addition of a small amount of nitric acid as a stabilizer to obtain a stable sol at a concentration of 120 g/L. To prepare indium oxide In_2O_3(400) films with mesoporous structure, block-copolymer Pluronic F127 (100 g/L) as a template material was added into the obtained indium hydroxide sol.

CdS nanoparticles were deposited onto the In_2O_3 films by the successive ion layer adsorption and reaction (SILAR) technique. This involved the dipping of the In_2O_3 film in a 1 M $Cd(NO_3)_2$ ethanolic solution for 5 min, rinsing it with distilled water, then dipping it for another 5 min in a 1 M Na_2S aqueous solution and rinsing it again with distilled water. The deposition cycle was repeated 10–50 times, and finally, the sample was thoroughly rinsed with distilled water and air dried.

The prepared samples were characterized by SEM, TEM, BET surface area measurements, AES, photoelectrochemical methods, and UV–vis and micro-Raman spectroscopy. SEM and TEM images were obtained using a Hitachi S 4800 field emission scanning electron microscope and a LEO-906E transmission electron microscope, respectively. BET surface area measurements were carried out by using an ASAP2020MP analyzer of surface area and porosity. The Auger spectroscopy method in combination with ion etching was realized by using a PHI-660 Auger microprobe. Photoelectrochemical measurements were carried out in a standard two-compartment three-electrode cell involving a platinum counter-electrode and a Ag|AgCl|KCl (sat.) electrode as the reference electrode (+0.201 V versus SHE). The cell was controlled by a conventional programmable potentiostat. Photocurrent spectra were obtained by using a setup equipped with a high-intensity grating monochromator, a 1 kW xenon lamp and a slowly rotating light chopper (0.3 Hz). Spectral dependencies of the photocurrent were corrected for the spectral intensity distribution of the monochromator output. UV–vis absorption spectra of the films deposited onto quartz substrates were recorded on a Shimadzu UV-2550 spectrophotometer. Raman spectra were taken at room temperature by using a Nanofinder High End (Lotis TII, Belarus–Japan) confocal-microscope-based setup. Raman scattering was excited by using a 473 nm solid-state laser. The laser power level at the sample was maintained at ca. 25 μW to minimize laser-induced damage to the CdS nanoparticles. The backscattered light, not analyzed for its polarization, was dispersed by using a 0.55 m single grating spectrometer (spectral resolution better than 1 cm^{-1}) and detected by a cooled CCD camera. The signal accumulation time was typically equal to 600 s. The spectral calibration with an accuracy better than 1 cm^{-1} was carried out by using a built-in gas-discharge lamp.

Results and Discussion

TEM images of the prepared films demonstrating their highly porous and nanocrystalline structure are shown in Figure 1. The microdiffraction pattern (inset of Figure 1b) indicates the presence of hexagonal CdS in the sensitized In_2O_3 films. The cross-sectional SEM image of a film deposited on an ITO substrate shows that the film thickness is about 40 nm (Figure 2a). According to the BET data, the surface areas of the In_2O_3(400) films prepared with and without Pluronic F127 are 119 and 53 m^2/g, respectively. It should be noted that the addition of Pluronic to the indium hydroxide sol leads to a significantly narrower pore-size distribution with an average pore diameter of ca. 5 nm (Figure 3).

Figure 4 shows the absorption spectra of the In_2O_3 films with deposited CdS nanoparticles. As can be seen clearly from Figure 4, the steepest rise in the absorbance is observed when

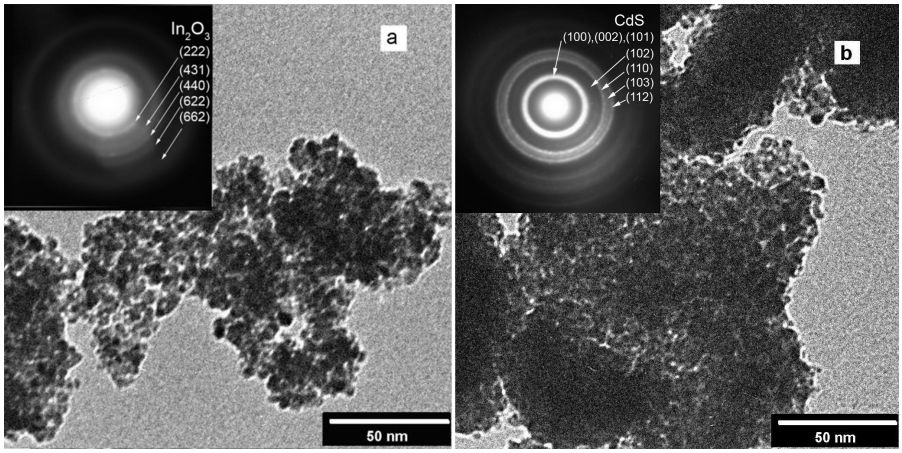

Figure 1: TEM images and electron diffraction patterns (insets) for In_2O_3(400) (a) and In_2O_3(400) after 30 SILAR CdS deposition cycles (b).

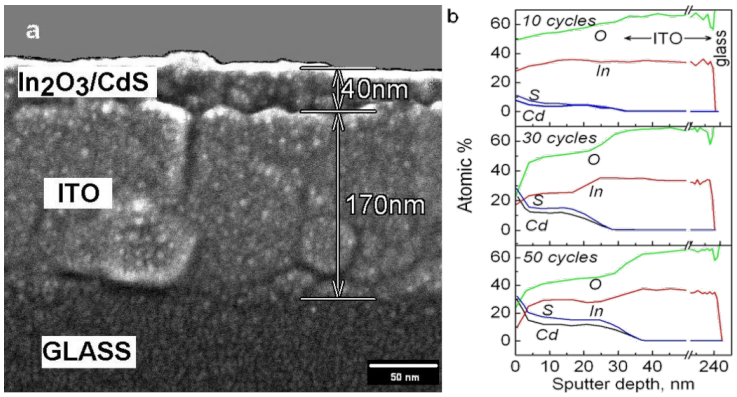

Figure 2: Cross-sectional SEM image of the In_2O_3(400) film after 30 SILAR CdS deposition cycles (a) and AES profiles for In_2O_3(400)/CdS structures with different numbers of SILAR cycles (b). Scaling from sputter time to depth in AES profiles was done on the basis of cross-sectional SEM data.

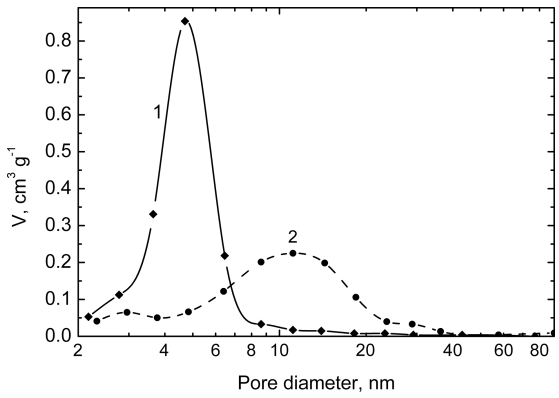

Figure 3: Barrett–Joyner–Halenda desorption-model pore-volume distribution of the In_2O_3(400) mesoporous films prepared with (1) and without (2) Pluronic F127.

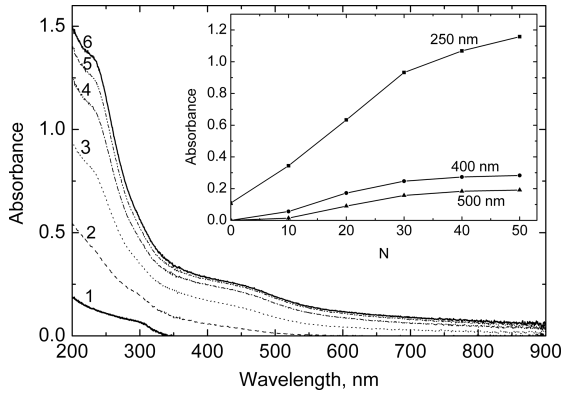

Figure 4: Absorption spectra of the In_2O_3(400) and In_2O_3(400)/CdS films deposited onto a quartz substrate. The number of SILAR cycles of the CdS deposition are as follows: 0 (1); 10 (2); 20 (3); 30 (4); 40 (5); 50 (6). The inset shows the dependencies of the absorbance at different wavelengths on the number of SILAR cycles.

increasing the number of SILAR cycles from 10 to 30. The absorbance does not change notably with the further deposition of CdS, indicating that the filling of the nanopore volume in In_2O_3 films with CdS particles occurs mainly during the first 30 cycles of SILAR deposition. According to the Auger profiles shown in Figure 2b, the film pores are filled rather uniformly at the initial stages of the SILAR deposition. Onwards, when the pore space is mostly filled, CdS nanocrystals continue to grow predominately on the top of the film.

The In_2O_3(400)/CdS films were also characterized by Raman spectroscopy. Raman spectra of all samples in the spectral range studied (0–1000 cm^{-1}) show the CdS LO phonon mode (≈300 cm^{-1}) with its two overtones, which correspond to two- (≈600 cm^{-1}) and three-phonon (≈900 cm^{-1}) processes. Figure 5 presents the Raman spectrum of the In_2O_3(400)/CdS system prepared by using 40 SILAR cycles. One phonon peak for CdS has a complex structure. The peak fitting by superposition of Lorentz lines allowed for the determination of position, full width at half maximum (FWHM) and relative intensity of the different components. The peak at ≈270 cm^{-1} can be associated with CdS surface phonons [14]. The peaks at ≈242 cm^{-1}, ≈318 cm^{-1} and ≈342 cm^{-1} are not characteristic of In_2O_3 (which has Raman modes at approximately 308, 365, 504 and 637 cm^{-1} [15,16]) and are not observed for the In_2O_3 substrate without deposited CdS. The presence of these peaks in the Raman spectra can testify to the fact that the samples studied contain not only In_2O_3 and CdS, but also some additional phases formed during the SILAR process. High values of the FWHM of the LO phonon peak can point to both a significant degree of CdS nanocrystal disorder and size heterogeneity (Figure 6).

As can be seen from Figure 6, the CdS phonon energy decreases with increasing the number of SILAR cycles (i.e., the nanocrystal size). This effect can be explained in the following way: according to wavevector-relaxation [17] and continuum [18,19] models, the decrease of the size of the nanoparticles leads to a monotonic red shift of the phonon energy relative to the value characteristic of a bulk crystal. This effect was observed by a number of researchers who studied nanocrystals produced by colloidal chemistry methods [20-22]. However, in our experiments where the nanoparticles were grown in situ (directly on the indium oxide substrate) it is also necessary to take into account their interaction with the host material. A similar approach was applied in the works [23] and [24] to explain Raman spectra of CdS_xSe_{1-x} and CdSe embedded in different glass matrixes. The lattice mismatch between CdS and the host material can cause compressive stress in CdS nanocrystals which leads to an increase of the atomic interaction and hence to a phonon energy increase. The latter could explain the blue shift of the peak position that is observed when decreasing the number of SILAR cycles. In contrary, when the number of deposition cycles increases, the influence of the substrate diminishes and the CdS phonon energy decreases.

The In_2O_3 prepared films absorb predominantly UV light with $\lambda < 400$ nm since they have a relatively wide bandgap (2.87 eV for In_2O_3(200) and 2.73 eV for In_2O_3(400), indirect optical transitions) [13]. Under external polarization and UV illumination the In_2O_3 electrodes generate an anodic photocurrent because indium oxide is an n-type semiconductor. It is remarkable that the onset potential of the photocurrent is shifted to the positive direction by approximately 700 mV when increasing the temperature of the oxide annealing (Figure 7).

Figure 8 shows the photocurrent–potential curves recorded under visible-light illumination of In_2O_3(200)/CdS and

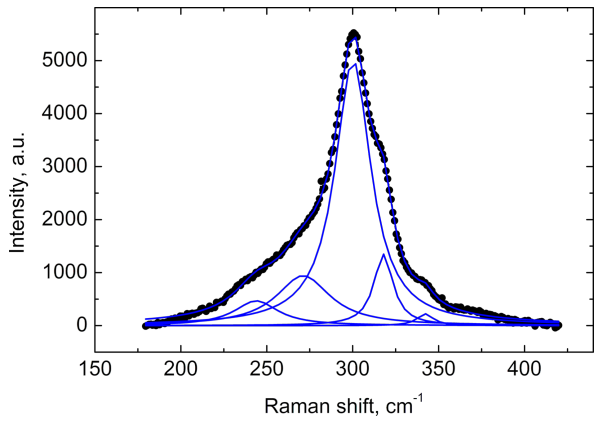

Figure 5: Raman spectrum of the In_2O_3(400)/CdS system prepared by using 40 SILAR cycles of CdS deposition after background subtraction (circles) and its fitting by the superposition of five Lorentz lines.

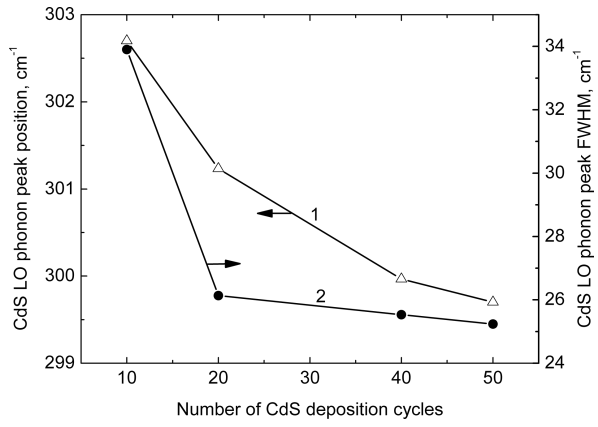

Figure 6: Dependence of the CdS LO phonon peak position (1) and FWHM (2) on the number of SILAR cycles.

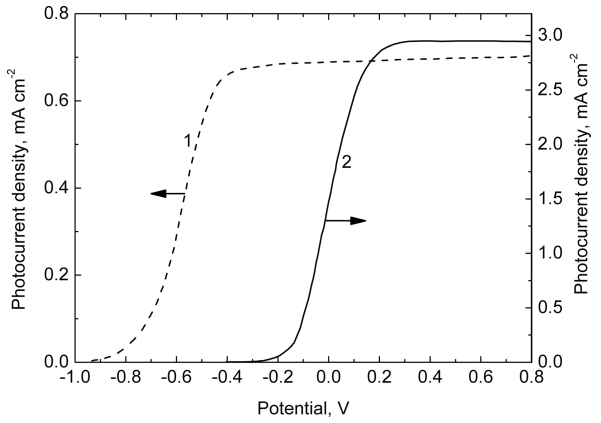

Figure 7: Photocurrent versus electrode-potential curves recorded under UV illumination of the mesoporous In_2O_3 electrodes annealed at 200 °C (1) and 400 °C (2). Electrolyte: 0.1 M KOH solution.

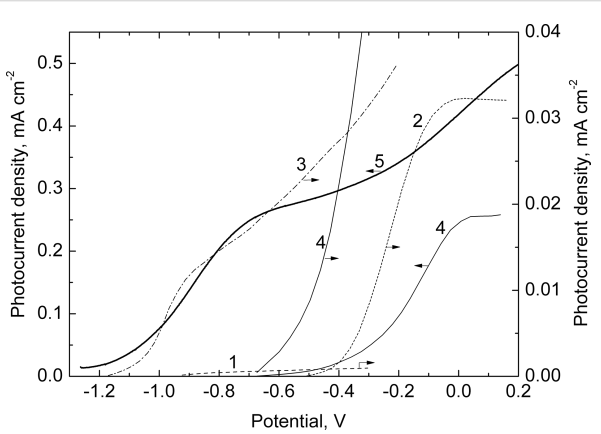

Figure 8: Photocurrent versus electrode potential curves recorded under visible-light illumination of the In_2O_3 (1, 2) and In_2O_3/CdS electrodes (3–5). The In_2O_3 films were annealed at 200 (1, 3) and 400 °C (2, 4, 5). The number of the SILAR cycles of CdS deposition was 10 (3, 4) and 50 (without the step of intermediate rinsing with distilled water, 5). Electrolyte: 0.1 M Na_2S + 0.1 M Na_2SO_3 + 0.1 M NaOH solution.

In_2O_3(400)/CdS heterostructures (curves 3 and 4) in an S^{2-}-containing electrolyte. For comparison, similar dependencies for nonsensitized In_2O_3(200) and In_2O_3(400) electrodes are also presented (curves 1 and 2). The sensitized photocurrent for In_2O_3(400)/CdS is ten times higher than that for In_2O_3(200)/CdS. The onset potentials, E_{on}, of the sensitized photocurrent correlate essentially with the corresponding E_{on} values for nonsensitized In_2O_3(200) and In_2O_3(400) and differ one from another by approximately 500 mV.

It is known that the E_{on} value as a first approximation can be identified as the energy level of the conduction-band edge (E_c) of a semiconductor. The thinnest (approximately 1 nm) hydroxide layer has been previously shown [13] to be formed at the In_2O_3(200) surface. This layer seems to be of crucial importance in changing the potential drop in the Helmholtz layer of the electrode and consequently in changing the E_c level on the potential scale. Thus, it can be concluded that the energy diagram of the In_2O_3/CdS heterostructure is primarily determined by the structure of the oxide surface being in contact with the electrolyte. By controlling the state of this surface it is possible to change the E_{on} value and therefore the photovoltage of the corresponding PEC cell.

Very fine CdS particles (approximately several nanometers) seem to form on the surface of mesoporous In_2O_3 at a relatively small number of SILAR cycles (up to 30–40), as evidenced by the revealed quantum-size effect. The further increase in the SILAR cycle number (up to 50 and above) can result in the formation of a bulk CdS film on the In_2O_3 surface. To simulate the transition from nanoparticles to the bulk cadmium sulfide, a thick (several hundreds of nanometers) CdS film was deposited onto the surface of In_2O_3(400). When preparing this film, the step of intermediate rinsing of the samples with distilled water necessary to remove surplus Cd^{2+} and S^{2-} ions from the surface was omitted.

When depositing the bulk CdS, the isotype n-In_2O_3/n-CdS heterojunction with the external narrow-bandgap semiconductor is formed. In contrast to nanoparticles, the space-charge region can be formed in this bulk semiconductor. As can be inferred from the photoelectrochemical behaviour of this system (Figure 8, curve 5), its solid-state heterojunction is not a barrier for photogenerated electrons. A distinctive feature of the photocurrent–potential curves of the heterojunction is the sharp shift of the onset potential to a more negative potential (E_{on} = −1.2 V). In this case, the E_{on} value is already determined by the position of the conduction band edge of CdS.

Figure 9 presents the photocurrent spectra of the In_2O_3(400)/CdS heterostructure. The SILAR deposition of CdS nanoparticles onto the In_2O_3 films leads to an extension of the long-wave edge of the photocurrent spectra up to 550 nm. Although the photocurrent increases in the whole spectral region studied when increasing the number of SILAR cycles, the greatest increase in photocurrent is observed at $\lambda > 450$ nm, i.e., outside the region of the indium oxide bandgap absorption.

Analysis of the photocurrent spectra in coordinates of $(Y \cdot h\nu)^2$ versus $h\nu$ typical for direct optical transitions inherent in CdS shows that the bandgap of CdS decreases from 2.68 eV at 10 SILAR cycles to 2.49 eV at 30 cycles and to 2.42 eV at 50 cycles (Figure 10). The E_g value of 2.42 eV corresponds to the optical bandgap of bulk CdS. The observed increase in E_g with the decreasing number of SILAR cycles can be explained

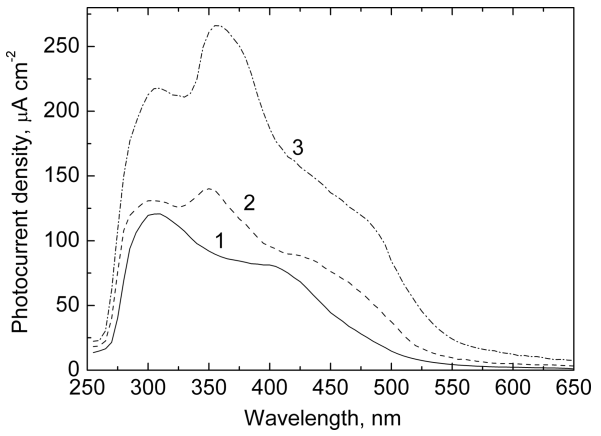

Figure 9: Photocurrent spectra of In_2O_3(400)/CdS film electrodes in 0.1 M Na_2S + 0.1 M Na_2SO_3 + 0.1 M NaOH solution. The spectra were measured at a potential of −0.1 V versus Ag/AgCl. The number of the SILAR cycles of CdS deposition was 10 (1), 30 (2) and 50 (3).

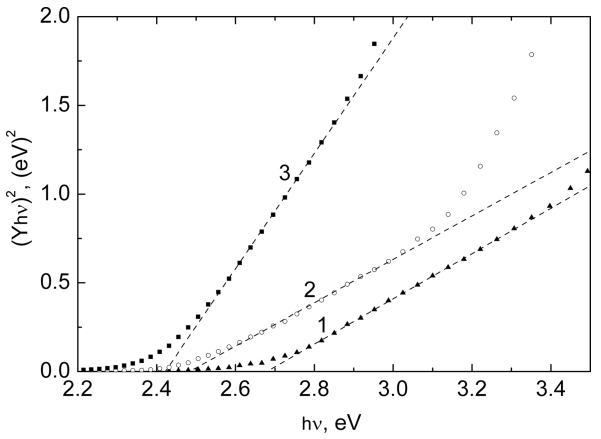

Figure 10: Analysis of the photocurrent spectra shown in Figure 9 in coordinates of $(Y \cdot h\nu)^2$ versus $h\nu$ typical for direct optical transitions for In_2O_3(400)/CdS film electrodes. The number of the SILAR cycles of CdS deposition was 10 (1), 30 (2) and 50 (3).

by the well-known quantum-confinement effect related to the discretization of energy levels in nanoparticles and the increase in the energy gap between LUMO and HOMO levels with the decreasing size of the semiconductor particles [25].

Conclusion

The effect of spectral sensitization of photoelectrochemical processes on nanocrystalline mesoporous In_2O_3 electrodes by CdS has been revealed. This effect takes place when CdS nanoparticles are deposited on the In_2O_3 surface by the method of successive ion layer adsorption and reaction (SILAR) and manifests itself as a red shift of the spectral sensitivity of the electrochemical system by about 100–150 nm. The onset potential of the sensitized photocurrent for the In_2O_3/CdS nano-heterostructure is determined by the energy position of the oxide conduction-band edge, which is controlled by the thermal treatment of In_2O_3. A rise in the oxide annealing temperature from 200 to 400 °C leads to the shift of photocurrent onset potential for the In_2O_3/CdS nano-heterostructure by approximately 500 mV in the positive direction and results in a rise of the photocurrent by an order of magnitude.

When increasing the number of cycles of CdS deposition, gradual filling of nanopores of the indium oxide film by CdS particles occurs resulting in a rise of the optical absorbance of the In_2O_3/CdS films and in an increase of the photocurrent of the corresponding electrodes. Quantum-confinement effects are observed in the photocurrent spectra and lead to a bandgap increase from 2.49 to 2.68 eV when decreasing the number of SILAR cycles from 30 to 10.

The deposition of the bulk CdS on the surface of In_2O_3 films results in the formation of an isotype In_2O_3/CdS heterojunction with external narrow band-gap component. The generation and separation of photoelectrons and photoholes in this case occur primarily in the CdS at the interface with the electrolyte, and the value of the onset potential is determined by the energy position of the conduction-band edge of bulk CdS.

Raman spectroscopy data show that due to the close contact at the CdS/host-material heterojunction the lattice stress in the CdS nanoparticles rises during the deposition process, which manifests itself in changes of the position of the CdS LO phonon peak and of its width.

Acknowledgements

We thank V.I. Shautsova for carrying out the TEM experiments. This work was supported by Research Program “Electronics and Photonics” of the Republic of Belarus (contract No 1.2.05).

References

1. Grätzel, M. *Nature* **2001,** *414,* 338–344. doi:10.1038/35104607
2. Vogel, R.; Hoyer, P.; Weller, H. *J. Phys. Chem.* **1994,** *98,* 3183–3188. doi:10.1021/j100063a022
3. Rühle, S.; Shalom, M.; Zaban, A. *ChemPhysChem* **2010,** *11,* 2290–2304. doi:10.1002/cphc.201000069
4. Kamat, P. V. *J. Phys. Chem. C* **2008,** *112,* 18737–18753. doi:10.1021/jp806791s
5. Katoh, R.; Furube, A.; Yoshihara, T.; Hara, K.; Fujihashi, G.; Takano, S.; Murata, S.; Arakawa, H.; Tachiya, M. *J. Phys. Chem. B* **2004,** *108,* 4818–4822. doi:10.1021/jp031260g
6. Nicolau, Y. F. *Appl. Surf. Sci.* **1985,** *22–23,* 1061–1074. doi:10.1016/0378-5963(85)90241-7
7. Pathan, H.; Lokhande, C. *Bull. Mater. Sci.* **2004,** *27,* 85–111. doi:10.1007/BF02708491

8. Baker, D. R.; Kamat, P. *Adv. Funct. Mater.* **2009,** *19,* 805–811. doi:10.1002/adfm.200801173
9. Ahmed, R.; Will, G.; Bell, J.; Wang, H. *J. Nanopart. Res.* **2012,** *14,* 1140–1153. doi:10.1007/s11051-012-1140-x
10. Cheng, S.; Fu, W.; Yang, H.; Zhang, L.; Ma, J.; Zhao, H.; Sun, M.; Yang, L. *J. Phys. Chem. C* **2012,** *116,* 2615–2621. doi:10.1021/jp209258r
11. Rabinovich, E.; Hodes, G. *J. Phys. Chem. C* **2013,** *117,* 1611–1620. doi:10.1021/jp3105453
12. Mori, S.; Asano, A. *J. Phys. Chem. C* **2010,** *114,* 13113–13117. doi:10.1021/jp1019203
13. Poznyak, S. K.; Kulak, A. I. *Electrochim. Acta* **2000,** *45,* 1595–1605. doi:10.1016/S0013-4686(99)00319-9
14. Roy, A.; Sood, A. K. *Phys. Rev. B* **1996,** *53,* 12127–12132. doi:10.1103/PhysRevB.53.12127
15. White, W. B.; Keramidas, V. G. *Spectrochim. Acta, Part A* **1972,** *28,* 501–509. doi:10.1016/0584-8539(72)80237-X
16. Korotcenkov, G.; Brinzari, V.; Ivanov, M.; Cerneavschi, A.; Rodriguez, J.; Cirera, A.; Cornet, A.; Morante, J. *Thin Solid Films* **2005,** *479,* 38–51. doi:10.1016/j.tsf.2004.11.107
17. Richter, H.; Wang, Z. P.; Ley, L. *Solid State Commun.* **1981,** *39,* 625–629. doi:10.1016/0038-1098(81)90337-9
18. Roca, E.; Trallero-Giner, C.; Cardona, M. *Phys. Rev. B* **1994,** *49,* 13704–13711. doi:10.1103/PhysRevB.49.13704
19. Trallero-Giner, C.; Debernardi, A.; Cardona, M.; Menéndez-Proupín, E.; Ekimov, A. I. *Phys. Rev. B* **1998,** *57,* 4664–4669. doi:10.1103/PhysRevB.57.4664
20. Nien, Y.-T.; Zaman, B.; Ouyang, J.; Chen, I.-G.; Hwang, C.-S.; Yu, K. *Mater. Lett.* **2008,** *62,* 4522–4524. doi:10.1016/j.matlet.2008.08.023
21. Romčević, N.; Kostić, R.; Romčević, M.; Čomor, M. I.; Nedeljković, J. M. *J. Phys. D: Appl. Phys.* **2005,** *38,* 4321–4324. doi:10.1088/0022-3727/38/24/009
22. Kostić, R.; Romčević, N. *Phys. Status Solidi C* **2004,** *1,* 2646–2649. doi:10.1002/pssc.200405349
23. Scamarcio, G.; Lugará, M.; Manno, D. *Phys. Rev. B* **1992,** *45,* 13792–13795. doi:10.1103/PhysRevB.45.13792
24. Hwang, Y.-N.; Shin, S.; Park, H. L.; Park, S.-H.; Kim, U.; Jeong, H. S.; Shin, E.-J.; Kim, D. *Phys. Rev. B* **1996,** *54,* 15120–15124. doi:10.1103/PhysRevB.54.15120
25. Brus, L. *J. Phys. Chem.* **1986,** *90,* 2555–2560. doi:10.1021/j100403a003

License and Terms

The definitive version of this article is the electronic one which can be found at:
doi:10.3762/bjnano.4.27

Beilstein Journal of Nanotechnology

Molecular dynamics simulations of mechanical failure in polymorphic arrangements of amyloid fibrils containing structural defects

Hlengisizwe Ndlovu[1,2], Alison E. Ashcroft[2,3], Sheena E. Radford[2,3] and Sarah A. Harris[*1,2]

Full Research Paper

Open Access

Address:
[1]School of Physics and Astronomy, University of Leeds, Leeds LS2 9JT, UK, [2]Astbury Centre for Structural Molecular Biology, University of Leeds, Leeds, LS2 9JT, UK and [3]School of Molecular and Cellular Biology, University of Leeds, Leeds LS2 9JT, UK

Email:
Sarah A. Harris* - s.a.harris@leeds.ac.uk

* Corresponding author

Keywords:
amyloid; fibril fragmentation; steered molecular dynamics (SMD); structural defects

Beilstein J. Nanotechnol. **2013,** *4,* 429–440.
doi:10.3762/bjnano.4.50

Received: 01 December 2012
Accepted: 24 June 2013
Published: 04 July 2013

This article is part of the Thematic Series "High-resolution electrical and chemical characterization of nm-scale organic and inorganic devices".

Guest Editors: E. Meyer and P. Eyben

Abstract

We examine how the different steric packing arrangements found in amyloid fibril polymorphs can modulate their mechanical properties using steered molecular dynamics simulations. Our calculations demonstrate that for fibrils containing structural defects, their ability to resist force in a particular direction can be dominated by both the number and molecular details of the defects that are present. The simulations thereby suggest a hierarchy of factors that govern the mechanical resilience of fibrils, and illustrate the general principles that must be considered when quantifying the mechanical properties of amyloid fibres containing defects.

Introduction

Amyloid fibrils are biomaterials that are commonly associated with human disease [1]. Over recent years, however, properties such as self-assembly and robustness have increasingly made them attractive candidates for use in nanotechnological applications [2,3] that range from conducting nanowires [4], to drug-delivery devices [5], structural scaffolds [6,7] and functionalised hydrogels [8]. A central theme in each of these distinct potential applications is an ability to control and modulate a desired property of the fibril aggregates. The requirements for the mechanical robustness of ideal, long, conducting nanowires, for instance, is that they not be prone to fragmentation, whereas a drug-delivery device needs to be sufficiently robust to carry its cargo to the target site, but then be able to release it in response to an external signal. The ability to control the length of fibrils by using simple changes in growth and storage conditions has been successfully demonstrated for bovine insulin

fibrils [9]. Before we can design fibrils with bespoke material properties, however, we first need to understand how the arrangement of the individual β-sheets modulates their mechanical behaviour.

Amyloid fibrils, like many crystalline materials, exhibit polymorphism. The predominant polymorph obtained by protein or peptide self-assembly depends on the environmental growth conditions such as pH, temperature, salt concentration and mechanical agitation [10]. Since amyloid polymorphs have been observed with drastically different morphologies [11] and chemical properties [12], it is important to develop an understanding of how the polymorphic form influences the mechanical properties of fibrils. A wealth of information on the material properties of amyloid is already available from extensive pathological and biological studies that focus on the diseases aspect of amyloid, as summarised in a recent review [13]. The mechanical properties of amyloid materials have also been characterised through various biophysical techniques [14]. These include the use of atomic force microscopy (AFM), and in particular, AFM nanoindentation methods to deduce the elastic properties of amyloid [15-19]. Computer simulations that characterise the mechanical properties of amyloid fibrils have proved useful in both verifying and expanding on the experimental work. Such computational studies have for instance, reported elastic properties of Aβ fibrils comparable to experimental values [20], investigated fibril failure under tensile loading [21], revealed that geometrical confinement of β-sheets in spider silk leads to mechanical enhancement [22], and highlighted the role played by the peptide sequence on the mechanical resistance of amylin-derived fibrils [23].

In this work, three polymorphs of fibrils formed from 10-residue fragments of the amylin protein (sequence SNNFGAILSS) as structurally determined by ssNMR [24] are simulated in full atomistic detail using molecular dynamics (MD). These models are classified according to symmetry packing classes, after the Eisenberg steric zipper nomenclature [25,26], as Class 1 (parallel both within each β-sheet and between the pair of stacked sheets), Class 2 (parallel within each β-sheet but antiparallel between stacked β-sheets) and Class 6 (antiparallel β-sheets stacked in a parallel orientation), as shown in Figure 1. The SNNFGAILSS sequence is particularly interesting in that both parallel and antiparallel polymorphs are simultaneously observed under identical growth conditions [24]. Moreover, a separate ssNMR study only observed a single fibril type in the antiparallel configuration, possibly due to the use of different terminal capping groups [27]. Consequently, the differences in

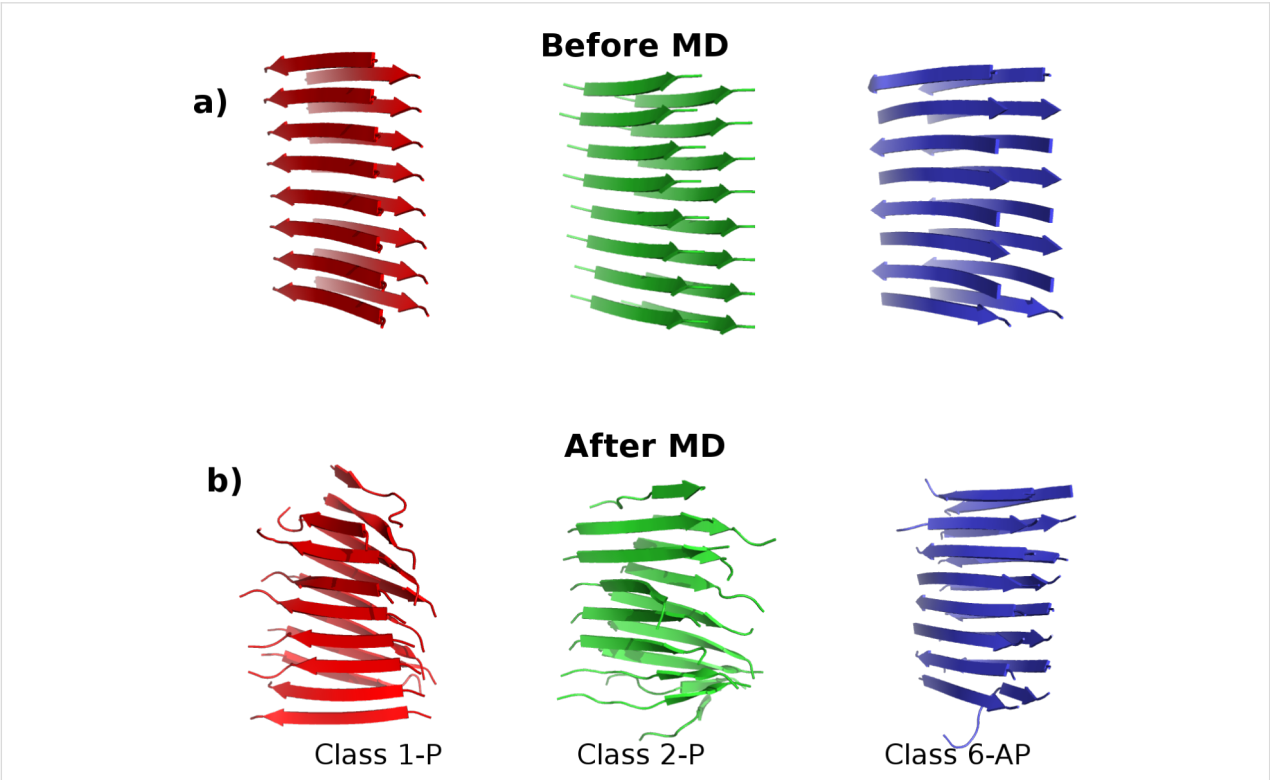

Figure 1: The three polymorphs of SNNFGAILSS sequence fibrils in the Class1-P (red), Class2-P (green) and Class6-AP (blue) symmetry-packing classes. (a) Models before the molecular dynamics simulation; (b) the structural changes in each model at the conclusion of 20 ns of MD in explicit solvent (water molecules omitted for clarity).

energetic and mechanical stability between polymorphs of SNNFGAILSS present a unique system to study the relevant interactions that play key roles in determining their observed properties.

We have used steered molecular dynamics (SMD) simulations to probe how the packing and steric arrangements found in the three different polymorph symmetry classes influence fibril mechanical behaviour. The fibrils are probed from different directions, using distinct pulling geometries that we developed previously to study the role of the peptide sequence in modulating amyloid mechanical properties [23]. The SMD pulling geometries are designed to disrupt the stabilising hydrophobic core and backbone hydrogen bond networks from a variety of directions. We then assess how the mechanical response in the simulations is affected by doubling the length of the model fibrils, and how the mechanical properties are modulated by incorporating chemical capping groups to neutralise the N- and C-termini of the peptides. In a previous simulation study to determine the sequence dependence of the resistance of amyloid fibrils to mechanical stress by using SMD [23], we highlighted the importance of structural defects within the model fibrils in determining their mechanical properties. Similarly, in this paper we pay particular attention to the role played by structural defects in the ability of the three different polymorphs of the 10-residue amylin fragment to resist an applied force. The calculations reveal a hierarchy of factors that govern the mechanical resilience of defect-containing fibrils subjected to forces applied in silico.

Results and Discussion

To characterise the mechanical response of the fibril polymorphs, following 20 ns of standard MD to equilibrate the fibrils models, SMD simulations were carried out using the pulling geometries shown schematically in Figure 2 to probe the fibrils from different directions. Each pulling-mode simulation was repeated four times, and the mechanical properties were characterised by the average peak force measured over the four independent simulations. The nomenclature adopted throughout is Class1-P (parallel β-sheets), Class2-P (parallel β-sheets) and Class6-AP (antiparallel β-sheets).

Mechanical responses of 8 × 2 fibril models

We first model the fibril polymorphs as two interfaced β-sheets, each of which comprises eight peptides (8 × 2 models), as shown in Figure 1. Figure 3a shows that all of the models contain some degree of structural disorder after the 20 ns of standard MD (used to equilibrate the fibrils prior to SMD), with the most ordered structure (Class6-AP) containing 80% β-sheet content, and the most disordered (Class2-P) containing only 58%. We subjected each of the three polymorphs to the four pulling modes in Figure 2, and recorded the peak forces exerted (as shown in Figure 4). Force profiles from which the highest peak forces are measured for each polymorph during the four different SMD pulling modes are shown in Figure 5. All three fibril polymorphs demonstrate an anisotropic response to mechanical probing. Similar mean peak forces are required to break the fibrils when the hydrogen-bond networks are probed ("shear" and "stretch"). There are however, very distinct

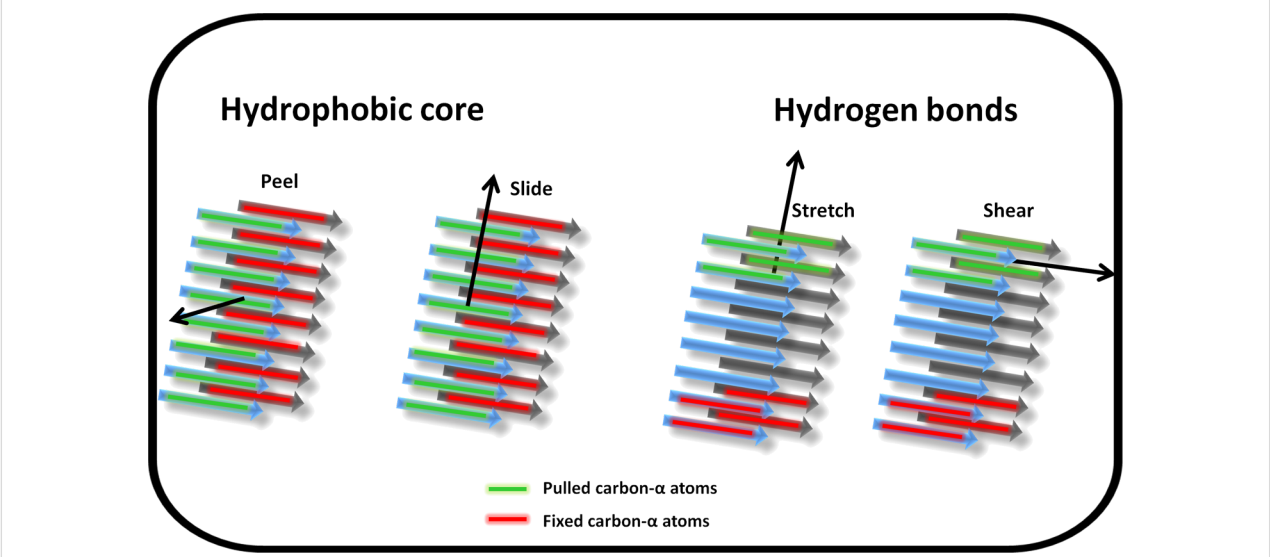

Figure 2: Schematic representation of the four pulling geometries used to mechanically probe the fibril models. The centre of mass of the carbon-α atoms in the peptide marked in green are pulled in the direction shown by the arrow at a constant velocity whilst the carbon-α atoms in the peptide marked in red are fixed for the duration of the simulation. All other atom types are free to move unrestrained. "Peel" and "slide" simulations probe the hydrophobic core interactions while "stretch" and "shear" interrogate the hydrogen bond networks parallel and perpendicular to the fibril long axis respectively.

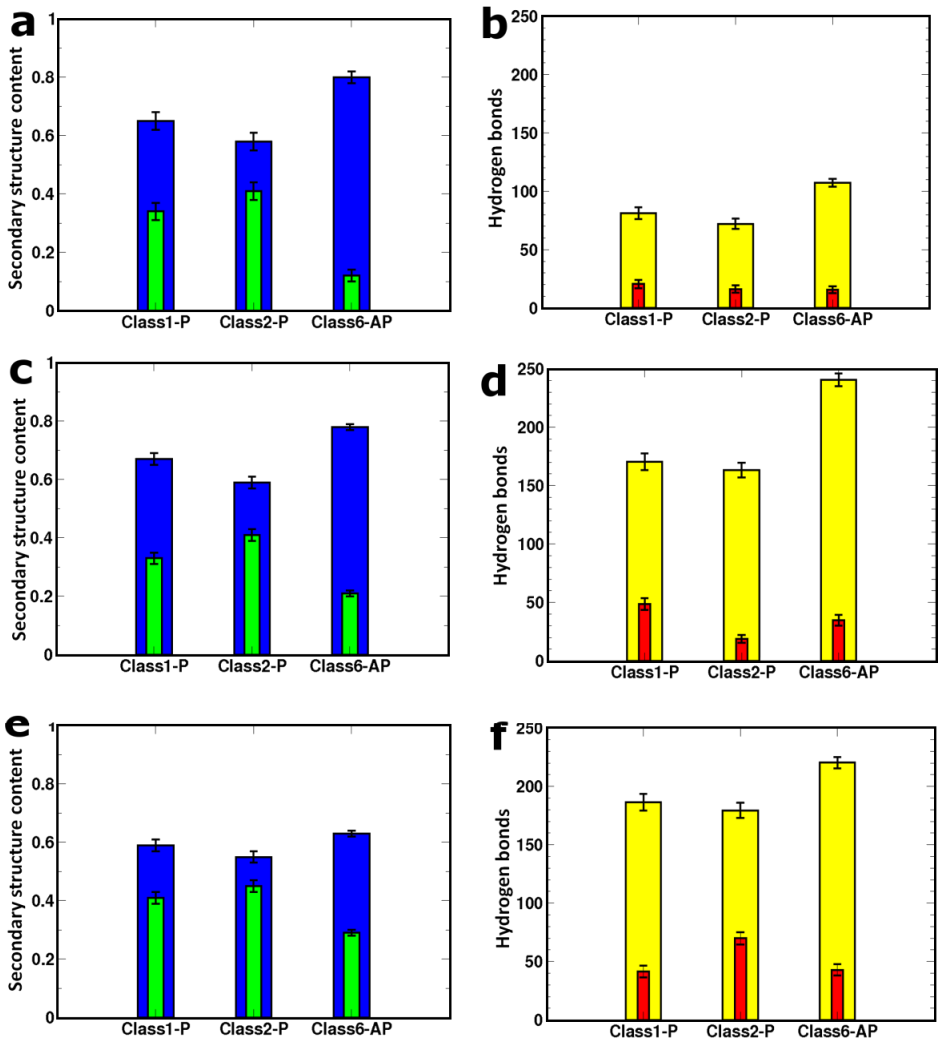

Figure 3: Left and right columns show the mean fraction of secondary structure content and hydrogen-bond numbers, respectively. The details for the 8 × 2 fibril models are in panels (a) and (b). On the left, blue bars show β-strand content and green bars show random coil conformations. On the right, the mean number of interstrand backbone (yellow) and side-chain (red) hydrogen bonds are shown. Panels (c) and (d) relate to the free-terminal-ended 16 × 2 models while panels (e) and (f) are for the capped 16 × 2 fibrils. The secondary structure content and hydrogen-bond analysis is computed from the final 10 ns of MD.

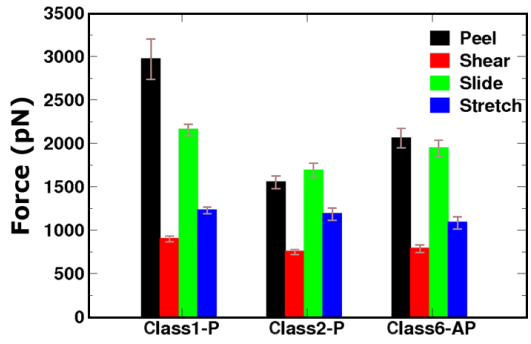

Figure 4: Mean peak force for the three fibril polymorphs (8 × 2 models) obtained from four repeat simulations of each pulling mode with error bars showing the standard error in the mean.

responses in the SMD simulations that probe the hydrophobic core interactions (“peel” and “slide”).

Hydrophobic core disruption: The largest mean peak forces for both hydrophobic core probing modes (“peel” and “slide”) were recorded for the Class1-P polymorph. The molecular basis behind the relative ranking in mean peak force between the polymorphs can be understood by examining the intersheet interfaces that are affected during the SMD simulation. Both “slide” and “peel” modes disrupt the electrostatic interactions between the charged termini and force the hydrophobic core to be exposed to solvent molecules. For the three polymorphs containing eight peptides in each of the two stacked β-sheets, we observe a correlation between the mean peak force and the

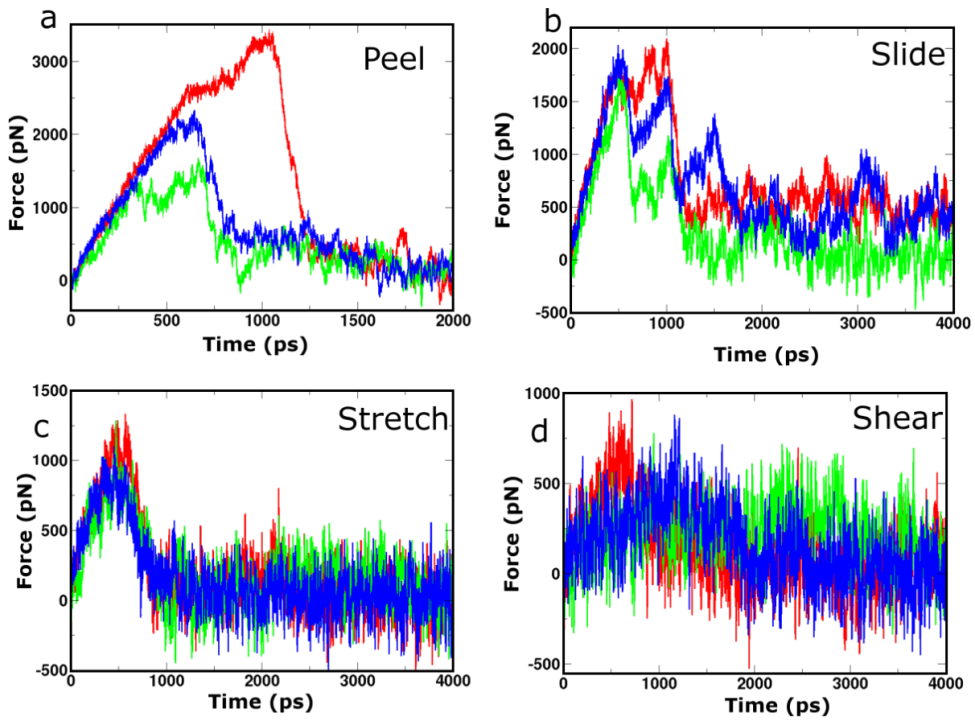

Figure 5: Selected force profiles recorded during SMD simulations for the class 1-P (red), class 2-P (green) and class 6-AP (blue) 8 × 2 fibril polymorphs. Panels (a), (b), (c) and (d) show the profiles from which the highest peak force was measured for each polymorph during probing by "peel", "slide", "stretch" and "shear" SMD pulling modes, respectively.

intersheet electrostatic interaction energies (Table 1) that arise due to the unique packing arrangements of the monomer β-strands. The Class1-P polymorph has the most favourable electrostatic energy between the stacked β-sheets because these are arranged in an antiparallel configuration, which brings the oppositely charged C- and N-termini close together. However, since Class2-P is in a parallel arrangement both within an individual β-sheet and within the stacked pair, this polymorph has the least favourable electrostatic interaction between the sheets of the three. The fact that the Class 6 polymorph is comprised of antiparallel β-sheets stacked in a parallel configuration places it intermediate between the other two. The correlation between the peak force and the electrostatic interfacial energy demonstrates how the details imposed by polymorphic arrangements of the peptides in the fibril can determine the mechanical characteristics when a force is applied in a particular direction.

Hydrogen-bond-network response: In the two pulling geometries ("shear" and "stretch") that primarily interrogate the hydrogen-bond networks, similar mean peak forces were recorded for all three polymorphs. The stretch and shear simulations probe the interpeptide hydrogen networks in directions parallel and perpendicular to the fibril axis respectively. Figure 4 shows that pulling parallel to the hydrogen bond network results in higher peak forces than when pulling across it. This implies that the hydrogen-bond network provides a cooperative resistance to the forces applied in the direction of the long axis. A surprising aspect of these simulations is that the

Table 1: Thermodynamic properties of 8 × 2 fibrils.[a]

Model	$\Delta G_{electro}$ [kcal/mol]	ΔG_{solv} [kcal/mol]	ΔG_{vdw} [kcal/mol]	$\Delta G_{Binding}$ [kcal/mol]
Class 1-P	−2457.79 ± 4.17	2466.82 ± 4.01	−152.46 ± 0.31	−143.43 ± 0.62
Class 2-P	938.98 ± 1.79	−849.46 ± 1.66	−198.60 ± 0.46	−109.08 ± 0.45
Class 6-AP	−254.94 ± 1.05	359.97 ± 0.84	−257.77 ± 0.40	−152.74 ± 0.52

[a]The interactions of the interface between the pair of β-sheets are decomposed into electrostatic ($\Delta G_{electro}$), solvation (ΔG_{solv}) and van der Waals (ΔG_{vdw}) energy terms, which all contribute to the binding free energy ($\Delta G_{Binding}$). Analysis is from 1 ps snapshots of the final 10 ns of unrestrained MD as calculated by the MM-PBSA method. The mean energies are expressed in units of kcal/mol, with the standard error in the mean.

polymorphs record virtually identical mean peak forces when subjected to "stretch", in spite of the fact that they contain different numbers of hydrogen bonds (Figure 3b). Moreover, a systematic simulation study of the relationship between thermodynamic stability and the symmetry class of fibrils has shown that in (non-Q/N)-rich sequences, the antiparallel fibrils tend to be more energetically stable than their parallel counterparts [28], which would suggest that the Class6-AP polymorph should exhibit the most resilience to stretching forces. However, prior to SMD, the Class1-P, Class2-P, and Class6-AP structures consist of 34%, 41% and 12% random coil conformations, respectively (Figure 3a), indicating that defects are present in all fibril models. These defects can dominate the mechanical response of the fibrils in a particular pulling direction by providing weak points that are liable to fracture, as we have previously described [23].

Mechanical response of 16 × 2 fibril models

Having demonstrated that pulling along the long axis of the fibril by the stretch deformation mode is sensitive to the presence of structural defects within the fibrils, we then examined how the peak force changes when the fibril doubles in length from eight peptides in each of the stacked β-sheets (8 × 2 peptide arrangement) to 16 (16 × 2 fibril model), since there is a greater probability that structural defects will be present in longer fibrils. The influence of fibril length on mechanical properties has already been demonstrated by using a normal mode analysis in conjunction with a coarse-grained elastic-network model based on SNNFGAILSS fibrils [29], which showed that the bending rigidity increases up to a critical length; however, it is not possible to assess the importance of defects within such a coarse-grained model. For direct comparison between the different fibril lengths, the mean peak force during SMD was normalised to the number of interfaces probed. Figure 6b shows that all three fibril models register an increase in the mean peak force per interface upon elongation. This indicates that the increase in the total number of hydrogen bonds between the fixed and pulled ends of the fibrils results in higher peak forces being required to induce mechanical failure. This implies that there is a degree of cooperativity in the resilience of these short fibres, which arises from the increased length of the hydrogen-bonding network along the long axis of the model fibrils. However, the relative gains in the mechanical resistance appear to be unique to each polymorphic model. Doubling the length for Class1-P and Class6-AP models leads to an increase in the mean peak force per interface of 35% and 46%, respectively, whilst for Class2-P the increase is marginal at 9%. The ranking of peak force per interface amongst the polymorphs is reflected

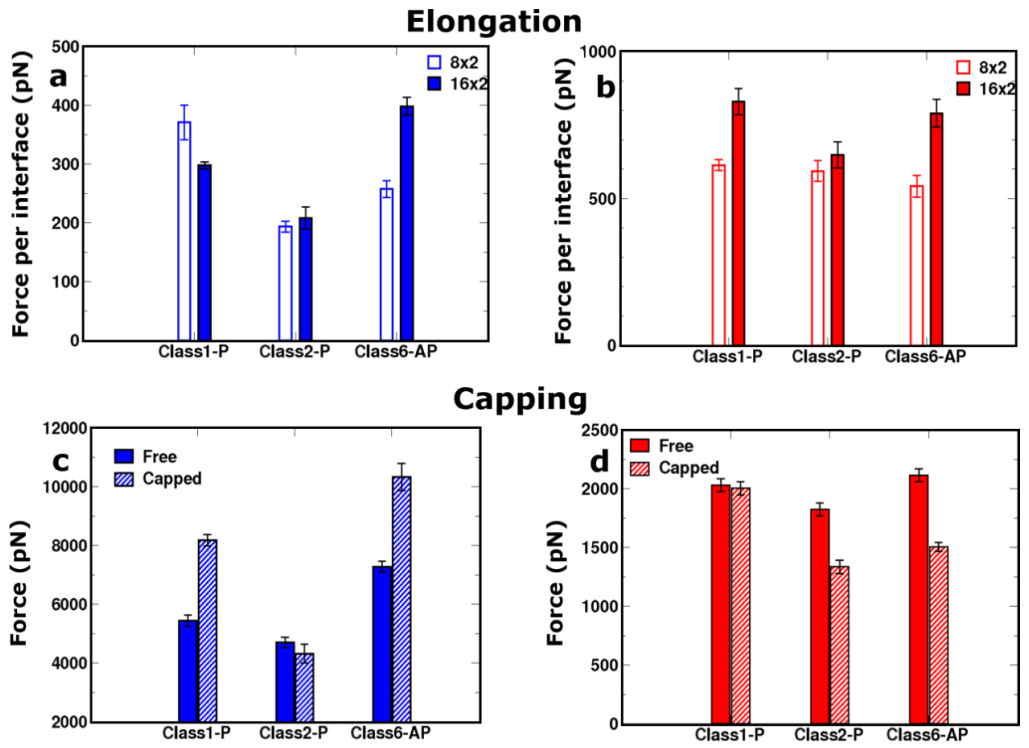

Figure 6: Elongation: The comparative response of the 16 × 2 (filled bar) and the 8 × 2 (empty bar) sized fibril models for the (a) "peel" and (b) "stretch" pulling directions. In both cases, the mean peak force is normalised by the number of interfaces interrogated during the simulation. **Capping:** The comparative response of uncapped (filled bar) and capped (striped bar) for the (c) "peel" and (d) "stretch" directions.

in the total number of backbone and side-chain hydrogen bonds present in each model (Figure 3d).

We also investigated the dependence of the mechanical response to the "peel" deformation, which interrogates the strength of the hydrophobic interface between the pair of stacked β-sheets along the long axis of the fibril (Figure 6a). In contrast to the shorter (8 × 2) aggregates, applying peel SMD to the 16 × 2 fibrils results in a fragmentation of only a small fraction of the hydrophobic surface (Figure 7). Consequently it was not possible to relate the peak force measured to the thermodynamic stability of the hydrophobic interface, because it is not completely disrupted during the deformation. We conclude that to understand the mechanical robustness of fibrils, it is necessary to have information about the structure of the fragments that result, as well as the structure of the unperturbed fibrils themselves.

Mechanical modulation of 16 × 2 fibril models by N- and C-terminal capping

We also explored how the mechanical properties of the polymorphs are affected by the addition of terminal capping groups at both ends of each peptide strand (N-terminal acetylation and C-terminal amidation), which neutralises the charged groups at both ends of the peptide monomers. The mean peak forces for fibrils of length 16 × 2 were compared for capped and uncapped models using the "peel" and "stretch" SMD modes (Figure 6c and Figure 6d). In the "peel" pulling geometry, which gives rise to an incomplete separation of the hydrophobic interfaces for these longer fibrils, the fragmentation mechanisms between capped and uncapped models are distinct, as shown in Figure 8. Figure 8 shows a comparison of the evolution of the distances between peptide pairs on opposite β-sheets for the class1-P model during each set of repeat peel SMD simulations. The resistance mechanism for the charged-termini models shows that the separation of the peptide pairs occurs gradually, i.e., the fibrils have ductile characteristics. In stark contrast, the capped models undergo significant displacements over a very short period of time; consequently, they are more brittle than the capped counterparts. We hypothesise that this is due to the modification of the electrostatics by the addition of capping groups. In the capped case, these fibrils break suddenly because the interactions stabilising the fibrils (hydrogen bonding and hydrophobic forces) are short-ranged in comparison to the long-range electrostatic interactions within the uncapped fibrils. This highlights how a relatively simple modification at the terminus end can have a significant impact on the mechanical character of amyloid fibrils formed from short peptide sequences.

The response of the capped and uncapped fibrils to SMD by the "stretch" SMD pulling mode was determined by both the

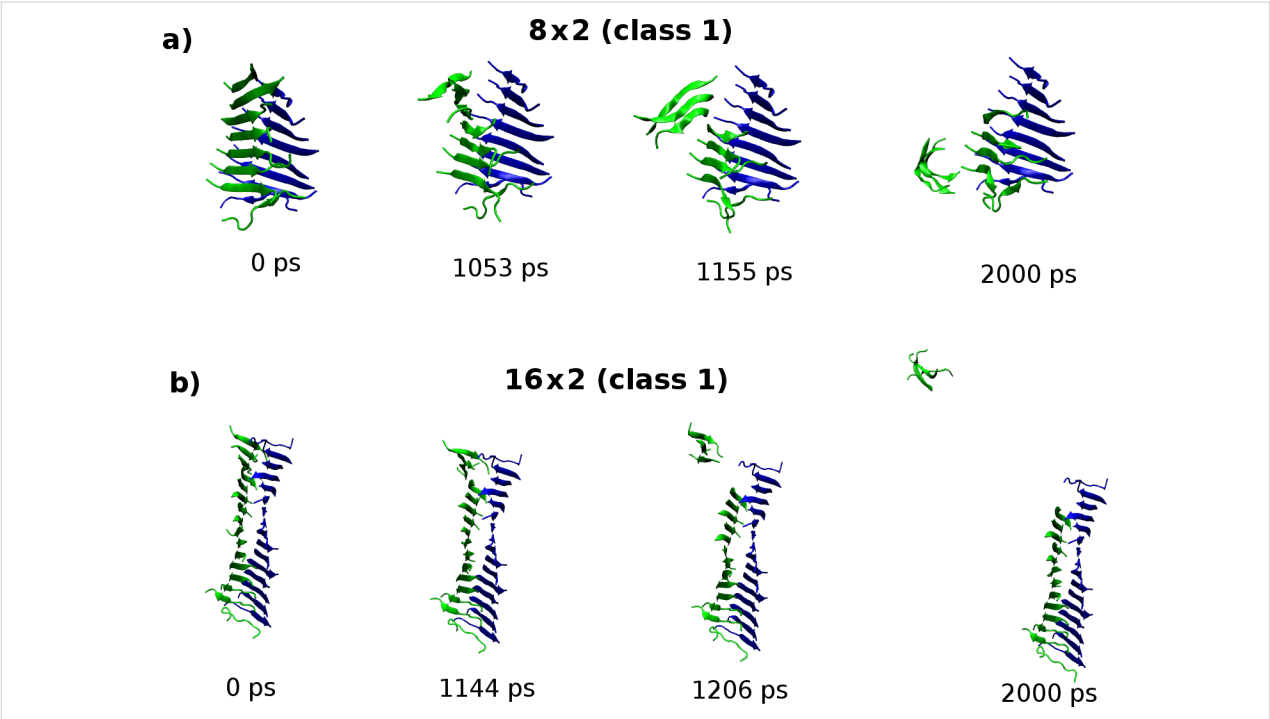

Figure 7: Molecular configurations sampled from the "peel" SMD trajectory for the (a) 8 × 2 and (b) 16 × 2 fibril models of the class1-P polymorph. The carbon-α atoms in the peptides coloured green are pulled while carbon-α atoms in peptides shown in blue are fixed. In contrast to the 8 × 2 fibrils, the response of the 16 × 2 fibrils leads to an exposure of only a small fraction of the hydrophobic surface.

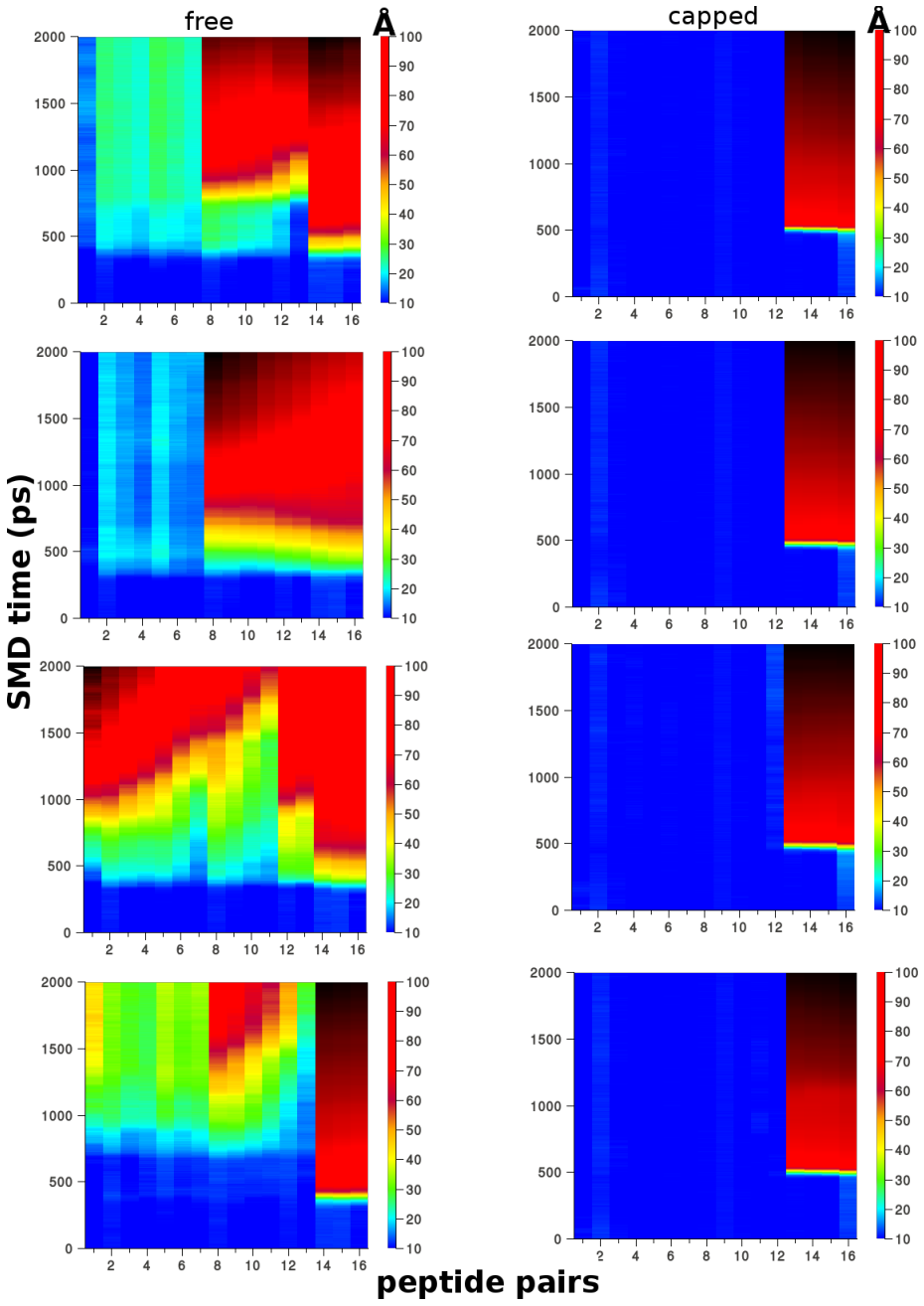

Figure 8: Plots showing the displacement between peptide pairs on opposite β-sheets during the "peel" SMD for the Class1-P polymorph model. The free (left) and capped terminal (right) models are each compared from four independent simulations. The colour scale is the centre-of-mass distance between pairs in angstroms (Å), the *x*-axis is the pair number (total of 16), and the *y*-axis is time in picoseconds.

number and the nature of the defects present in the fibril models. Although both the Class1-P and Class2-P polymorphs show an increase in the number of hydrogen bonds when the termini are capped, the number of ordered β-sheet secondary structures is reduced, indicating an increased number of defects within the aggregates. Consequently, the mean peak force per interface required to break the fibrils is reduced or remains the same when the termini are capped. The behaviour of the Class6-AP polymorph, which shows a large reduction in the mean peak force for the capped fibrils, provides a particularly striking example of how the response of fibrils to an applied force can be dominated by the molecular details of the defects present. Figure 9 shows the starting configuration for the SMD simulations for the capped fibril model. This polymorph developed a

substantial crack defect in the one of the paired β-sheets prior to SMD, which substantially reduced the ability of this fibril model to resist "stretch" relative to its uncapped counterpart.

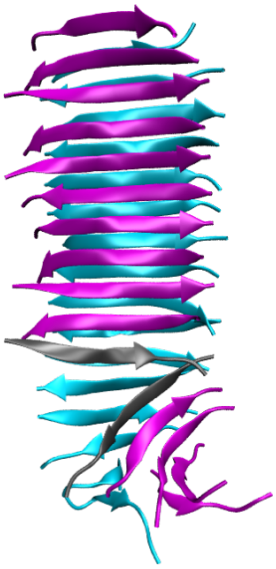

Figure 9: Molecular conformation of the capped Class6-AP fibril prior to SMD simulation. The misaligned peptide strands on the purple β-sheet, highlighted in grey, are significantly splayed and have reduced interpeptide hydrogen bonding. This structural defect site is the first point of failure leading to the reduced peak force for this fibril model.

Conclusion

We have performed a series of SMD simulations to mechanically probe three polymorphs of fibrils formed from the SNNFGAILSS peptide sequence. The results collectively demonstrate how the mechanical response of fibrils is directly related to the peptide packing arrangements and the number and nature of the defects present within the models. The small model fibrils investigated in this study are rich in structural defects, because they lack the stabilisation from crystal packing within a larger aggregate. Consequently, we have been able to characterise how the nature and presence of such defects influences their mechanical response. However, this precludes the investigation of effects such as crack propagation on the material properties of the model fibrils, because these occur over longer length scales. Our simulations suggest a hierarchy of factors that govern the mechanical resilience of fibrils subjected to stretching forces, which we list below in order of importance:

(1) If defects are present that are sufficiently severe that there is an absence of hydrogen-bonding interactions between one β-strand and the next within one of the paired β-sheets (e.g., the capped Class6-AP polymorph), then this defect will act as a weak point when a fibril is subjected to the "stretch" deformation, and it will rupture at lower forces than an equivalent fibril in which this defect is absent. This is illustrated by the behaviour of the capped Class6-AP polymorph, which disassociates at anomalously low forces given the number of hydrogen bonds it contains due to the presence of a crack defect in one of the paired β-sheets (as shown in Figure 9).

(2) If the fibril models contain disordered regions that have reduced hydrogen bonding interactions within a given β-sheet, but which nevertheless maintain a degree of interaction with consecutive monomers, then the fibril will be weaker when subjected to "stretch" than one with a perfectly ordered β-sheet structure. This is illustrated by the behaviour of all polymorphs subjected to the stretch deformation.

(3) If the fibrils contain a high degree of order at the interface being interrogated, and if the pulling mode applied results in a substantial separation of this interface, then the peak force required to cause mechanical failure of the fibril will be correlated with the interfacial energy. This is illustrated by the behaviour of the 8 × 2 polymorphs subjected to the "peel" deformation. We hypothesise that only for polymorphs containing a very high degree of ordered β-sheet secondary structure would the response of the fibrils to "stretch" be determined by the difference in hydrogen bonding between idealised parallel and antiparallel β-sheets.

Our simulations of amyloid polymorphs illustrate the general principles that must be considered when evaluating and comparing the mechanical properties of amyloid fibrils containing structural defects. While fibrils formed from an 11-residue fragment of transthyretin, full length and α-chain insulin fibrils and an 84-residue SH3 domain have been reported that contain extremely high degrees of structural order, with defects present in approximately one molecule in every 1000 along the fibril axis [30], experiments which have probed the mechanical properties of α-synuclein and full-length transthyretin under high-pressure conditions have shown that their robustness is indeed dominated by the presence of defects within the hydrophobic core [31]. From our understanding of the crystallisation of inorganic substances, such as minerals and ceramics, it is known that the number of defects will depend critically upon how these crystals were grown, including factors such as the rate of growth, the presence of surfaces or impurities, and whether the solution was agitated. If amyloid fibres with bespoke mechanical properties are to be used in nanotechnology, it will be necessary to assess the reproducibility of the experimental conditions used to produce the fibrils carefully, because small changes in the manufacturing could potentially alter the polymorphic form or the number density of defects present, and substantially affect mechanical robustness.

Moreover, recent combined experimental and simulation studies of pore formation in membranes (which is implicated in amyloid toxicity) by oligomeric aggregates of $A\beta_{9-42}$ have shown that the stress associated with tightly bending the fibrils to form a cylindrical channel induces large defects in previously homogeneous fibrils [32,33]. Consequently, the propensity of amyloid fibrils to form defects may also play a role in their cytotoxicity.

Experimental

Construction of polymorph models

The models of the parallel and antiparallel (Class1-P & Class6-AP) fibril structures were built from coordinate files determined from ssNMR [24]. The coordinate files initially consisted of a pair of β-sheets, each of which was composed of two peptides of the SNNFGAILSS sequence (2 × 2 models). These coordinates were used as templates from which longer fibrils were constructed. The Nucleic Acid Builder (NAB) software package [34] was used to make translated copies of the 2 × 2 model, which were then subsequently joined into single structures in the LEAP module of the Amber9 package [35]. The elongated copies maintained the intersheet and interpeptide separation distances found in the original ssNMR coordinates. The LEAP module also allowed for the automatic addition of hydrogen atoms (which are not resolved by ssNMR). Two fibrils sizes were constructed for each polymorph; namely a pair of β-sheets each containing eight peptides (8 × 2 model) and a pair of β-sheets each containing 16 peptides (16 × 2 model). Two versions of the 16 × 2 sized models were built with the terminal ends either free (zwitterionic form) or capped (N-terminal acetylation and C-terminal amidation). A third SNNFGAILSS model in the Class2-P symmetry configuration was also rationally designed with similar steps used to make length and capping modifications.

Molecular dynamics simulations

Molecular dynamics simulations were run using AMBER9 [35] and NAMD2.7b1 [36] simulation packages, with the all atom AMBER99SB [37] and the CHARMM22/CMAP [38] force fields used, respectively. All models were explicitly solvated in a periodic water-box of TIP3 molecules [39] with periodic boundary conditions applied in all three directions. As the peptide sequence carried no net charge, neutralisation with counter-ions was not necessary. Long-range electrostatic interactions were calculated using the particle mesh Ewald (PME) method with a 9 Å cut-off. The models were then subjected to careful multistage equilibration with positional restraints on the solute allowing for gentle heating of each system from an initial temperature of 100 K to a target 300 K prior to MD. All bonds to hydrogen were constrained using the SHAKE algorithm allowing a 2 fs time step to be used during MD. Restraints on the hydrogen-bond distance of the interstrand backbone were then temporarily imposed for 1 ns prior to MD. All MD was run at constant temperature of 300 K using a Berendsen thermostat and constant pressure of 1 atm. The root mean square deviation (RMSD) of backbone carbon-α atoms was used to monitor convergence of the MD simulations. This was achieved within 20 and 40 ns for the 8 × 2 and 16 × 2 models, respectively.

Steered molecular dynamics simulation

The details of the SMD protocol used are identical to those we have described elsewhere [23]; only a summary is presented here. The final configurations of the fibril models at the end of the MD were used as the starting points for SMD simulations to characterize the mechanical properties of the polymorphs. Prior to the start of SMD, each model was resolvated in a larger periodic water box in order to allow extension under force without self-interactions. The NAMD2.7b1 [36] package and Charmm22-cmap force field [38] was used to perform the simulations. The fragmentation methodology schematically shown in Figure 2 was then applied to the fibril models, with each deformation type repeated four times. The fixed/pulled atom selections only apply to carbon-α atoms in the affected peptides, with all other atom types free to move. The simulations were carried out at constant temperature (300 K) and constant pressure (1 atm). Randomised starting velocities according to the Maxwell-Boltzmann distribution in each repeat simulation were used to ensure that the trajectories sampled different areas of phase space. The SMD simulations all used a spring constant of 500 pN/Å with a constant pulling velocity of 0.01 Å/ps unless otherwise stated. The duration of the SMD simulations were 4 ns for “stretch”, “slide” and “shear” geometries, and 2 ns for the “peel” mode. The capped models required the use of different simulation parameters for error-free completion in the time step and pulling velocity (0.5 fs and 0.04 Å/ps). Thus for cross comparability, a new set of “peel” and “stretch” simulations were also run for the uncapped models with these new SMD parameters.

Analysis methods and calculations

Secondary structure content, hydrogen bond and thermodynamic analysis of the production-phase MD simulations was performed on snapshots sampled every 1 ps from the final 10 ns of the converged trajectory. Secondary structure content was calculated with the DSSP method [40] through the PTRAJ module of AMBER 9 package [35]. The HBONDS utility in VMD [41] was used to analyse the occupancies of the backbone and side-chain interstrand hydrogen bonds. The MM-PBSA methodology as implemented in AMBER11 [35] was used to calculate the binding free energy of the intersheet interface and also the enthalpy of the fibril complex devoid of solvent molecules.

Acknowledgements

We thank David Middleton for the provision of coordinate files for the SNNFGAILSS fibril template. We thank the UK National Grid Service for contributing computational resources to the project. This work was funded by the EPSRC through the award of a doctoral training studentship to HN.

References

1. Chiti, F.; Dobson, C. M. *Annu. Rev. Biochem.* **2006,** *75,* 333–336. doi:10.1146/annurev.biochem.75.101304.123901
2. Cherny, I.; Gazit, E. *Angew. Chem., Int. Ed.* **2008,** *47,* 4062–4069. doi:10.1002/anie.200703133
3. Mankar, S.; Anoop, A.; Sen, S.; Maji, S. K. *Nano Rev.* **2011,** *2,* 6032. doi:10.3402/nano.v2i0.6032
4. Scheibel, T.; Parthasarathy, R.; Sawicki, G.; Lin, X.-M.; Jaeger, H.; Lindquist, S. L. *Proc. Natl. Acad. Sci. U. S. A.* **2003,** *100,* 4527–4532. doi:10.1073/pnas.0431081100
5. Maji, S. K.; Schubert, D.; Rivier, C.; Lee, S.; Rivier, J. E.; Riek, R. *PLoS Biol.* **2008,** *6,* e17. doi:10.1371/journal.pbio.0060017
6. Todd, C. H.; de Lacalle, S.; Su, X.; Liu, G.; Rich, A.; Zhang, S. *Proc. Natl. Acad. Sci. U. S. A.* **2000,** *97,* 6728–6733. doi:10.1073/pnas.97.12.6728
7. Horii, A.; Wang, X.; Gelain, F.; Zhang, S. *PLoS One* **2007,** *2,* e190. doi:10.1371/journal.pone.0000190
8. Bhak, G.; Lee, S.; Park, J. W.; Cho, S.; Paik, S. R. *Biomaterials* **2010,** *31,* 5986–5995. doi:10.1016/j.biomaterials.2010.03.080
9. Domigan, L. J.; Healy, J. P.; Meade, S. J.; Blaikie, R. J.; Gerrard, J. A. *Biopolymers* **2011,** *97,* 123–133. doi:10.1002/bip.21709
10. Toyama, B. H.; Kelly, M. J. S.; Gross, J. D.; Weissman, J. S. *Nature* **2007,** *449,* 233–237. doi:10.1038/nature06108
11. Jiménez, J. L.; Nettleton, E. J.; Bouchard, M.; Robinson, C. V.; Dobson, C. M.; Saibil, H. R. *Proc. Natl. Acad. Sci. U. S. A.* **2002,** *99,* 9196–9201. doi:10.1073/pnas.142459399
12. Krishnan, R.; Lindquist, S. L. *Nature* **2005,** *435,* 765–772. doi:10.1038/nature03679
13. Eisenberg, D.; Jucker, M. *Cell* **2012,** *148,* 1188–1203. doi:10.1016/j.cell.2012.02.022
14. Knowles, T. P. J.; Buehler, M. J. *Nat. Nanotechnol.* **2011,** *6,* 469–479. doi:10.1038/nnano.2011.102
15. Guo, S.; Akhremitchev, B. B. *Biomacromolecules* **2006,** *7,* 1630–1636. doi:10.1021/bm0600724
16. del Mercarto, L. L.; Maruccio, G.; Pompa, P. P.; Bochicchio, B.; Tamburro, A. M.; Cingolani, R.; Rinaldi, R. *Biomacromolecules* **2008,** *9,* 796–803. doi:10.1021/bm7010104
17. Smith, J. F.; Knowles, T. P. J.; Dobson, C. M.; MacPhee, C. E.; Welland, M. E. *Proc. Natl. Acad. Sci. U. S. A.* **2006,** *43,* 15806–15811. doi:10.1073/pnas.0604035103
18. Kol, N.; Alder-Abramovich, L.; Barlam, D.; Shneck, R. Z.; Gazit, E.; Rousso, I. *Nano Lett.* **2005,** *5,* 1343–1346. doi:10.1021/nl0505896
19. Graveland-Bikker, J. F.; Schaap, I. A. T.; Schmidt, C. F.; de Kruif, C. G. *Nano Lett.* **2006,** *6,* 616–621. doi:10.1021/nl052205h
20. Paparcone, R.; Keten, S.; Buehler, M. J. *J. Biomech* **2010,** *43,* 1196–1201. doi:10.1016/j.jbiomech.2009.11.026
21. Paparcone, R.; Buehler, M. J. *Biomaterials* **2011,** *32,* 3367–3374. doi:10.1016/j.biomaterials.2010.11.066
22. Keten, S.; Xu, Z.; Ihle, B.; Buehler, M. J. *Nat. Mater.* **2010,** *9,* 359–367. doi:10.1038/nmat2704
23. Ndlovu, H.; Ashcroft, A. E.; Radford, S. E.; Harris, S. A. *Biophys. J.* **2012,** *102,* 587–596. doi:10.1016/j.bpj.2011.12.047
24. Madine, J.; Jack, E.; Stockley, P. G.; Radford, S. E.; Serpell, L. C.; Middleton, D. A. *J. Am. Chem. Soc.* **2008,** *130,* 14990–15001. doi:10.1021/ja802483d
25. Sawaya, M. R.; Sambashivan, S.; Nelson, R.; Ivanova, M. I.; Sievers, S. A.; Apostol, M. I.; Thompson, M. J.; Balbirnie, M.; Wiltzius, J. J. W.; McFarlane, H. T.; Madsen, A. Ø.; Riekel, C.; Eisenberg, D. *Nature* **2007,** *447,* 453–457. doi:10.1038/nature05695
26. Nelson, R.; Sawaya, M. R.; Balbirnie, M.; Madsen, A. Ø.; Riekel, C.; Grothe, R.; Eisenberg, D. *Nature* **2005,** *435,* 773–778. doi:10.1038/nature03680
27. Nielsen, J. T.; Bjerring, M.; Jeppesen, M. D.; Pedersen, R. O.; Pedersen, J. M.; Hein, K. L.; Vosegaard, T.; Skrydstrup, T.; Otzen, D. E.; Nielsen, N. C. *Angew. Chem., Int. Ed.* **2009,** *48,* 2118–2121. doi:10.1002/anie.200804198
28. Berryman, J. T.; Radford, S. E.; Harris, S. A. *Biophys. J.* **2011,** *100,* 2234–2242. doi:10.1016/j.bpj.2011.02.060
29. Yoon, G.; Kwak, J.; Kim, J. I.; Na, S.; Eom, K. *Adv. Funct. Mater.* **2011,** *21,* 3454–3463. doi:10.1002/adfm.201002493
30. Knowles, T. P. J.; Smith, J. F.; Devlin, G. L.; Dobson, C. M.; Welland, M. E. *Nanotechnology* **2007,** *18,* 044031. doi:10.1088/0957-4484/18/4/044031
31. Foguel, D.; Suarez, M. C.; Ferrão-Gonzales, A. D.; Porto, T. C. R.; Palmieri, L.; Einsiedler, C. M.; Andrade, L. R.; Lashuel, H. A.; Lansbury, P. T.; Kelly, J. W.; Silva, J. L. *Proc. Natl. Acad. Sci. U. S. A.* **2003,** *100,* 9831–9836. doi:10.1073/pnas.1734009100
32. Jang, H.; Arce, F. T.; Capone, R.; Ramachandran, S.; Lal, R.; Nussinov, R. *Biophys. J.* **2009,** *97,* 3029–3037. doi:10.1016/j.bpj.2009.09.014
33. Connelly, L.; Jang, H.; Arce, F. T.; Capone, R.; Kotler, S. A.; Ramachandran, S.; Kagan, B. L.; Nussinov, R.; Lal, R. *J. Phys. Chem. B* **2012,** *116,* 1728–1735. doi:10.1021/jp2108126
34. Macke, T.; Case, D. A. Modeling unusual nucleic acid structures. In *Molecular Modeling of Nucleic Acids;* Leontes, N. B.; SantaLucia, J., Jr., Eds.; American Chemical Society: Washington, DC, 1998; pp 379–393.
35. Case, D. A.; Cheatham, T. E., III; Darden, T.; Gohlke, H.; Luo, R.; Merz, K. M., Jr.; Onufriev, A.; Simmerling, C.; Wang, B.; Woods, R. J. *J. Comput. Chem.* **2005,** *26,* 1668–1688. doi:10.1002/jcc.20290
36. Phillips, J. C.; Braun, R.; Wang, W.; Gumbart, J.; Tajkhorshid, E.; Villa, E.; Chipot, C.; Skeel, R. D.; Kalé, L.; Schulten, K. *J. Comput. Chem.* **2005,** *26,* 1781–1802. doi:10.1002/jcc.20289
37. Hornak, V.; Abel, R.; Okur, A.; Strockbine, B.; Roitberg, A.; Simmerling, C. *Proteins: Struct., Funct., Bioinf.* **2006,** *65,* 712–725. doi:10.1002/prot.21123
38. MacKerell, A. D., Jr.; Bashford, D.; Bellott, M.; Dunbrack, R. L., Jr.; Evanseck, J. D.; Field, M. J.; Fischer, S.; Gao, J.; Guo, H.; Ha, S.; Joseph-McCarthy, D.; Kuchnir, L.; Kuczera, K.; Lau, F. T. K.; Mattos, C.; Michnick, S.; Ngo, T.; Nguyen, D. T.; Prodhom, B.; Reiher, W. E., III; Roux, B.; Schlenkrich, M.; Smith, J. C.; Stote, R.; Straub, J.; Watanabe, M.; Wiórkiewicz-Kuczera, J.; Yin, D.; Karplus, M. *J. Phys. Chem. B* **1998,** *102,* 3586–3616. doi:10.1021/jp973084f
39. Jorgensen, W. L.; Chandrasekhar, J.; Madura, J. D.; Impey, R. W.; Klein, M. L. *J. Chem. Phys.* **1983,** *79,* 926–935. doi:10.1063/1.445869
40. Kabsch, W.; Sander, C. *Biopolymers* **1983,** *22,* 2577–2637. doi:10.1002/bip.360221211
41. Humphrey, W.; Dalke, A.; Schulten, K. *J. Mol. Graphics* **1996,** *14,* 33–38. doi:10.1016/0263-7855(96)00018-5

Beilstein Journal of Nanotechnology

Characterization of electroforming-free titanium dioxide memristors

John Paul Strachan[1], J. Joshua Yang[1], L. A. Montoro[2,3], C. A. Ospina[2], A. J. Ramirez[*2], A. L. D. Kilcoyne[4], Gilberto Medeiros-Ribeiro[1,3] and R. Stanley Williams[*1]

Full Research Paper

Open Access

Address:
[1]nanoElectronics Research Group, HP Labs, 1501 Page Mill Rd, Palo Alto, CA 94304, USA, [2]Brazilian Nanotechnology National Laboratory, CP 6192, Campinas, SP 13083-970, Brazil, [3]Universidade Federal de Minas Gerais, 31270-901, Belo Horizonte, MG, Brazil and [4]Advanced Light Source, Lawrence Berkeley National Laboratory, Berkeley, CA 94720, USA

Email:
A. J. Ramirez[*] - antonio.ramirez@lnnano.cnpem.br;
R. Stanley Williams[*] - stan.williams@hp.com

* Corresponding author

Keywords:
electron microscopy; memristor; resistance switching; transition-metal oxide; X-ray spectroscopy

Beilstein J. Nanotechnol. **2013,** *4,* 467–473.
doi:10.3762/bjnano.4.55

Received: 26 April 2013
Accepted: 20 July 2013
Published: 07 August 2013

This article is part of the Thematic Series "High-resolution electrical and chemical characterization of nm-scale organic and inorganic devices".

Guest Editors: E. Meyer and P. Eyben

Abstract

Metal–insulator–metal (MIM) structures based on titanium dioxide have demonstrated reversible and non-volatile resistance-switching behavior and have been identified with the concept of the memristor. Microphysical studies suggest that the development of sub-oxide phases in the material drives the resistance changes. The creation of these phases, however, has a number of negative effects such as requiring an elevated voltage, increasing the device-to-device variability, damaging the electrodes due to oxygen evolution, and ultimately limiting the device lifetime. In this work we show that the deliberate inclusion of a sub-oxide layer in the MIM structure maintains the favorable switching properties of the device, while eliminating many of the negative effects. Electrical and microphysical characterization of the resulting structures was performed, utilizing X-ray and electron spectroscopy and microscopy. In contrast to structures which are not engineered with a sub-oxide layer, we observed dramatically reduced microphysical changes after electrical operation.

Introduction

A memristor is a passive electronic element that displays a pinched hysteresis loop in its current–voltage characteristic, including the resistance switching that is seen in metal–insulator–metal (MIM) devices, often called resistive random access memory (RRAM or ReRAM). The memristor concept was developed by Chua [1,2], and much later associated with the

behaviors seen in a range of nanoscale devices [3,4]. In turn, the research effort to understand and develop oxide-based resistance switching devices for non-volatile memory applications has an even longer history [5-15] and remains active today. An important topic that has remained a challenge is understanding the microphysical changes [16,17] during electrical operation (forming and switching). Fortunately, physical characterization efforts with the required spatial resolution and material sensitivity are beginning to shed light on the material changes that take place in material systems such as the titanates, NiO, and HfO_2 [18-24].

Recently, physical characterization of Pt/TiO_2/Pt unipolar [25] and bipolar [26] resistance-switching devices by TEM and X-ray absorption revealed that the switching involves the creation of localized channels of Ti_4O_7 within the matrix material. The Ti_4O_7 channel, which can be considered an ordered array of oxygen vacancies in a TiO_2 rutile phase, is a thermodynamically stable and metallic (at room temperature) Magnéli phase. In the unipolar switching mode [25], this conductive channel is created and destroyed during ON and OFF switching, respectively, and spans the device structure between the top and bottom electrodes. In bipolar devices [26], this conductive phase is developed during the electroforming step [27,28] and ON and OFF switching does not appear to substantially modify this phase, but instead seems to modulate a thinner insulating barrier between the channel and a metal contact [29,30]. Indeed, the generation of the Ti_4O_7 Magnéli phase from TiO_2 can require significant power dissipation, lead to material damage to the device as oxygen gas evolves, and, in the case of bipolar devices, require an initial irreversible "electroforming" step to enable the subsequent reversible resistance switching to be possible. This electroforming step requires a large voltage and leads to variance from device to device. In addition, the high probability of electroforming failure results in a low switchable device yield [27]. Thus, it has been highly desirable from a technological standpoint to eliminate this step. Scientifically, it is also interesting to learn whether the formation of both a suboxide and an ordered phase, as seen in the Magnéli phase observations, are necessary preconditions to allow resistance switching in the titanium oxide system. The above studies point strongly to the benefits of deliberate oxide-layer engineering in order to fabricate devices that are able to switch reversibly without the need to form a conductive phase through the bulk first. Earlier studies [27] by our team indeed demonstrated that using a switching layer which includes a highly non-stoichiometric TiO_{2-x} film in addition to a thin stoichiometric TiO_2 layer can eliminate the need for an electroforming step while maintaining device performance. In the present work, we investigate the detailed material changes involved in such structures with X-ray spectromicroscopy and transmission electron microscopy (TEM), both techniques previously employed in observing the formation of a bulk conducting (Magnéli) phase. These techniques are applied to both the standard (electroformed) and non-stoichiometric (forming-free) devices in order to compare the material changes in each of them.

Sample preparation and resistance switching

MIM crossbar devices were fabricated on a silicon/silicon-nitride substrate. In some areas, the underlying Si was etched to form free-standing membranes allowing transmission characterization by X-ray absorption spectromicroscopy and electron microscopy. The bottom and top electrodes consisted of Cr(5 nm)/Pt(15 nm) and Pt(30 nm), respectively, patterned perpendicular to each other by photolithography. In between these electrodes, a blanket switching layer was deposited with two different compositions. For standard devices, an amorphous single layer TiO_2 (30 nm) was sputter-deposited from a titania source. For electroforming-free devices (described below), a bilayer was used consisting of TiO_{2-x} (30 nm) and TiO_2 (5 nm), where the thicker oxygen deficient layer was sputter deposited from a Ti_4O_7 Magnéli phase target and the thinner stoichiometric layer was again deposited from a stoichiometric titania target. Device junction areas studied included 1.5×1.5 μm^2 and 3×3 μm^2. The device area is defined by the overlap of the bottom and top electrode. X-ray diffraction (XRD) and selected area electron diffraction (SAED) showed that the stoichiometric TiO_2 film is predominantly amorphous with some small (<10 nm) anatase grains, while the bilayer film is amorphous with no observed structural ordering.

Electrical measurements of both types of devices are shown in Figure 1. Both showed reversible bipolar resistance switching. The standard device required an initial electroforming step which creates a channel of reduced titanium oxide [26], increasing the conductivity and allowing subsequent bipolar resistance switching to take place. As shown in Figure 1a, the initial high-resistance state ("Virgin") can never be attained and thus the electroforming step is irreversible. In contrast, the bilayer device, Figure 1b, did not require such an electroforming step and subsequent bipolar resistance switching showed that the initial conductive state of the device ("Virgin") is nearly equivalent to the subsequent OFF state. Thus, this bilayer device has three distinct properties: 1) Elimination of the higher power electroforming step, 2) the first ON switching is identical to subsequent ON switching steps, and 3) the initial Virgin state is nearly equivalent to the subsequent OFF state, thus showing that the initial state of the device can be regained, even after going to the high conductance state (ON). These three properties can be used to define a so called "forming-free" device.

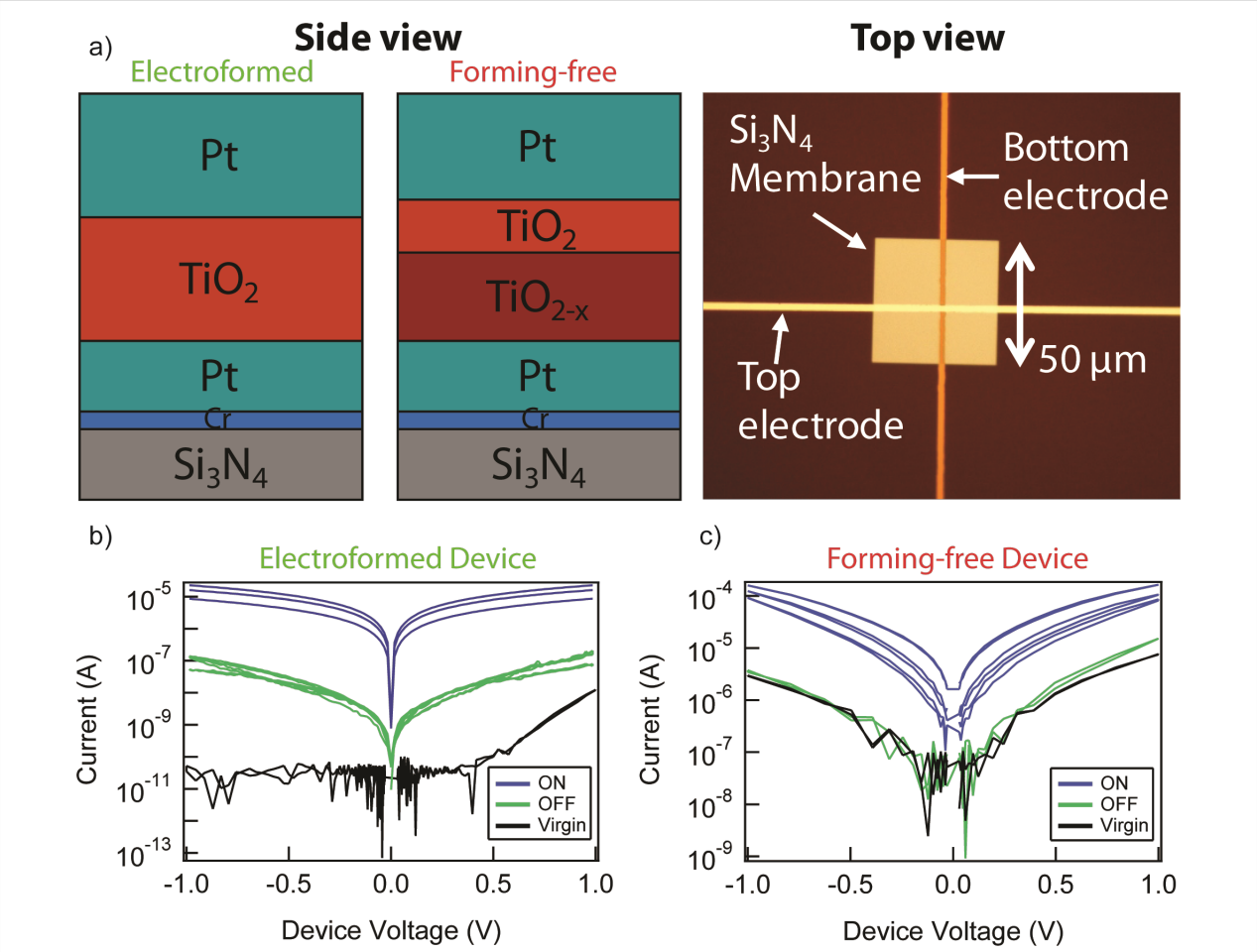

Figure 1: (a) Device schematics from side and top views for the electroformed (left panel) and forming-free (center panel) structures. A top view (right panel) shows the free-standing membrane allowing X-ray transmission measurements. Electrical characterization of (b) normal Pt/TiO_2/Pt and (c) double layer Pt/TiO_{2-x}/TiO_2 device, showing the Virgin, OFF (high resistance), and ON (low resistance) states. The normal device exhibits an irreversible forming step, while the double layer structure is able to regain the Virgin state when turned OFF.

Results and Discussion

Device characterization by X-ray spectromicroscopy

To probe any switching-induced material changes in the devices, characterization was performed using scanning transmission X-ray microscopy (STXM) at the Advanced Light Source in the Lawrence Berkeley National Laboratory. STXM allows spatially-resolved X-ray absorption spectroscopy (XAS) to be performed on a sample and is well-suited for chemical and structural characterization of the thin oxide layer within a memristor device in a non-destructive manner. High-brightness, monochromatic X-rays from a bending magnet are focused using a zone plate lens to approximately 35 nm diameter, with energy resolution of better than 100 meV [31]. In our study, the X-ray energy was swept through the Ti L-edge and for each energy point, the X-ray focus was spatially scanned to acquire an image of the device junction area. Localized spectra were extracted by processing this dataset and integrating pixels within separate regions of the device and thereby deriving the XAS intensity versus energy. This technique has been used for previous studies of the single layer TiO_2 memristor devices and can identify the presence of spatially-localized channels of oxygen vacancy rich Ti–O phases through analysis of the near-edge X-ray absorption fine structure (NEXAFS) [26].

After electrical operation of the memristor devices, STXM measurements were made. Figure 2 compares post-switching X-ray absorption images of a normal electroformed device and a forming-free bilayer device. All images were taken at X-ray energies within the Ti $L_{2,3}$ absorption edge (455–475 eV) which is sensitive to chemical and structural changes [32-34] of the titanium. An additional advantage is that by tuning to a Ti-absorption resonance, contributions from the electrodes (Pt) and other non-Ti elements in the stack are eliminated. In the images of Figure 2, regions with higher absorption are shown with darker contrast, and background absorbing materials such

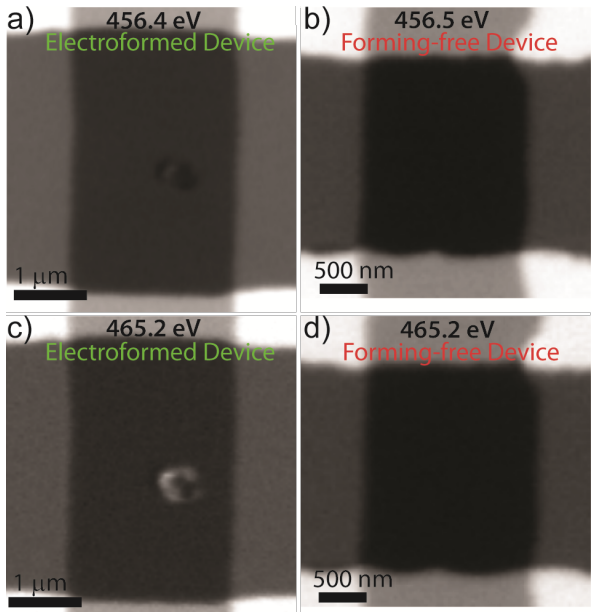

Figure 2: Comparison of scanning transmission X-ray micrographs for electroformed and forming-free devices. Contrast was derived from spatially-resolved X-ray absorption using incident monochromatic X-rays at the indicated energy which is before (456.4/456.5 eV) and within (465.2 eV) the main Ti L_3 edge. For the electroformed device, (a) and (c), a strong contrast was observed within the junction which reversed at the different X-ray energies, and corresponds to the formation of a sub-oxide phase. No such contrast was observed within the junction of the forming-free devices, (b) and (d). More detailed X-ray absorption spectroscopy for these junction regions are shown below in Figure 3.

as the Pt electrodes with a higher elemental mass than the switching layer show up prominently. Nonetheless, in both images of the electroformed device (Figure 2a and Figure 2c), additional contrast was observed within the junction. This contrast is indicative of significant material changes within the device. The forming-free bilayer device, on the other hand, showed no spatial contrast anywhere within or near the device junction. In total, three forming-free devices were studied in STXM after resistance switching and no spatial features indicating material changes were observed.

X-ray absorption spectroscopy was also performed for both types of devices. In this work the NEXAFS of the Ti $L_{2,3}$ edges of the film were integrated within the junction area. Figure 3 shows the spectra for electroformed (a) and forming-free (b) devices, in both cases comparing the Virgin material state to that after electrical switching. Within an electroformed device (Figure 3a) dramatic material changes were observed even when only comparing the switched and Virgin state qualitatively. The spectrum of the Virgin state showed four main peaks which are the L_3 and L_2 absorption peaks, each crystal field split into doublets (457–462 eV and 462–468 eV). The Virgin state spectrum is consistent with an amorphous state of the TiO_2 [26,35]. In contrast, within the switched device, a NEXAFS spectrum was observed with a reduced crystal field splitting as well as a prominent lower energy absorption at 456 eV, assigned to the Ti^{3+} valence state. The NEXAFS therefore indicates a mixed-valence composition including both Ti^{3+} and Ti^{4+}, and matches well the spectrum observed in reduced titanium oxide layers [36-38]. It is additionally worth noting that the spectrum observed in the ON and OFF state of the device was similar [26], suggesting that the material changes occurred during electroforming rather than during switching and that any material differences between the ON and OFF states were undetectable with this technique.

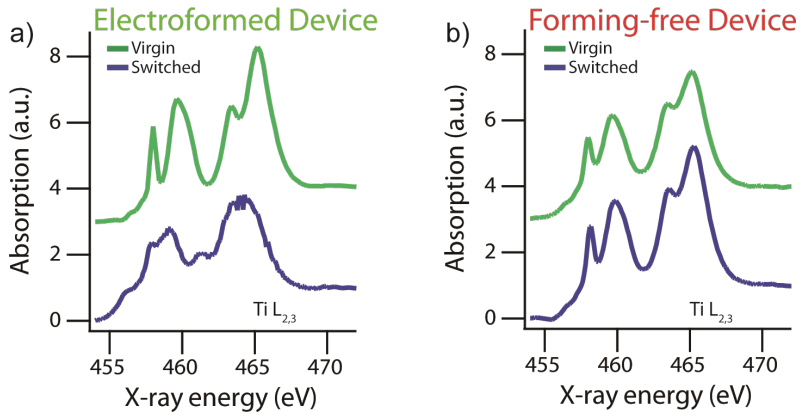

Figure 3: X-ray absorption spectroscopy within the junction region of an electroformed and forming-free device. The Ti L_3 absorption edge is shown, which is sensitive to chemical composition and structure state. (a) The "Virgin" NEXAFS spectrum (green curve) was derived from a neighboring, simultaneously grown device which was not electrically biased, while the "switched" spectrum (blue curve) came from within the materially altered nanoscale region in the electroformed device of Figure 2 with a size of roughly 200 nm × 200 nm. (b) Both "Virgin" and "switched" spectra (green and blue curves, respectively) were derived from the junction region in the forming-free device of Figure 2, before and after the application of electrical bias, respectively.

For the forming-free device containing a TiO_{2-x} layer, the non-stoichiometry is qualitatively evident in the NEXAFS of the material grown, seen in the Virgin state (Figure 3b, green curve). Compared to the as-grown stoichiometric TiO_2 layer (Figure 3a, green curve), this spectrum exhibits more merged and less prominent crystal field split doublets (457–462 eV and 462–468 eV). While not as distinct as the heavily reduced phase found in the electroformed layer (Figure 3a, blue curve), the trend is the same, showing that indeed the as-grown film for forming-free devices contains a substantial concentration of reduced valence titanium atoms and therefore oxygen vacancies.

Between the Virgin and switched states of the forming-free device, presented in Figure 3b, no large qualitative differences in the NEXAFS spectrum are observed. However, a very slight sharpening and increased absorption is seen in the spectrum after switching, which is likely caused by Joule heating from the applied current, which serves to anneal the film during operation [29,35] and to reduce disorder. The overall lack of material changes in the forming-free compared to the electroformed devices shows a progress in reducing the device damage during operation and can thus improve the technological promise of memristors. However, the presence of conductive channels less than 50 nm in areal diameter is not ruled out in this X-ray study, as spectroscopy of such small channels is at the limit of the present technique, and would require higher resolution electron-based measurements.

Device characterization by TEM

TEM characterization was performed using a JEM 2100F microscope. A customized single-tilt sample-holder tip was designed to accommodate the silicon/silicon-nitride substrates with the memristor device. The electron microscope was used to obtain selected area electron diffraction (SAED) patterns as well as for transmission and scanning-transmission imaging from bright-field and high-angle annular dark-field (HAADF) detection. Figure 4a shows a low-magnification TEM image of the post-switched forming-free device. A careful analysis of the junction region in the ON state indicates no clear evidence of local modifications as a result of the switching process. This fact was also suggested from a comparison among different images obtained from devices in ON, OFF and 'Virgin' states. Additionally, Figure 4b shows SAED patterns obtained through the regions indicated as #1 and #2 in Figure 4a. The diffraction patterns are dominated by the metallic elements and indicate polycrystalline material. The SAED pattern from region #1 (Pt/TiO_{2-x}/TiO_2/Pt) is dominated by the Pt electrodes. Region #2 (TiO_{2-x}/TiO_2 on silicon nitride) evidences only diffuse rings indicating predominantly amorphous material. Using different selecting apertures, other areas within the junction region were analyzed with equivalent results. Hence, these results indicate that the titanium oxide phases are amorphous, with no observation of structural or physical modifications in the junction originating from the switching process.

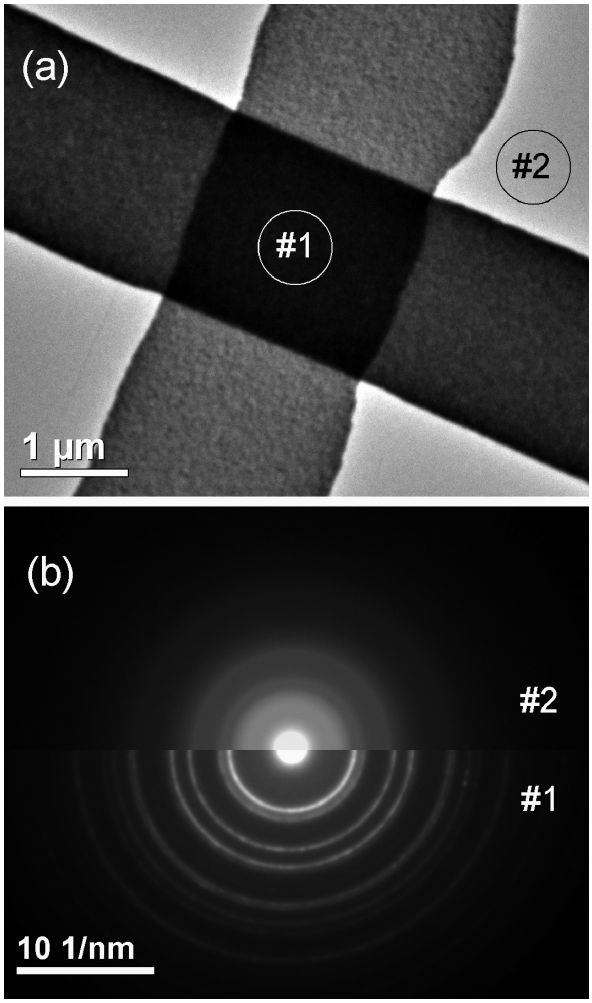

Figure 4: (a) Low-magnification TEM image of the junction region from a forming-free device in the ON state. (b) SAED patterns obtained in the two regions indicated in (a).

Scanning transmission electron microscopy (STEM) was also used to explore the forming-free device from a structural and morphological standpoint. Figure 5 depicts STEM images obtained from bright-field (BF) detection. BF imaging was utilized rather than HAADF detection due to the latter having an image contrast mainly dominated by the local atomic mass. In addition, the BF imaging has a major electron-phase contribution and channeling effect, which are more appropriate for probing the switching process. Nonetheless, no evidence of a switching effect was observed from a careful analysis along the junction. However, BF image analysis indicated that the Pt grains from the top electrode are larger than those of the bottom

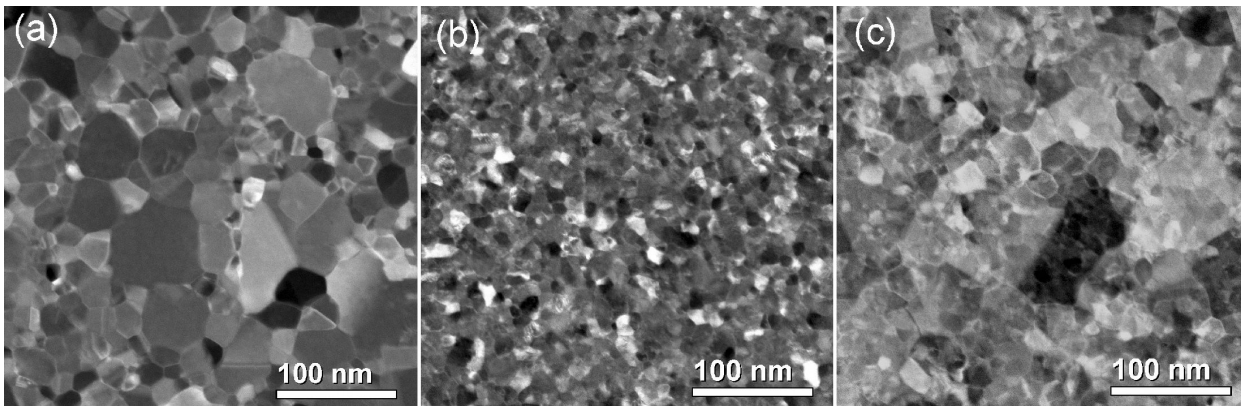

Figure 5: Bright-field STEM images obtained within different regions of the forming-free device: (a) top electrode, (b) bottom electrode, and (c) junction.

electrode, as seen in Figure 5a and Figure 5b. These grain size distributions were observed to be uniform within the junction, roughly 20 μm away at the Si_3N_4 window edge, and over the Si substrate outside of the window (as checked by scanning electron microscopy). This strongly suggests that the grain growth was initiated by self-heating in the thin film electrode itself.

Conclusion

We have seen that it is possible to reduce and nearly eliminate many of the damaging effects which had been observed in titanium oxide based resistance switching devices [24-27] by engineering devices with an oxygen deficient layer which can serve as a vacancy reservoir. It was shown that, electrically, such a structure removed the need for a high voltage electroforming step and the as-fabricated device resistance closely matched the later attained OFF state. In addition, using several physical characterization methods with chemical and structural sensitivity and nanoscale spatial resolution, we saw that the cycling of the device did not bring about observable material changes. Thus, any such changes must be more subtle. One limitation of both techniques employed here is the lack of sensitivity in the direction perpendicular to the sample plane as these methods integrate through the entire layer stack in a transmission geometry. Thus, it is worthy of future study to explore the materials modifications in the perpendicular direction. Additionally, while the work presented here has shown the material state before and after electrical switching and the forming is performed ex-situ, in-situ studies, particularly with TEM, may be the best method to further probe and discover any minute material changes in a manner that can be directly correlated with the resistance switching in real time.

Acknowledgements

Work at HP was partially supported by the U.S. Government's Nano-Enabled Technology Initiative. Work at the Advanced Light Source at Lawrence Berkeley National Laboratory is supported by the Director, Office of Science, Office of Basic Energy Sciences, of the U.S. Department of Energy under Contract No. DE-AC02-05CH11231. We acknowledge the Brazilian Nanotechnology National Laboratory and Brazilian Center for Research in Energy and Materials for use of the electron microscopy facilities.

References

1. Chua, L. O. *IEEE Trans. Circuit Theory* **1971,** *18,* 507. doi:10.1109/TCT.1971.1083337
2. Chua, L. O.; Kang, S. M. *Proc. IEEE* **1976,** *64,* 209. doi:10.1109/PROC.1976.10092
3. Strukov, D. B.; Snider, G. S.; Stewart, D. R.; Williams, R. S. *Nature* **2008,** *453,* 80. doi:10.1038/nature06932
4. Chua, L. O. *Appl. Phys. A* **2011,** *102,* 765. doi:10.1007/s00339-011-6264-9
5. Dearnaley, G.; Stoneham, A. M.; Morgan, D. V. *Rep. Prog. Phys.* **1970,** *33,* 1129. doi:10.1088/0034-4885/33/3/306
6. Waser, R.; Dittman, R.; Staikov, G.; Szot, K. *Adv. Mater.* **2009,** *21,* 2632. doi:10.1002/adma.200900375
7. Liu, S. Q.; Wu, N. J.; Ignatiev, A. *Appl. Phys. Lett.* **2000,** *75,* 2749. doi:10.1063/1.126464
8. Sawa, A.; Fuji, T.; Kawasaki, M.; Tokura, Y. *Appl. Phys. Lett.* **2004,** *85,* 4073. doi:10.1063/1.1812580
9. Szot, K.; Speier, W.; Bihlmayer, G.; Waser, R. *Nat. Mater.* **2006,** *5,* 312. doi:10.1038/nmat1614
10. Jeong, D. S.; Schroeder, H.; Waser, R. *Electrochem. Solid-State Lett.* **2007,** *10,* G51. doi:10.1149/1.2742989
11. Meijer, G. I. *Science* **2008,** *319,* 1625. doi:10.1126/science.1153909
12. Odagawa, A.; Sato, H.; Inoue, I. H.; Akoh, H.; Kawasaki, M.; Tokura, Y.; Kanno, T.; Adachi, H. *Phys. Rev. B* **2004,** *70,* 224403. doi:10.1103/PhysRevB.70.224403
13. Rozenberg, M. J.; Inoue, I. H.; Sánchez, M. J. *Appl. Phys. Lett.* **2006,** *88,* 033510. doi:10.1063/1.2164917
14. Shoute, L. C. T.; Pekas, N.; Wu, Y.; McCreery, R. L. *Appl. Phys. A* **2011,** *102,* 841. doi:10.1007/s00339-011-6268-5
15. Lee, J. S.; Ortolani, M.; Schade, U.; Chang, Y. J.; Noh, T. W. *Appl. Phys. Lett.* **2007,** *90,* 051907. doi:10.1063/1.2437086

16. Janotti, A.; Varley, J. B.; Rinke, P.; Umezawa, N.; Kresse, G.; Van de Walle, C. G. *Phys. Rev. B* **2010,** *81,* 085212. doi:10.1103/PhysRevB.81.085212
17. Jiang, W.; Noman, M.; Lu, Y. M.; Bain, J. A.; Salvador, P. A.; Skowronski, M. *J. Appl. Phys.* **2011,** *110,* 034509. doi:10.1063/1.3622623
18. Janousch, M.; Meijer, G. I.; Staub, U.; Delley, B.; Karg, S. F.; Andreasson, B. P. *Adv. Mater.* **2007,** *19,* 2232. doi:10.1002/adma.200602915
19. Andreasson, B. P.; Janousch, M.; Staub, U.; Todorova, T.; Delley, B.; Meijer, G. I.; Pomjakushina, E. *Phys. Rev. B* **2009,** *80,* 212103. doi:10.1103/PhysRevB.80.212103
20. Jeong, H. Y.; Lee, J. Y.; Choi, S.-Y.; Kim, J. W. *Appl. Phys. Lett.* **2009,** *95,* 162108. doi:10.1063/1.3251784
21. Martinez, E.; Guedj, C.; Calka, P.; Minoret, S.; Buckley, J.; Bernard, Y.; Jousseaume, V. *Surf. Interface Anal.* **2010,** *42,* 783. doi:10.1002/sia.3343
22. Calka, P.; Martinez, E.; Lafond, D.; Dansas, H.; Tirano, S.; Jousseaume, V.; Bertin, F.; Guedj, C. *Microelectron. Eng.* **2011,** *88,* 1140. doi:10.1016/j.mee.2011.03.125
23. Fujii, T.; Arita, M.; Hamada, K.; Kondo, H.; Kaji, H.; Takahashi, Y.; Moniwa, M.; Fujiwara, I.; Yamaguchi, T.; Aoki, M.; Maeno, Y.; Kobayashi, T.; Yoshimaru, M. *J. Appl. Phys.* **2011,** *109,* 053702. doi:10.1063/1.3553868
24. Schroeder, H.; Pandian, R.; Miao, J. *Phys. Status Solidi A* **2011,** *208,* 300. doi:10.1002/pssa.201026743
25. Kwon, D.-H.; Kim, K. M.; Jang, J. H.; Jeon, J. M.; Lee, M. H.; Kim, G. H.; Li, X.-S.; Park, G.-S.; Lee, B.; Han, S.; Kim, M.; Hwang, C. S. *Nat. Nanotechnol.* **2010,** *5,* 148. doi:10.1038/nnano.2009.456
26. Strachan, J. P.; Pickett, M. D.; Yang, J. J.; Aloni, S.; Kilcoyne, A. L. D.; Medeiros-Ribeiro, G.; Williams, R. S. *Adv. Mater.* **2010,** *22,* 3573. doi:10.1002/adma.201000186
27. Yang, J. J.; Miao, F.; Pickett, M. D.; Ohlberg, D. A. A.; Stewart, D. R.; Lau, C. N.; Williams, R. S. *Nanotechnology* **2009,** *20,* 215201. doi:10.1088/0957-4484/20/21/215201
28. Nauenheim, C.; Kuegeler, C.; Ruediger, A.; Waser, R. *Appl. Phys. Lett.* **2010,** *96,* 122902. doi:10.1063/1.3367752
29. Borghetti, J.; Strukov, D. B.; Pickett, M. D.; Yang, J. J.; Stewart, D. R.; Williams, R. S. *J. Appl. Phys.* **2009,** *106,* 124504. doi:10.1063/1.3264621
30. Pickett, M. D.; Strukov, D. B.; Borghetti, J. L.; Yang, J. J.; Snider, G. S.; Stewart, D. R.; Williams, R. S. *J. Appl. Phys.* **2009,** *106,* 074508. doi:10.1063/1.3236506
31. Kilcoyne, A. L. D.; Tyliszczak, T.; Steele, W. F.; Fakra, S.; Hitchcock, P.; Franck, K.; Anderson, E.; Harteneck, B.; Rightor, E. G.; Mitchell, G. E.; Hitchcock, A. P.; Yang, L.; Warwick, T.; Ade, H. *J. Synchrotron Radiat.* **2003,** *10,* 125. doi:10.1107/S0909049502017739
32. van der Laan, G. *Phys. Rev. B* **1990,** *41,* 12366. doi:10.1103/PhysRevB.41.12366
33. de Groot, F. M. F.; Figueiredo, M. O.; Basto, M. J.; Abbate, M.; Petersen, H.; Fuggle, J. C. *Phys. Chem. Miner.* **1992,** *19,* 140. doi:10.1007/BF00202101
34. de Groot, F. M. F.; Fuggle, J. C.; Thole, B. T.; Sawatzky, G. A. *Phys. Rev. B* **1990,** *42,* 5459. doi:10.1103/PhysRevB.42.5459
35. Strachan, J. P.; Yang, J. J.; Münstermann, R.; Scholl, A.; Medeiros-Ribeiro, G.; Stewart, D. R.; Williams, R. S. *Nanotechnology* **2009,** *20,* 485701. doi:10.1088/0957-4484/20/48/485701
36. Soriano, L.; Abbate, M.; Vogel, J.; Fuggle, J. C.; Fernández, A.; González-Elipe, A. R.; Sacchi, M.; Sanz, J. M. *Surf. Sci.* **1993,** *290,* 427. doi:10.1016/0039-6028(93)90725-Y
37. Lusvardi, V. S.; Barteau, M. A.; Chen, J. G.; Eng, J., Jr.; Frühberger, B.; Teplyakov, A. *Surf. Sci.* **1998,** *397,* 237. doi:10.1016/S0039-6028(97)00740-1
38. Pollakowski, B.; Beckhoff, B.; Reinhardt, F.; Braun, S.; Gawlitza, P. *Phys. Rev. B* **2008,** *77,* 235408. doi:10.1103/PhysRevB.77.235408

License and Terms